SYNTHESIS, CHARACTERIZATION AND POTENTIAL APPLICATIONS OF FePt NANOPARTICLES

by

VIKAS NANDWANA

Presented to the Faculty of the Graduate School of

The University of Texas at Arlington in Partial Fulfillment

of the Requirements

for the Degree of

DOCTOR OF PHILOSOPHY

THE UNIVERSITY OF TEXAS AT ARLINGTON

May 2009

Dedicated to

My Parents and Wife

ACKNOWLEDGEMENTS

I would like to express my deepest appreciation and gratitude to my advisor, Professor J. Ping Liu, for providing invaluable guidance for my research and for constantly supporting me over the past five years. I especially thank him for introducing me to scientific research and providing me with challenges. His expertise in nanostructured magnetism, along with his vision of nanotechnology, has been a source of inspiration for me to pursue further research in this exciting field. The present research could not have been completed without his expert guidance, constant supervision, and onging encouragement. I would also like to express my appreciation to Professors Stathis I. Meletis, Choong-Un Kim, Ali R. Koymen, and Yaowu Hao, for serving on my dissertation supervisory committee. I am grateful to them for their support of my research and for their careful and critical reading of my dissertation. I am indebted to past and present colleagues for their important suggestions, assistance, encouragement of my studies and research, and wonderful friendship during our time together. Among them are Dr. Chuan-bing Rong, Dr. Girija S. Chaubey, Dr. Narayan Poudyal, Dr. Kevin Elkins, Dr. Zhiqiang Jin, Vamsi Chakka, Tejaswi Vedantam, Kung-Te Chu, Kazuaki Yano, Dr. Yiping Wang, Dr. Yang Li, Dr. Baki Altuncevahir, Yunpeng Zhang, Daren Li, Dr. Ming Yue, Dr. Shirly Machluf, Dr. Kendra Wallis, Dr. Nguyen Van Vuong, Hamed Arami, John Griffis and Chengyang Liu. I am thankful to our collaborator, Dr. Z. L. Wang at The Georgia Institute of Technology for providing assistance with the HRTEM analysis. I am also grateful to Dr. Shishou S. Kang for his help with the HRTEM analysis at The University of Alabama. I am thankful to Dr. Jiechao Jiang and Mike Coviello in the Department of Materials Science and Engineering at UTA for the technical support he provided with for operating the TEM and SEM.

I would like to thank all the faculty and staff members in the Department of Materials Science and Engineering at UTA. My studies and research experiences have been so memorable because of their diligent effort to create a great environment for all students. I am grateful to The University of Texas at Arlington for providing me such a wonderful environment for my studies. I also express my indebtedness to all my friends for their encouragement to complete this work, particularly Neerav, Mitech, Sachin, Karan, Puneet, and Sarath. There can be no adequate acknowledgement for the loving encouragement I have received from my parents, brothers, sisters and all family members. Without their constant support and inspiration all this would never have been possible. My final thanks go to my wife Deepika, who has continuously supported me throughout the process of my pursuing this PhD. The daily encouragement she provided makes this dissertation as much hers as it is mine. This work was supported by US DoD/MURI grant N00014-05-1-0497 and DARPA through ARO under Grant No DAAD 19-03-1-0038. This work was also supported by The Center of Nanostructured Materials and Characterization Center for Materials and Biology at The University of Texas at Arlington.

April 20, 2009

ABSTRACT

SYNTHESIS, CHARACTERIZATION AND POTENTIAL APPLICATIONS OF FePt NANOPARTICLES

Vikas Nandwana, PhD

The University of Texas at Arlington, 2009

Supervising Professor: J. Ping Liu

Monodisperse FePt nanoparticles with controlled size and geometry have drawn great attention in the last decade for fundamental scientific studies and for their potential applications in advanced materials and devices such as ultra-high-density magnetic recording media, exchange-coupled nanocomposite magnets, biomedicines and nanodevices. This dissertation focuses on the synthesis and characterization of FePt nanoparticles and their use in potential applications.

The FePt nanoparticles of different size (2 to 16 nm) and shape (spherical, cubic, rod) were synthesized by a chemical solution method. The size and shape of these particles were controlled by adjusting reaction parameters. The as-synthesized FePt nanoparticles have chemically disordered fcc structure and are superparamagnetic at room temperature. Upon heat treatment the nanoparticles were transformed into ordered $L1_0$ structure, and high coercivity up to 27 kOe was achieved. Magnetic properties of annealed FePt nanoparticles including magnetization and coercivity were strongly dependent on particle size, shape, composition and annealing temperature.

$FePt/Fe_3O_4$ bimagnetic nanoparticles with two different morphologies, core/shell and heterodimer, were prepared by coating or attaching Fe_3O_4 on surface of FePt nanoparticles. The size of FePt and Fe_3O_4 was tuned very finely to obtain most effective exchange coupling. The heterodimer nanoparticles resulted in relatively poor magnetic properties compared to the core/shell nanoparticles due to insufficient exchange coupling. By optimizing the dimensions of the FePt and Fe_3O_4 in core/shell bimagnetic nanoparticles, energy products up to 17.8 MGOe were achieved.

$FePt/Fe_3O_4$ core/shell and $FePt+Fe_3O_4$ mixed nanoparticles with similar magnetic properties were compacted under 2.0 GPa at 400 °C, 500 °C and 600 °C. A density up to 84% of the full density was achieved. After annealing at 650 °C in forming gas, the $FePt/Fe_3O_4$ compacted samples were converted into $L1_0$ $FePt/Fe_3Pt$ magnetic nanocomposite. The nanoscale morphology was retained before and after annealing for bulk samples made from both core/shell and mixed nanoparticles. After annealing, the highest energy product in the bulk samples was 18.1 MGOe based on the theoretical density. The core/shell nanoparticle compacted samples had more effective exchange coupling than the mixed nanoparticle compacted samples.

FePt/Au core/shell nanoparticles were successfully synthesized where Au shell was coated by reduction of gold acetate on surface of FePt nanoparticles. The FePt/Au core/shell nanoparticles show ferromagnetism after annealing at optimum temperature without any significant sintering. Also, FePtAu nanoparticles were prepared by doping Au into FePt nanoparticles during the synthesis. By tuning right stoichiometry of the $Fe_xPt_yAu_{100-x-y}$ nanoparticles, the phase transition temperature from fcc to $L1_0$ was reduced by more than 200 °C. After annealing at 500 °C, the highest coercivity of 18 kOe was obtained from the $Fe_{51}Pt_{36}Au_{13}$ nanoparticles compared to 2 kOe from $Fe_{51}Pt_{49}$ nanoparticles without any sacrifice in saturation magnetization.

TABLE OF CONTENTS

LIST OF ILLUSTRATIONS

LIST OF TABLES

CHAPTER 1

MAGNETISM AND MAGNETIC MATERIALS

1.1 Basics of Magnetism

1.1.1 *Origin of Magnetism*

Magnetism describes phenomenon of forces between two or more objects that are related to a magnetic field. This magnetic field is created by the movements and interactions of electrons. A magnet is an object that exhibits an external magnetic field and can be categorized into electromagnets or permanent magnets. An electromagnet is a type of magnet in which the magnetic field is produced by a flow of an electric current in a wire. In contrast, a permanent magnet is a type of magnet in which the magnetic moments of the orbital electrons are aligned.[1-2] Therefore each atom can be considered as a tiny magnet. The electromagnetic field disappears when the current is removed, while a permanent magnet retains its magnetism for a long time. For the permanent magnets, orbital electrons create a magnetic moment by moving around a nucleus (Figure 1.1). There is also a spin magnetic moment which is caused by a spin of electron itself. However, in most elements except a few (iron, cobalt, and nickel), there is no net magnetic moment because in pairs of electrons the magnetic moments are cancelled by their neighbors.

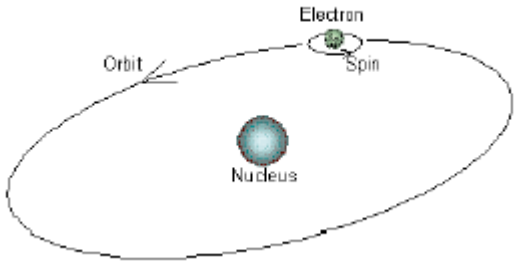

Figure 1.1 Orbit of a spinning electron about the nucleus of an atom.

1.1.2 *Magnetic Field and Magnetic Moment*

The magnetic field strength is expressed by *H*. Here the magnetic flux density *B*, which is defined in terms of force on moving charge in the Lorentz force law, is shown as follow,

$$B = H + 4 \pi M \quad (1.1)$$

where, *M* is called magnetization which is explained as the total magnetic moment *m* in unit volume. The magnetic properties of materials can be characterized not only by the magnitude of *M*, but also the magnitude of *M* change by varying *H*.[2] The ratio between *M* and *H* is called susceptibility (*k*),

$$k = M / H \quad (1.2)$$

Also the permeability (μ) is a similar quantity as the susceptibility and defined as,

$$\mu = B / H \quad (1.3)$$

The type of magnetism can be characterized by observing the susceptibility and permeability of a material.

1.2 Classification of Magnetism

The origin of magnetism lies in the orbital and spin motions of electrons. Electron interactions also have strong effect in magnetism. In some materials, there is no collective interaction of atomic magnetic moments, whereas in other materials there are very strong interactions among atomic moments. The way to classify the different types of magnetism depends on how materials respond to magnetic fields. The magnetic behavior of materials can be classified into diamagnetism, paramagnetism, ferromagnetism, antiferromagnetism and ferrimagnetism (Figure 1.2).[3]

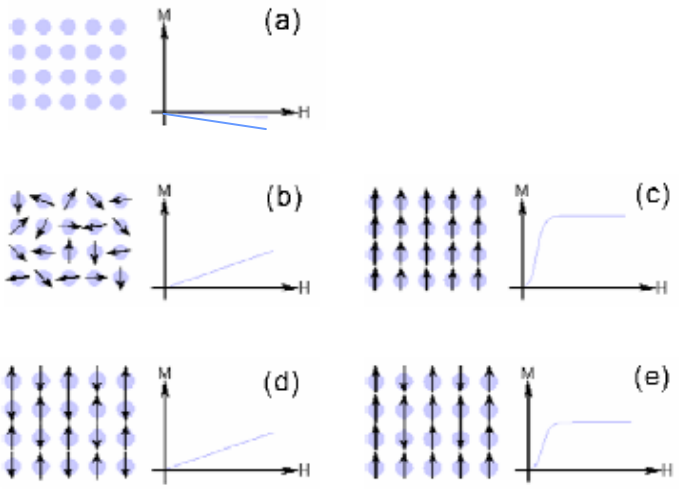

Figure 1.2 Summary of different types of magnetic behavior. (a) diamagnetism, (b) paramagnetism, (c) ferromagnetism, (d) antiferromagnetism and (e) ferrimagnetism.

1.2.1 Diamagnetism

Diamagnetism is a fundamental property of all matter, although it is usually very weak. It is due to the non-cooperative behavior of orbiting electrons when exposed to an applied magnetic field. Diamagnetic substances are composed of atoms which have no net magnetic moments (i.e., all the orbitals are filled and there are no unpaired electrons). However, when exposed to a field *H*, the orbiting electrons either accelerate or decelerate so that their magnetic moments are in the opposite direction from the external field and a negative magnetization is produced. The susceptibility *k* is < 0 (order of 10^{-5}) for a diamagnetic material, resulting in very low negative moments.[1-6]

1.2.2 Paramagnetism

For this class of materials, some of the atoms or ions in the material have a net magnetic moment due to unpaired electrons in partially filled orbitals. However, the individual magnetic moments do not interact magnetically, and as with diamagnetism, the net magnetization is zero when the field is not applied. In the presence of a field, there is a partial alignment of the atomic magnetic moments in the direction of the field, resulting in a net positive magnetization such that the susceptibility *k* is > 0 (order of 10^{-5} to 10^{-2}) for paramagnetic materials.[1-3] In addition, the

efficiency of an external field in aligning the moments is opposed by randomizing effects of temperature. This results in a temperature dependent susceptibility known as the Curie Law.

1.2.3 Ferromagnetism

Ferromagnetic materials exhibit parallel alignment of permanent magnetic moments, resulting in a large net magnetization even in the absence of a magnetic field. These moments originate from the overall contribution of electron spin and orbital magnetic moments.[4] The elements Fe, Ni, and Co and many of their alloys are typical ferromagnetic materials. Magnetic susceptibility as high as 10^6 is possible for ferromagnetic materials. Two distinct characteristics of ferromagnetic materials are their spontaneous magnetization and the existence of magnetic ordering temperature. The spontaneous magnetization is the net magnetization that exists inside a uniformly magnetized microscopic volume in the absence of an external field. As temperature increases, the arrangement of atomic moments is disturbed by the thermal agitation, resulting in temperature dependence of spontaneous magnetization. In spite of the presence of spontaneous magnetization, a large piece of ferromagnetic or ferromagnetic substance is usually not spontaneously magnetized but exists rather in a demagnetized state. This is because the interior of the piece is divided into many magnetic domains, each of which is spontaneously magnetized. Since the direction of domain magnetization varies from domain to domain, the resultant magnetization can be changed from zero to the value of spontaneous magnetization.[1] The saturation magnetization (M_s) is the maximum induced magnetic moment that can be obtained in a magnetic field beyond which no further increase in magnetization occurs. Saturation magnetization is an intrinsic property and dependent on temperature.

1.2.4 *Antiferromagnetism*

In some other types of materials, the magnetic moment coupling between adjacent atoms or ions results in the antiparallel alignment of the magnetic dipoles. This phenomenon of the alignment of spin moments of neighboring atoms or ions in exactly opposite directions is termed as antiferromagnetism. The opposing magnetic moments cancel one another, resulting in zero

net magnetization of the material.[2,4] Some examples of antiferromagnetic crystals are manganese oxide (MnO), manganese sulfide (MnS), and iron oxide (FeO).

1.2.5 *Ferrimagnetism*

Ferrimagnetism is another type of magnetic ordering. In ferrimagnets, the moments of adjacent atoms or ions are in an antiparallel alignment, but they do not cancel out each other. The best example of a ferromagnetic mineral is magnetite (Fe_3O_4). The structural formula for magnetite is $[Fe^{3+}]A\ [Fe^{3+},Fe^{2+}]BO_4$. This particular arrangement of cations on the A and B sublattices is called an inverse spinel structure. With negative AB exchange interactions, the net magnetic moment of magnetite is due to the B-site Fe^{2+} because the moments from the trivalent ions are opposite and cancel each other. Ferrimagnetism is therefore similar to ferromagnetism. Ferrimagnetism exhibits all the hallmarks of ferromagnetic behavior: spontaneous magnetization, Curie temperatures, hysteresis, and remanence. However, ferro and ferrimagnets have very different magnetic ordering.

1.3 Characteristic of Ferromagnetic Materials[1-5,7]

1.3.1 *Curie Temperature*

Even though electronic exchange forces in ferromagnets are very large, thermal energy eventually overcomes the exchange interaction and produces a randomizing effect. This effect becomes dominant at a particular temperature called the Curie temperature (*T*c). Below the Curie temperature, the magnetic structure is ordered, and above the Curie temperature the magnetic structure is disordered. The saturation magnetization goes to zero at the Curie temperature. The Curie temperature is an intrinsic property of materials and is a diagnostic parameter that can be used for mineral identification. However, it is not full proof because different magnetic minerals, in principle, can have the same Curie temperature.

1.3.2 Magnetic Domains

Any ferromagnetic material at a temperature below Curie temperature (*Tc)* is composed of small-volume regions known as domains, in which there is the mutual alignment of the magnetic moments in the same direction, as illustrated in Figure 1.3(a). Each domain is

magnetized to its saturation magnetization, and adjacent domains are separated by domain walls, across which the direction of magnetization gradually changes (see Figure 1.3(b)).

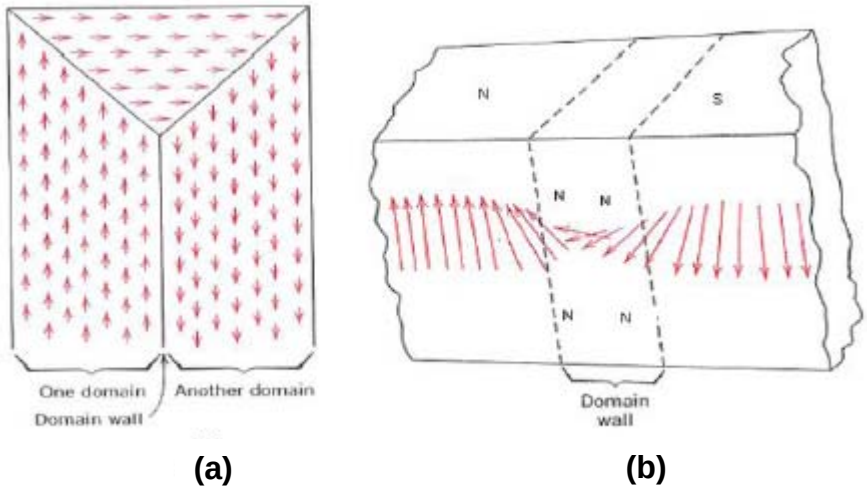

Figure 1.3 (a) Creation of domain and domain wall and (b) spin orientation rotation through domain (Bloch) wall.

Domain walls have a finite width that is determined principally by exchange and magnetocrystalline anisotropy energy. Exchange energy tends to keep magnetic moment parallel to each other and can be kept small if the 180 ° rotation takes place gradually with wide wall as shown in Figure 1.4 (a), but large with thin wall as shown in Figure 1.4 (b).[7] However, for the wide wall structure, the magnetizations within the wall are no longer aligned along an easy axis of magnetization. This produces an anisotropy energy, which is high in (a) but low in (b). The exchange energy tends to make the wall as wide as possible whereas the anisotropy tends to make the wall as thin as possible. As a result of this competition between exchange and anisotropy energies, the domain wall has a finite width (on the order of few nanomters).

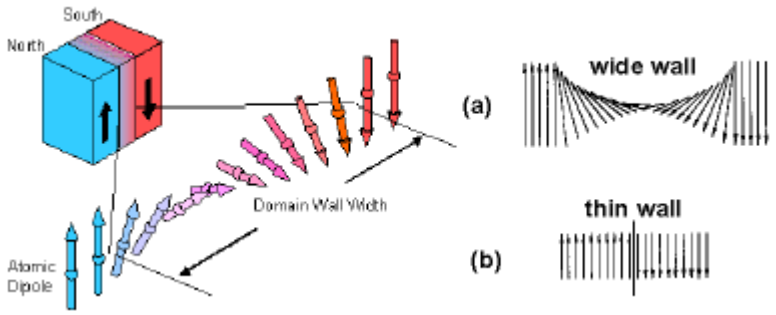

Figure 1.4 Schematic representation of a 180 º domain wall with (a) wide wall with gradual magnetization change, and (b) thin wall with abrupt magnetization change.[8]

1.3.3. *Hysteresis Loops*

Ferromagnets can retain the memory of an applied field even after the field is removed. This behavior is called hysteresis, and a plot of the variation of magnetization with magnetic field is called a hysteresis loop. The hysteresis loop is a means of characterizing magnetic materials, and various parameters can be determined from it. Initially, the moments of the constituent domains are randomly oriented in such a way that there is no net *B (or M)* field. As shown in Figure 1.5, on the application of a field to an unmagnetized sample, the polarization increases initially by the growth of favorably oriented domains, which will be magnetized in the easy direction of the crystal. When the polarization can increase no further by the growth of domains, the direction of magnetization of the domains then rotates away from the easy axis to align with the field. When all of the domains have fully aligned with the applied field, saturation is reached, and the polarization can increase no further. The maximum value of *M* is called the saturation magnetization M_s, and the resultant *M-H* curve is called the initial magnetization curve. Starting from the saturation point (see Figure 1.5), when the *H* field is reduced, the curve does not retrace its original path. A hysteresis effect is produced in which the *M* field lags behind the applied *H* field or decreases at a lower rate. At zero field, a residual *M* is called the remanence or remanent magnetization M_r is retained, indicating that the material remains magnetized even in the absence of an external *H* field. The polarization will only decrease after a sufficiently high field is applied to: (1) nucleate and grow domains favorably oriented with respect to the applied field or (2) rotate

the direction of magnetization of the domains towards the applied field. After applying a high enough reversal field, saturation polarization will be achieved in the negative direction. If the applied field is then decreased and again applied in the positive direction then the full hysteresis loop is plotted (Figure 1.5). The area contained within the loop indicates the amount of energy absorbed by the material during each cycle of the hysteresis loop. The reverse field required to bring the magnetic induction B of a specimen to zero is called the inductive coercivity (H_b) whereas the reverse field required to bring the magnetization M to zero is called the intrinsic coercivity (H_c). The remanence ratio M_r/M_s is generally used as measure of squareness of the *M-H* loop.

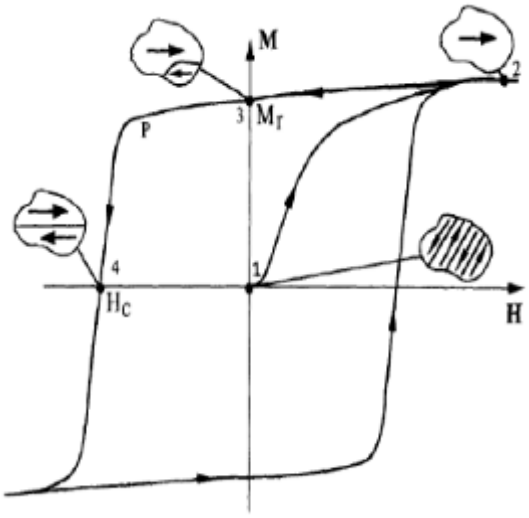

Figure 1.5 The magnetization curve and hysteresis loop of a permanent magnet showing the magnetic domain structure in the virgin state (1), at saturation (2), at remanence (3), and at the coercive field (4).[9]

1.3.4 Magnetic Anisotropy

In many situations, the susceptibility of a ferromagnetic material will depend on the direction in which it is measured. Such a situation is called magnetic anisotropy. When magnetic anisotropy exists, the total magnetization of a ferromagnetic *Ms* will prefer to lie along a special direction called the easy axis or crystal axis. In case of hexagonal close packed (HCP) or tetragonal crystal, the easy axis is usually the c-axis. Under an applied field, the magnetic

moment deviates from the easy direction and returns to its original alignment with the removal of the field. The energy associated with this alignment is called the anisotropy energy and in its lowest order form is given by:[2]

$$E_a = K \sin^2\theta \qquad (1.4)$$

where θ is the angle between M_s and the easy axis, and K is the anisotropy constant (units is ergs/cm^3). There are several causes of anisotropy, including those induced by stress and prior mechanical handling of materials. Two important and common sources of anisotropy, which are magnetocrystalline anisotropy and shape anisotropy, are discussed next.

1.3.4.1 Magnetocrystalline Anisotropy

Only magnetocrystalline anisotropy, or simply crystal anisotropy, is intrinsic to the materials; all other anisotropies are induced. In crystal anisotropy, the ease of obtaining saturation magnetization is different for different crystallographic directions. The direction of easy magnetization of crystal is the direction of spontaneous domain magnetization in the demagnetized state. An example is a single crystal of cobalt as shown Figure 1.6.

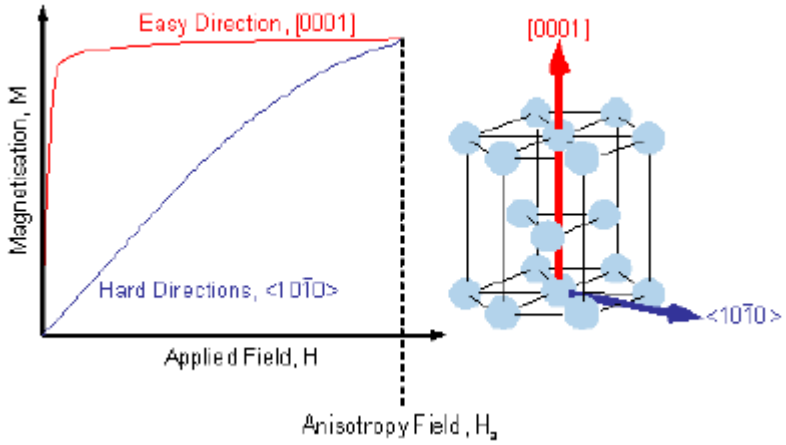

Figure 1.6 Directional dependence of saturation magnetization in Cobalt metal.[10]

1.3.4.2 Shape Anisotropy

It is easier to induce a magnetization along the long direction of a nonspherical piece of material than along a short direction. This is so because the demagnetizing field is less in the

long direction, for the reason that the induced poles at the surface are farther apart. Thus, a smaller applied field will negate the internal, demagnetizing field. The shape anisotropy can be very important for nonspherical materials. The long axis of a specimen plays the same role as the easy axis of the crystal, and the shape anisotropy constant K_s is given by:

$$K_s = ½(N_a - N_c)M^2. \quad (1.5)$$

Magnetization is easy along the c-axis and equally hard along any axis normal to *c* (assume *a*). If *c* decreases until it equals *a*, the specimen becomes spherical ($N_a = N_c$, $K_s = 0$) and shape anisotropy disappears.[2]

1.4 Ferromagnetic Materials

1.4.1 Soft Magnetic Materials

Soft magnetic materials can be easily magnetized and demagnetized by low-strength magnetic field. When an applied field is removed, soft magnetic materials will return to a state of relatively low residual magnetization. Soft magnetic materials are used primarily to enhance or channel the flux produced by an electric current. The main parameter, which is often used as a figure of merit for soft magnetic materials, is the relative permeability, which is a measure of how readily the material responds to the applied magnetic field. The other main parameters of interest are the coercivity, the saturation magnetization, and the electrical conductivity. As shown in Figure 1.7, typical soft materials have very low intrinsic coercivity and high saturation magnetization M_s but low M_r.

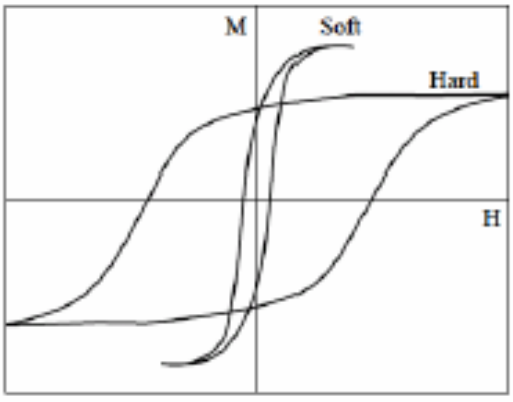

Figure 1.7 Typical *M-H* curves for soft and hard magnets.

1.4.2 Hard Magnetic Materials

Hard magnets, also referred to as permanent magnets, are magnetic materials that can retain their magnetism after being magnetized. The term “hard” is used to describe materials that have sufficiently high resistance to demagnetizing field. Coercivity is therefore the key to distinguishing between hard and soft phase magnetic materials. As shown in Figure 1.8, materials that have an intrinsic coercivity of greater than 1000 Oe and typically high remanence M_r are hard magnetic materials. Such material have high energy product $(BH)_{max}$, which is the figure of merit of permanent magnet.

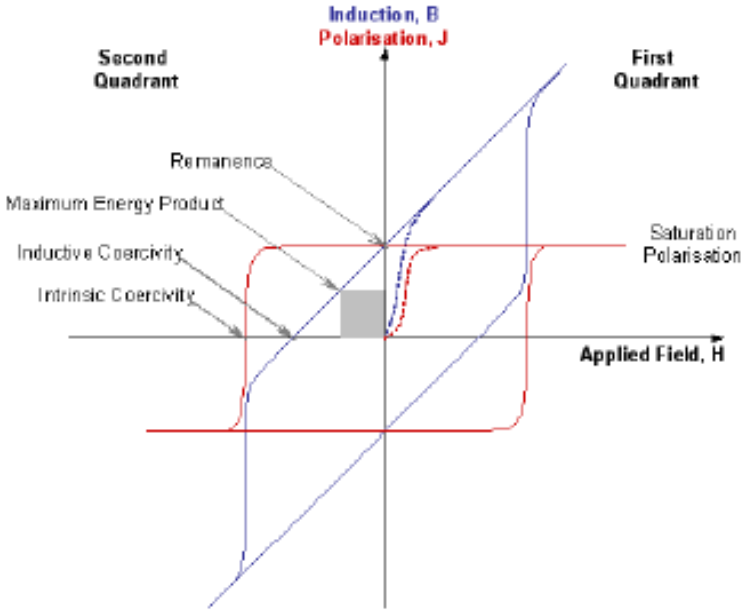

Figure 1.8 Typical *M-H* and *B-H* loops of ferromagnetic materials.[10]

Maximum Energy Product $(BH)_{max}$: In *B-H* loop, the maximum value of the product of *B* and *H* is called the maximum energy product, ($(BH)_{max}$) and is a measure of the maximum amount of useful work that can be performed by the magnet. Its unit is KJ/m^3 (MGOe). For a permanent magnetic material, the $(BH)_{max}$ is twice the maximum magnetostatic energy available from a magnet of optimal shape. The product tends to increase with both increasing coercive field

H_c and saturation magnetization *Ms.* However, for materials with sufficiently high H_c values ($H_c > 2\pi M_s$), the theoretical limit for the energy product is limited only by M_s and is given by:[11]

$$(BH)_{max} \leq (2\pi M_s)^2. \qquad (1.6)$$

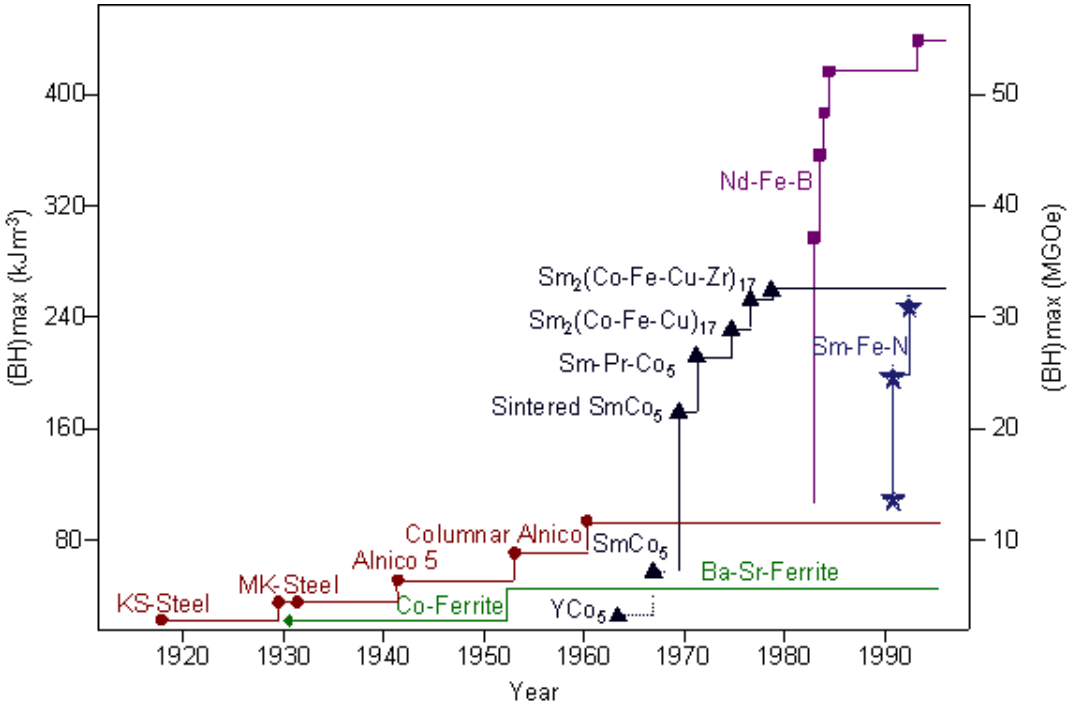

Figure 1.9 Progress in the energy product of permanent magnets in the 20th century.[10]

1.4.3 Exchange-coupled Hard/Soft Nanocomposite Magnets

Driven by the limitation in equation (1.6) $(BH)_{max} \leq (2\pi M_s)^2$, research has been focused on developing new high-anisotropy materials with high M_s and Curie temperature (Tc). Thus, new hard-magnetic compounds such as $SmCo_5$, Sm_2Co_{17}, and $Nd_2Fe_{14}B$ are made. Unfortunately, these compounds still have magnetization values significantly lower than that of Co, Fe, or $Fe_{65}Co_{35}$, which have $4\pi M_s$ values of 18, 21, and 24 kG, respectively.[11] In 1991, Kneller and Hawig[12] proposed an alternative approach to enhance the transition metal content to increase *Ms* by making a nanocomposite of exchange-coupled hard and soft magnetic phases. Such magnets are referred as exchange-spring magnets and provide a new approach to increased $(BH)_{max}$. The

hard phase provides the requisite magnetic anisotropy and stabilizes the exchange-coupled soft phase against demagnetization, and the soft phase provides the high magnetization (as shown in Figure 1.10).[13-15]

Exchange-coupled nanocomposite was first observed by Coehoorn *et al*.[16] in a melt-spun $Nd_{4.5}Fe_{77}B_{18.5}$ sample that, when annealed, consisted of a mixture of $Nd_2Fe_{14}B$, Fe_3B, and Fe phases. Skomski and Coey explored the theory of exchange-coupled films and predicted that a giant energy product of 120 MGOe might be attainable by exploiting the exchange-spring mechanism in oriented nanostructured magnets.[17-19] It has also been predicted that, for effective exchange coupling, the grain size of soft phase should not be larger than twice the domain-wall thickness of hard phase. Future applications of exchange-spring magnets will likely be based on a nanoscale dispersed composite geometry obtained in bulk processing.[19-21]

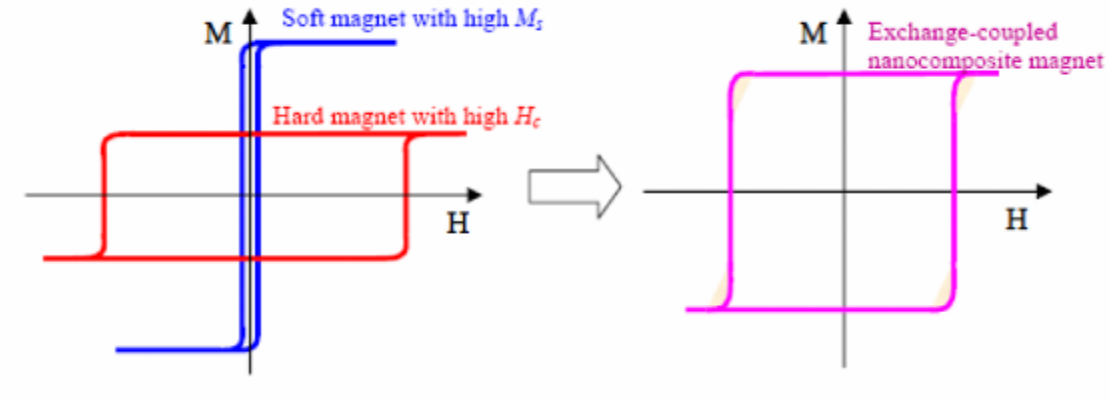

Figure 1.10 Hysteresis loops of soft, hard, and hard/soft nanocomposite magnets.

1.5 Magnetism of Ferromagnetic Nanoparticles

Ferromagnetic nanoparticles (also called as magnetic nanoparticles) exhibit a variety of unique magnetic phenomena that is drastically different from those of their bulk counterparts because of the high surface to volume ratio of the particle at nanometer scale. Magnetic properties of small ferromagnetic particles, such as coercivity and saturation magnetization, are mainly dominated by two key features: (1) a size limit below which the specimen cannot be

broken into domains, and so it remains with single domain; and (2) the thermal energy in small particles, which decouples the magnetization from the particle itself to give rise to the phenomenon of superparamagnetism. These two key features are represented by two key sizes (on the length scale): the single domain size and the superparamagnetic size as shown in figure 1.11.[2, 9]

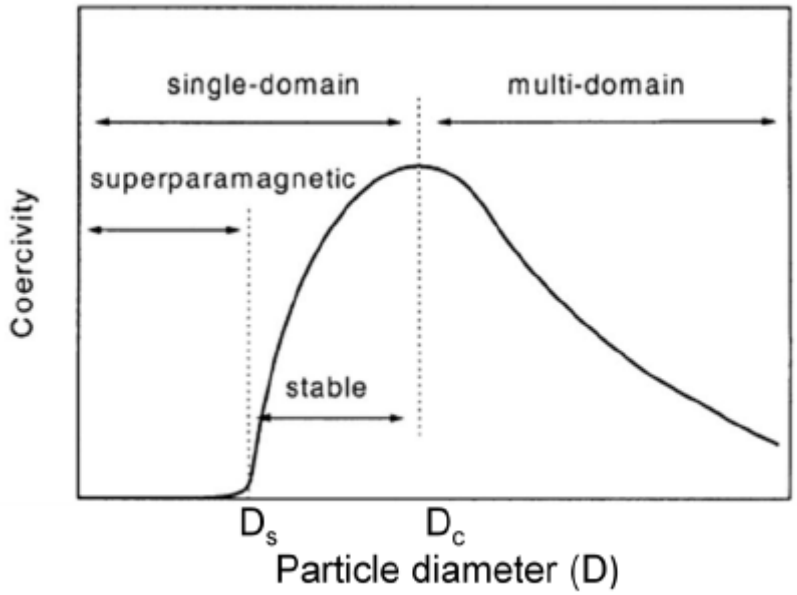

Figure 1.11 Variation of coercivity with particle diameter.

1.5.1 Single-Domain Particles

The magnetostatic energy of a ferromagnet could be decreased by restructuring the material into domains. There is a limit to this because the formation of domains costs energy as a result of domain wall formation. Thus, in a large body there could be minimum domain size below which the energy cost of domain formation exceeds the benefits of decreasing the magnetostatic energy. When the size of the magnets decreases to a critical particle diameter, the formation of domain walls is energetically less favorable, and the magnets have only a single domain. Magnetization reversal in single-domain particle occurs via spin rotation, since there are no domain walls to move. Single-domain particles consequently have a larger coercivity compared to

multidomain system as it is harder to rotate the magnetization than to move a domain wall.[2,9] In this single-domain regime, the magnetic coercivity increases as the size of the nanoparticle increases (Figure 1.11) with the relationship:

$$H_c = 2K/m_s[1 - 5(k_BT/KV)^{1/2}], \quad (1.7)$$

where m_s is the saturation magnetization.[22] Above the critical size ($D > D$c), multidomain magnetism begins in which a smaller reversal magnetic field is required to make the net magnetization zero. Saturation magnetization of nanoparticles is also strongly dependent on their size. Magnetic materials intrinsically possess magnetically disordered spin glass-like layers near the surface due to the reduced spin–spin exchange coupling energy at the surface.[23,24] In bulk cases, since the disordered surface layer is minimal compared to the total volume of the magnet, such surface spin canting effects are negligible. Upon reduction of the size of magnetic materials to the nanoscale regime, however, the surface canting effects are dramatically pronounced in the saturation magnetization value (m_s), described as:

$$m_s = M_S[(r - d)/r]^3, \quad (1.8)$$

where r is the size, M_S is the saturation magnetization of bulk materials, and d is the thickness of disordered surface layer.[23] For very small nanoparticles (less than ~5 nm) such size effect on m_s is more noticeable, since internal spins of the nanoparticle also start to be canted as do the surface spins because of increased interactions between the surface and internal spins.[23]

1.5.2 Superparamagnetism

Superparamagnetism is a phenomenon where magnetic materials exhibit a behavior similar to paramagnetism at temperatures below the Curie or the Neel temperature. Superparamagnetism occurs when the material is composed of very small crystallites (1-20 nm). In this case even though the temperature is below the Curie or Neel temperature, the thermal energy is sufficient to overcome the coupling forces between neighboring atoms, and to change the direction of magnetization of the entire crystallite. The material behaves in a manner similar to paramagnetic materials and the magnetic moment of the entire crystallite tends to align in a random way without a magnetic field. The energy required to change the direction of

magnetization of a crystallite is called the crystalline anisotropy energy (*KV*) and depends both on the materials properties and the crystallite size. As the crystallite size decreases, so does the crystalline anisotropy energy, resulting in a decrease in the temperature at which the material becomes superparamagnetic.[2,9] A typical hysteresis loop of superparamgnetic nanoparticles is shown in Figure 1.12 with Hc =0 and M_r/ M_s =0.

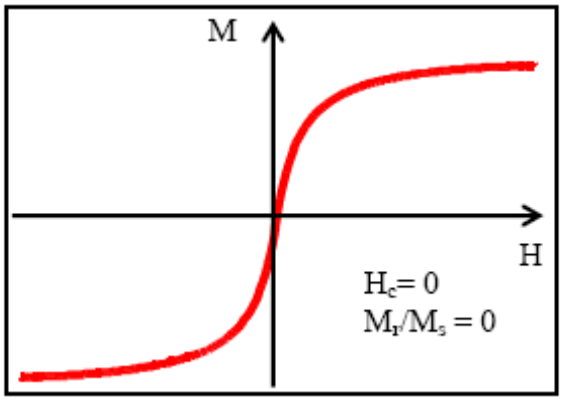

Figure 1.12 A typical hysteresis loop for superparamagnetic particles.

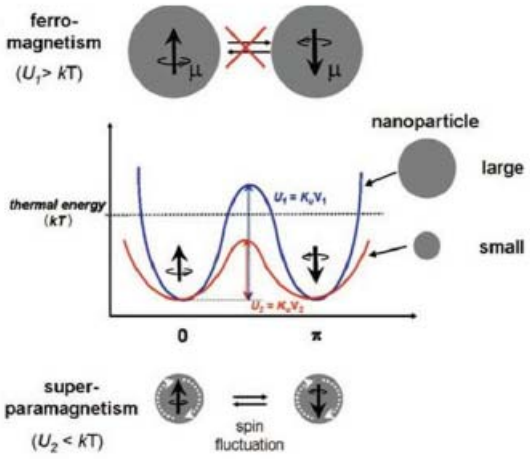

Figure 1.13 Energy diagram of magnetic nanoparticles with different magnetic spin alignment, showing ferromagnetism in a large particle (top) and superparamagentism in a small nanoparticle (bottom).[25]

The phenomenon of superparamagnetism is timescale-dependent due to the stochastic (random variable) nature of the thermal energy. The time scale for a successful jump can be calculated by:

$$\tau = \tau_o e^{-KV/k_B T} \qquad (1.9)$$

where the attempt timescale (τ_o) is about 10^{-9} s, and V is the volume of the particle. This equation (1.9) describes the time scale over which the moment of the particles ($\mu_p = M_s V$) attampts to jump the anisotropy energy (KV) barrier as shown in Figure 1.13.

Typical experiments with a magnetometer take 10 to 100 s; if Ms reversed at times shorter than the experimental time scale, the system appears superparamagnetic. Using τ =100 s and τ_o=10^{-9} s, we can obtain the critical volume from equation (1.9):[2]

$$V_{sp} = 25k_B T / K. \qquad (1.10)$$

A particle with a volume smaller than this quantity acts superparamagnetically on the 100 s experimental timescale. Equation (1.10) can be rearranged to yield

$$T_B = KV / 25k_B. \qquad (1.11)$$

T_B is called the blocking temperature; below T_B, the free movement of the moment of particles ($\mu_p = M_s V$) is blocked by the anisotropy; above T_B, $k_B T$ kicks the moment loose so that the system appears superparamagnetic. Blocking temperature (T_B) which is characteristic for ferromagnetic to superparamagnetic transition can be ascertained in nanoparticles by measuring the zero field cooling (ZFC) and field cooling (FC) magnetization temperature as shown in Figure 1.14. As the particles cool in a zero applied field, they will tend to magnetize along preferred crystalline directions in the lattice, thus minimizing the magneto-crystalline energy. Since the orientation of each crystallite varies, the net moment of the system will be zero. Even when a small external field is applied, the moments will remain locked in the preferred crystal directions, as is seen in the low temperature portion of the ZFC curve. As temperature increases, more thermal energy is available to disturb the system. Therefore, more moments will align with the external field

direction in order to minimize the Zeeman energy term. In other words, thermal vibration is providing the activation energy required for the Zeeman interaction. Eventually, the net moment of the system reaches a maximum where the greatest population of moments has aligned with the external field. The peak temperature is called the blocking temperature (T_B). As temperature rises above T_B, thermal vibrations become strong enough to overcome the Zeeman interaction and thus randomize the moments.

Field cooled (FC) measurements proceed in a similar manner to ZFC, except that the constant external field is applied while cooling and heating. However, the net moment is usually measured while heating. The FC curve will diverge from the ZFC curve at a point near the blocking temperature as seen in Figure 1.14. This divergence occurs because the spins from each particle will tend to align with the easy crystalline axis that is closest to the applied field direction, and will remain frozen in that direction at low temperature.

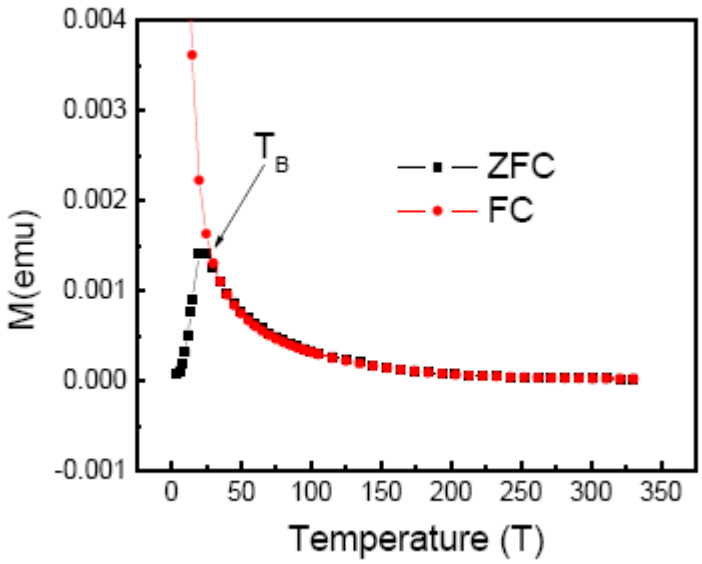

Figure 1.14 Typical ZFC and FC curves showing the blocking temperature of nanoparticles.

CHAPTER 2

MAGNETIC NANOPARTICLES

Magnetic nanoparticles with sizes ranging from 2 to 20 nm in diameter represent an important class of artificial nanostructured materials because their magnetic properties change drastically with their size. This chapter first focuses on physical and chemical approaches to synthesize magnetic nanoparticles. Then we talk about the techniques used (in our experiments) to characterize these nanoparticles. Finally, we talk about the applications of these nanoparticles in various fields such as data storage, high energy magnets, biomedicine etc.

2.1 Synthesis of Magnetic Nanoparticles

A series of general methods for the magnetic nanoparticle synthesis have now been developed.[26] An essential feature of their synthesis is the preparation of particles of specified size and shape (at least, the size distribution should be less than 5-10%, and controllable). The shape control and the possibility of synthesis of anisotropic magnetic structures are especially important. In order to eliminate (or substantially decrease) the interparticle interactions, magnetic nanoparticles often need to be isolated from one another by immobilization on a substrate surface or in the bulk of a stabilizing inert matrix. It is important that the distance between the particles in the matrix should be controllable. Finally, the synthetic procedure should be relatively simple, inexpensive and reproducible. The methods of generation of magnetic nanoparticles in the gas or solid phase using high-energy treatment of the material are usually called physical, while the nanoparticle syntheses, which are often carried out in solutions at moderate temperatures are chemical methods.

2.1.1. Physical Methods

2.1.1.1 Condensation Methods

The method of nanoparticle synthesis from supersaturated metal vapors is based on the classical nucleation theory in which the nascent phase clusters are described by the spherical liquid drop model. Nanoparticles (clusters) are prepared using various ways of metal evaporation: laser vaporisation,[27, 28] thermal vaporisation,[29,30] arc discharge, plasma vaporisation,[31] and solar energy- induced evaporation.[32] In each method, special installations are employed differing in engineering solutions of particular units.[33]

For example, in the classical thermal vaporization method, a metal or alloy sample is heated in a tungsten boat in an argon or helium stream. The atoms of the vaporized metal lose kinetic energy upon collisions with inert gas atoms, gather in clusters and condense on a cooled substrate as a nanodispersed powder. By varying the evaporation rate, the substrate temperature and gas pressure and composition, one can control the particle size in the 100± 3 nm range. Most often, prior to opening the installation and taking out the sample, nanoparticles are passivated by passing an inert gas/ oxygen mixture for several minutes. In particular, this method has been used to prepare heterometallic nanoparticles (~30 nm) with the composition Fe-M (M=Ni, Mn, Pt, Cr).[29]

2.1.1.2 Mechanical Milling

The mechanochemical dispersion of a compact material in mills of various designs appears an attractive way to produce disperse systems. However, there exists a mechanical dispersion limit for solids,[34, 35] which prevents in some cases the preparation of nano-sized particles with a narrow dispersion. In addition, high energy impact on the material being ground result in intensive interaction of the nanoparticles formed with the dispersion medium. The morphology of the nanoparticles can be controlled by changing milling speed, time, type and size of grinding medium (balls), milling media, milling temperature etc.

2.1.1.3 Electrochemical Generation

This method is used as a method for the synthesis of substantial amounts of rather small (~2 nm) nanoparticles with a narrow dispersion.[36] A standard electrochemical cell containing an alcohol solution of tetraalkylammonium halide was used to obtain cobalt particles. On passing the current, the cobalt anode dissolved to give Co nanoparticles near the cathode (glass carbon). The influence of electrolysis conditions on the magnetic characteristics of the resulting nanoparticles was studied using several examples. The average size of a particle formed upon electrochemical dispersion was inversely proportional to the current density. Evaporation of the solvent yields crystallites, which can be readily converted again into a colloid suspension. The electrochemical process has been used to obtain γ-Fe_2O_3 nanoparticles (8 ± 3 nm), stable in organic solvents due to adsorption of cationic surfactants.[37]

2.1.2 Chemical Methods

Diverse metal-containing compounds (MCC) including metal carbonyls, organometallic compounds, metal carboxylates, etc., are used as the precursors in the chemical synthesis of magnetic nano- particles. Most often, precursors decompose on heating or UV irradiation; other types of treatment of MCC, resulting in nanoparticles, have also been developed.

2.1.2.1 Thermal Decompositions of Metal-containing Compounds

Thermal decomposition of metal-containing compounds has been studied in detail in relation to the development of the scientific grounds of the metal organic chemical vapor deposition (MOCVD) technique, which is used successfully to obtain nanoparticles. When the reaction is carried out in a liquid medium in the presence of surfactants or polymers, it is possible to stabilize the resulting amorphous nanoparticles with diameters of up to 10 nm. An interesting example of two-stage thermolysis of $Fe(CO)_5$ has been reported.[38] First, an iron oleate complex is formed from $Fe(CO)_5$ and oleic acid at 100 ºC; at 300 ºC, the complex decomposes to give primary `loose' nanoparticles (11 ± 4 nm). After maintaining at 500 ºC, these are converted, as shown by powder X-ray diffraction, into crystalline α-Fe nanoparticles. Laser photolysis of volatile MCC (most often, metal carbonyls) is also suitable for this purpose.[39]

2.1.2.2 Ultrasonic Decomposition of Metal-containing Compounds

In this method, metal carbonyls and their derivatives are used as metal-containing compounds, although cases of successful use of other organometallic compounds are also known. Nanoparticles are synthesized by ultrasound-induced decomposition of a solution of MCC in solvent. In order to retain the monodispersity and prevent aggregation of the particles formed, suitable surfactant is added to the solution. Ultrasonic decomposition of iron pentacarbonyl in polyvinylpyrrolidine resulted in amorphous γ-Fe_2O_3 nanoparticles. Their dimensions were determined by the nature and concentration of the surfactants present in the solution.[40]

2.1.2.3 The Reduction of Metal-containing Compounds

Magnetic metallic nanoparticles can be prepared from metal salts using strong reducing agents, namely, alkali metal dispersions in ethers or hydrocarbons, alkali metal complexes with organic electron acceptors (e.g., naphthalene), $NaBH_4$ and other complex hydrides. By using $NaBH_4$ in aqueous solutions at room temper-ature, both homo- (Fe, Co, Ni) and heterometallic (FeCo, FeCu, CoCu) nanoparticles were obtained as amorphous powders containing substantial amounts of boron (20 mass% or more). High-boiling alcohols are also used as reducing agents. The reduction of cobalt acetate with dodecane-1,2-diol at 250 ºC in oleic acid in the presence of trioctylphosphine gives 8 ± 3 nm Co particles.[41] nickel-containing nanoparticles have been prepared in a similar way.[42]

2.1.2.4 Synthesis in Reverse Micelles

Recent years were marked by intensive development and wide use of the synthesis nanoparticles in nano-sized `reactors' as the size of `nanoreactors' can be controlled within certain limits. A micelle is an example of these nanoreactors. Reverse micelles are tiny drops of water stabilized in a hydrophobic liquid phase due to the formation of a surfactant monolayer on their surface. Owing to the exactly measured amount of MCC in each micelle (as the nanoparticle formation occurs without substance supply from the outside), it is possible not only to control the composition and the average size of the particles but also to obtain monodisperse samples with a narrow particle size distribution. Co nanoparticles were synthesized by mixing two colloid

solutions of reverse micelles with the same diameter (3 nm), one containing $CoCl_2$ and the other containing sodium tetrahydroborate of the same concentration.[43] Magnetic nanoparticles with an average diameter of 5.8 nm and a polydispersity of 11% were obtained in hexane as a colloid dispersion stable against aggregation and oxidation during a week. Syntheses of cobalt nanoparticles in reverse micelles are described in detail in the literature.[44]

2.1.2.5 Sol-gel Method

The sol-gel method is widely used in a number of technologies.[45] In nanotechnology, it is used most often to obtain metal oxides but is also applicable to the synthesis of nanosized metals and fused bimetallic and heteroelement particles. For example, reduction of Ni^{2+} and Fe^{2+} ions inserted in silica gel in 3 : 1 ratio with hydrogen resulted in Ni_3Fe nanoparticles (19 ± 4 nm) within the SiO_2 matrix.[46]

2.2 Characterization of Magnetic Nanoparticles

Transmission electron microscopy (TEM), high resolution TEM (HRTEM), scanning electron microscopy (SEM), and powder and X-ray diffraction (XRD) were used for structural characterization. Inductively coupled plasma-optical emission spectroscopy (ICP-OES) and energy dispersive X-ray (EDX) were used for compositional characterization of nanoparticles before and after annealing. An Alternating gradient magnetometer (AGM) and a superconducting quantum interference device (SQUID) magnetometer were used for magnetic characterization. A brief description of these equipments and characterization techniques and the techniques used to prepare samples are following.

2.2.1 X-ray Diffraction (XRD)[47]

Philips PW 1710 x-ray diffractometer with Cu-Kα radiation (wavelength λ=1.54056 Å) was used for crystalline structure characterization of samples. The samples were prepared by drop casting dispersions of nanoparticles in non polar solvents such as hexane or heptane on either a glass substrate or silicon wafer. The samples were dried under ambient conditions protected with a Petri dish cover to eliminate unintended contamination from air borne particles. Samples were

then inserted in the sample holder and analyzed typically between 20 – 90 2θ degrees. The incident x-ray follows Bragg's law as described in figure 2.1 and the following formula:

$$n\lambda = 2d \sin\theta \qquad (2.1)$$

When a monochromatic x-ray beam with wavelength λ is projected onto a crystalline material at an angle θ, diffraction occurs only when the distance traveled by the rays reflected from successive planes differs by a complete number *n* of wavelengths. By varying the angle θ, the Bragg's Law conditions are satisfied by different *d*-spacing in materials. Plotting the angular positions and intensities of the resultant diffracted peaks of radiation produces a pattern that is characteristic of the sample. Usually 2θ is used instead of θ. If equation (2.1) is rearranged to the following form considering a first order reflection:

$$\theta = \sin{-1}\ (\lambda/2d) \qquad (2.2)$$

The distance between lattice planes can be calculated using the following formula:

$$d = a / (h^2 + k^2 + l^2)^{1/2} \qquad (2.3)$$

Since the lower order Miller indices result in larger interplanar spacing in equation (2.3), the diffraction angle in equation (2.2) will be lower. Therefore, as the Miller indices increase, the diffraction angles will also increase.

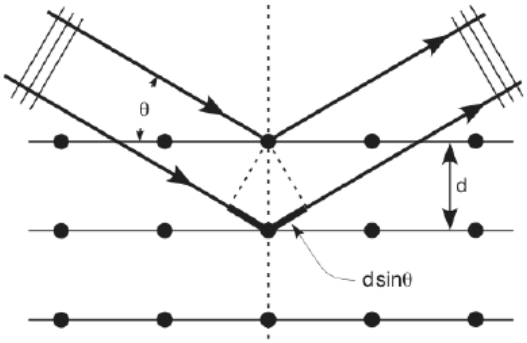

Figure 2.1 Bragg's law.

2.2.2 Scanning Electron Microscope (SEM)

A scanning electron microscope uses a tiny electron beam to scan across the sample. In SEM, the signals are observed on the same specimen site as the incoming electron beam. As mentioned above, very thin samples are required for TEM methods, where as compact samples or bulk samples can be investigated by SEM. Valuable information about morphology, surface topology, and composition can be obtained.

For conventional imaging in the SEM, specimens must be electrically conductive, at least at the surface, and electrically grounded to prevent the accumulation of electrostatic charge at the surface. Nonconductive specimens tend to charge when scanned by the electron beam, and (especially in secondary electron imaging mode) this causes scanning faults and other image artifacts. Samples are usually coated therefore with an ultrathin coating of electrically-conducting material such as gold or gold/palladium alloy deposited on the sample either by low-vacuum sputter coating or by high vacuum evaporation. Coating prevents the accumulation of static electric charge on the specimen during electron irradiation. Grisham's EDX (Energy Dispersive X-ray) detector connected to the SEM was used for studying the elemental composition of samples. The samples were mounted on an Aluminum sample stub or Si substrates using double-sided carbon stick tabs. A thin layer of Au-Pd was also deposited on the samples to make them conductive.

2.2.3 *Transmission Electron Microscope (TEM)*[48,49]

JEOL 1200EX TEM was used for observing the morphologies and crystalline structure of nanoparticles. This TEM uses an acceleration voltage of 120 kV and can reach a magnification up to 500k times. Bright field images as well as the selected area electron diffraction (SAED) patterns were captured onto negative films, which were then developed and scanned as digital images. A 300-mesh copper grid with a carbon film deposited on a formvar backing, purchased from Ted Pella, were used for preparing TEM samples. A drop of the nanoparticle dispersion solution in octane was put on the formvar side of the TEM grid. The solvent was allowed to evaporate in air and assemble on the grid. However, for TEM imaging of nanoparticles, it is

important to avoid excessive surfactant coating, which reduces the contrast and quality of the observation of nanoparticles.

The high acceleration voltage generates electrons that are collected by the condenser lenses. The electron beam then transmits through the specimen and the objective lens creates images of the specimen. Projective lens then projects the image on the fluorescent screen. By tuning the objective lens and projective lens, magnification and focus can be adjusted respectively. Images are recorded on the negative films by the camera installed at the bottom portion of the TEM. In the image mode of TEM, if the transmitted beam of electrons through the specimen is chosen to create images, then it is called bright field image. On the other hand, it is called dark field image if the diffracted beam is chosen. The selected area electron diffraction (SAED) pattern will be showed if the diffraction mode of TEM is set.

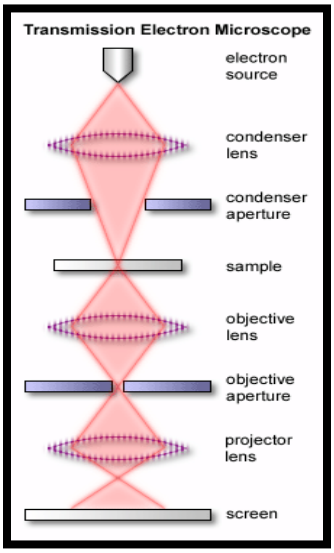

Figure 2.2 A typical structure and optics of TEM.

High-resolution TEM imaging of selected samples were performed by Hitachi HF 2000 TEM at Georgia Institute of Technology. Sample preparation for HRTEM analysis is the same as that for TEM.

2.2.4 Inductively Coupled Plasma-optical Emission Spectroscopy (ICP-OES)

Inductively coupled plasma-optical emission spectroscopy (ICP-OES) analysis on composition of selected powder samples were processed by Galbraith Research Labs. This technique uses plasma of argon that contains a large amount of cations and electrons. Temperatures within the plasma can reach up to 10,000 K, allowing the sample to fully ionize whether injected into the plasma either as an aerosol, thermally generated vapor or fine powder. Recombination with electrons within the plasma generates characteristic x-rays associated with the ions present. A spectrophotometer can then detect the wavelength and intensity of the emission allowing determination of multiple elements and relative quantities within the sample.

2.2.5 Alternating Gradient Magnetometer (AGM)

In an AGM measurement, the sample is mounted on an extended rod attached to a piezoelectric element and then placed at the center of the poles that generates magnetic field. An alternating gradient magnetic field is generated which produces an alternating force on the sample. This force (F) is proportional to the magnitude of the alternating magnetic field (B) and the magnetic moment (m) of the sample. Thus,

$$E = -m \cdot B \tag{2.4}$$

$$F_x = -(dE/dx) = m\, dB/dx \tag{2.5}$$

This force is converted into a proportional voltage by a piezoelectric element and hence the moment of the sample can be measured. The applied field is measured by a Hall probe sensor and the sensitivity of the AGM can reach up to 10 nemu. Samples with dimension up to 5 mm x 5 mm can be measured in AGM. The maximum magnetic field that can be applied by AGM is limited to 14 kOe and it can only be operated at room temperature. Therefore, samples that have high anisotropy or require low or high temperature measurements will need magnetometers that can provide much higher saturation field to get accurate magnetic measurements and capability of operating in different temperatures.

Figure 2.3 Princeton Measurements Corporation Alternating Gradient Magnetometer.

2.2.6 Superconducting Quantum Interference Device (SQUID) Magnetometer

SQUID uses a superconducting magnet, through which large amount of current can flow so that large magnetic field can be generated. The magnetic measuring mechanism of SQUID belongs to an inductive technique. During magnetic moment measurement, the sample moves through a system of superconducting detecting coils and the magnetic moment of the sample causes change in magnetic flux associated with the detecting coils, resulting in electric current produced in the detecting coils. The detecting coils are connected to the SQUID sensor, which functions as a highly linear current-to voltage converter, producing very accurate variations in the output voltage that is proportional to the moment of the sample. The SQUID can generate a magnetic field as high as 70 kOe and can be operated in temperatures from 2 K to 400 K. The sensitivity of SQUID is 10 nemu up to applied field of 2.5 kOe and 0.6 μemu above that. Liquid helium is required to operate SQUID, which makes the use of it expensive. Sample dimension requirements of SQUID are almost the same as AGM, but the sample for SQUID can be longer in one of its dimensions. AGM is much easier, faster, and less expensive to operate comparing to SQUID. Hence, room-temperature measurements of all samples that can be saturated below 14 kOe should be measured by AGM.

.

Figure 2.4 Quantum design SQUID magnetometer.

2.3 Applications of Magnetic Nanoparticles

Nanoparticles exhibit unique mechanical, optical, electronic, magnetic and chemical properties that are drastically different from those of their bulk counterparts.[50-52] These novel properties arise from the large fraction of atoms that lies on the surface of the particles and from the finite number of the atoms within each particle. Magnetic nanoparticles are of special interest, owing to their unique magnetic properties as a result of their reduced size (< 100 nm). There are a number of potential technological applications for magnetic nanoparticles. Some of them have been discussed in the following section, such as surface functionalized particles in biomedical applications, as particle arrays in magnetic storage media, as compacted powders in permanent magnets and in solutions as ferrofliuds.[53-66]

2.3.1 Magnetic Recording Media

Synthesis and assembly of magnetic nanoparticles have attracted great attention because of their potential application in ultra-high-density magnetic recording.[59] Continued increases in the areal density of hard disk drives will be limited by thin-film media in which each bit of information is stored over hundreds of grains (Figure 2.5). Self-assembled nanoparticle

media and patterned media in which data are stored in an array of single-domain magnetic particle have been suggested as a means to overcome this limitation and to enable recording density up to 1 Tbit/in^2.[60] In such ultra-high-density media, small material grain and a narrow size distribution are required because of high recording density. To obtain both a high signal-to-noise ratio and

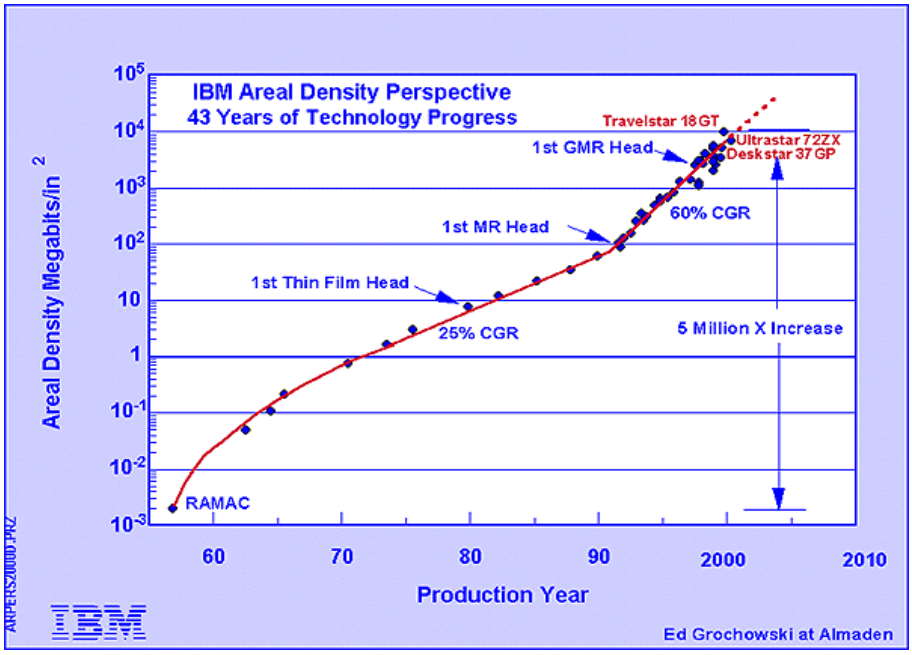

Figure 2.5 Recent developments in magnetic recording media in last 50 years.

thermal stability of the media, isolated, non-interacting, or very weekly interacting nanoparticles with very high magnetic anisotropy energy K_u are required.[61] Extensive research is being done on $CoFe_2O_4$ and FePt nanoparticles for high-density recording media.[61,63] $CoFe_2O_4$ nanoparticle is a well-known material with a very high cubic magnetocrystalline anisotropy, good coercivity, and moderate saturation magnetization.[63-65] $L1_0$ FePt nanoparticles are one of the best candidates for ultra-high-density recording media because of their very high magnetocrystalline anisotropy (K_u is 10^8 erg/cm^3), which is much higher than those of the currently used CoCr-based alloys.[61] This large crystalline anisotropy allows for thermally stable grain diameters down to 2.8 nm.[67]

2.3.2 Permanent Magnets

The figure of merit by a permanent magnetic material is judged, is the maximum energy product, $(BH)_{max}$. To obtain a large energy product requires large magnetization (M_s) and large coercivity (H_c). Although a great increment in maximum energy product of permanent magnets has been achieved in last century as shown in Figure 1.9, there has not been any significant improvement in the last 25 years. The last two breakthroughs in energy products have come from single phase hard magnetic materials (Figure 1.9). However, for hard materials with sufficiently high H_c values, the energy product is limited by their low Ms. As mentioned in 1.3.8, exchange-coupled nanocomposite magnets are promising candidates for advanced permanent magnetic applications, as high energy products $(BH)_{max}$ and relatively high coercivities can be developed in these nanocomposite magnets. A small grain size (less than 20 nm) and a uniform mixture of the hard and soft phases are required for effective exchange coupling between the hard and the soft phases. Zeng *et al.* demonstrated in 2002 that exchange-coupled nanocomposite magnet such as FePt-Fe_3Pt can be made using monodisperse nanoparticles of FePt and Fe_3O_4 as precursors by self assembly technique.[21] In the exchange-coupled isotropic FePt-Fe_3Pt nanocomposite, the energy product of 20.1 MGOe was achieved, which is 50% higher than that expected theoretically from a single phase, nonexchange-coupled isotropic FePt. An anisotropic nanocomposite magnet with both the hard and soft phases aligned is expected to show a much higher energy product than the isotropic one.[12, 13] However, controlling the morphology including grain size and grain alignment, in nanocomposite magnet remains a great challenge.[56]

2.3.3 Biomedical Applications

Magnetic nanoparticles have been proposed for biomedical applications for several years.[54, 66] In recent years, nanotechnology has developed to a stage that makes it possible to produce, characterize, and specifically tailor the functional properties of nanoparticles to applications. This shows considerable promise for applications in biomedical and diagnostic fields, such as targeted drug delivery, hyperthermic treatment for malignant cells, and magnetic

resonance imaging (MRI).[52, 54-56, 66] There are three reasons why magnetic nanoparticles are useful in biomedical applications. First, the size of magnetic nanoparticles can be controlled, ranging from a few nanometers up to tens of nanometers and are thus smaller in size than a cell (10-100μm), a virus (20-450 nm), a protein (5 -50 nm) or a gene (2nm wide and 10 - 100 nm long). Magnetic nanoparticles can get close to cells and genes, and they can be coated with biomoleclues to make them interact or bind with biological entities. Second, magnetic nanoparticles can be manipulated by an external magnetic field gradient. Magnetic nanoparticles can be used to deliver a package, such as an anticancer drug, to a targeted region of the body such as a tumor. Third, magnetic nanoparticles can also be made to respond resonantly to a time-varying magnetic field, with an associated transfer of energy from the field to the nanoparticles. Magnetic nanoparticles can be made to heat up, which leads to their use as hyperthermia agents, delivering toxic amounts of thermal energy to targeted bodies such as tumors or as chemotherapy. [54-56, 66] For biomedical applications, magnetic nanoparticles must (1) have a good thermal stability; (2) have a larger magnetic moment; (3) be biocompatible; (4) be able to form stable dispersion so the particles could be transported in living system; and (5) response well to AC magnetic fields. Furthermore, better control of particle size and properties will be necessary to use these particles in biomedical applications, in which uniformity of the properties will ensure accurate doses and delivery.[66] So far, the widely used magnetic nanoparticles for biomedical applications are magnetite (Fe_3O_4) and related oxides, which are chemically stable, nontoxic, non-carcinogenic, and have attractive magnetic properties.[58]

2.3.4 Ferrofluids

A ferrofluid is a special solution of magnetic nanoparticles in a colloidal suspension whose flow can be controlled by magnets or magnetic fields.[68] Particles are coated with a surfactant that disperses the particles and prevents agglomeration by overcoming the van der Waals forces that exist between the particles.[58] As a result, when such a fluid is not in the presence of external magnetic field, it has zero net magnetization. When a strong magnet is brought close to the ferrofluid, several spikes will appear as the fluid arranges itself along the magnetic field lines of

the magnet. When the field is removed, the particles again disperse, randomizing their orientation and establishing no net magnetization.[59, 69] These unique properties allow ferrofluids to have applications in numerous fields of technology. The most common application of ferrofluids is the cooling of loudspeakers. The ohmic heat produced in the voice coil can be transmitted to the outer structure by the fluid which increases the cooling by a factor 3 approximately. In sealing technology, a drop of ferrofluid is put into the gap between a magnet and a highly permeable rotating shaft. In the small gap, a strong magnetic field fixes the ferrofluid, and pressure differences about 1 bar can be sealed without serious difficulties.[69] Some of the other technological applications of ferrofluids includes their being used as bearings, dampers, stepping motors and se motors, and sensors. [52, 68-70]

CHAPTER 3

SYNTHESIS AND CHARACTERIZATION OF FePt NANOPARITCLES

3.1. Introduction

FePt nanoparticles have been extensively studied in the past years due to the great potential applications in many areas including data storage, permanent magnets and biomedical technology.[71] FePt nanoparticles containing a near-equal atomic percentage of Fe and Pt are an important class of magnetic nanomaterials. They are known to have a chemically disordered face-centered cubic (fcc) structure (below 500 °C in phase diagram) or a chemically ordered face-centered tetragonal ($L1_0$) structure,[72] as shown in Figure 3.1. The fcc-structured FePt has superparamagnetic nature. The fully ordered $L1_0$-structured FePt can be viewed as alternating atomic layers of Fe and Pt stacked along the [001] direction (the c-axis in Fig. 3.1(b)). Its anisotropy constant K, which measures the ease of magnetization reversal along the easy axis, can reach as high as 10^7 Jm^{-3},[62] a value that is one of the largest among all known hard magnetic materials. This large K is caused by Fe and Pt interactions originating from spin-orbit coupling and the hybridization between Fe 3d and Pt 5d states.[73–76] These Fe–Pt interactions further render the FePt nanoparticles chemically much more stable than the common high-moment nanoparticles of Co and Fe, as well as the large coercive materials $SmCo_5$ and $Nd_2Fe_{14}B$, making them especially useful for practical applications in solid-state devices and biomedicine. There are several techniques to fabricate FePt nanoparticles, such as vacuum deposition,[77] mechanical ball milling,[78] chemical synthesis[79] and gas-phase evaporation.[80] As-synthesized, the FePt has a chemically disordered fcc structure. Hence, thermal annealing is needed to transform the fcc structure into the chemically ordered $L1_0$ structure.

The synthesis of monodisperse FePt nanoparticles of desired size, shape and properties is first step being pre-requisite of their further investigation and use for practical application. Narrow size distribution, or monodispersity, is strongly desired because magnetic properties become strongly size dependent in the nanometer size range. In contrast with all the physical deposition processes, solution-phase synthesis offers a unique way for producing monodisperse nanoparticles[52,81–84] and has also been found to be effective in synthesizing monodisperse FePt nanoparticles and nanoparticle superlattices.[79] Although many factors affect particle size and shape of nanoparticles during chemical synthesis, only few parameters have been studied for FePt system since the mechanism for size and shape control is different for each material. Hence, understanding the mechanism of the formation of FePt nanoparticles can provide clear approaches to their size, shape and size distribution control.

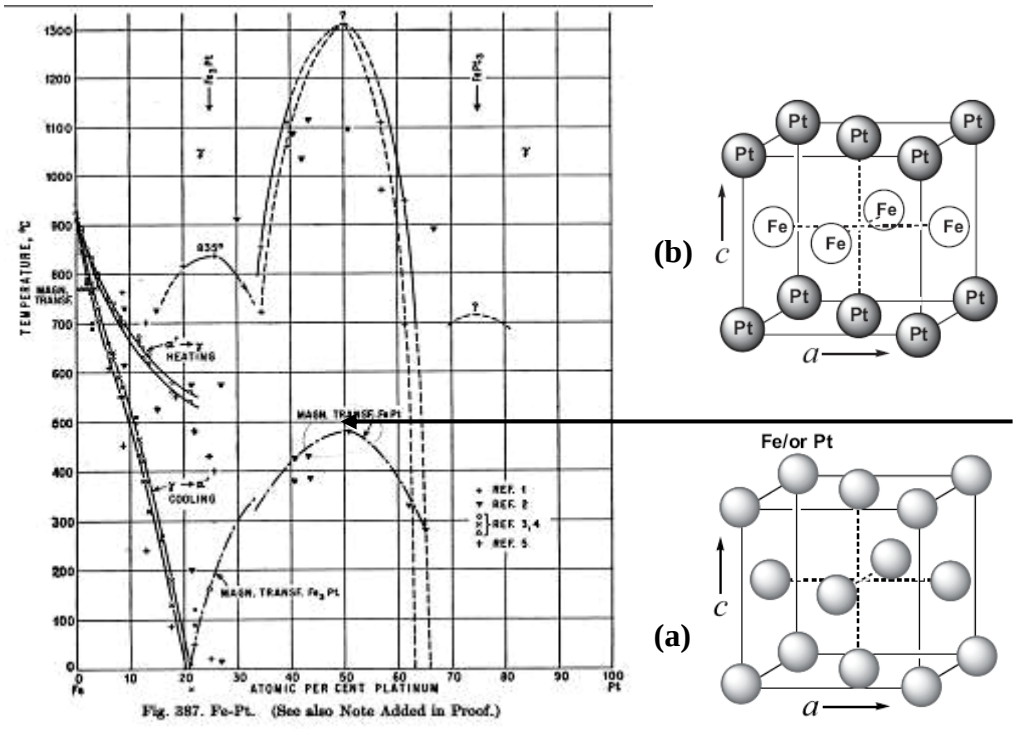

Fig. 387. Fe-Pt. (See also Note Added in Proof.)

Figure 3.1 Phase diagram of FePt alloys (left) and schematic illustration of the unit cell of (a) chemically disordered fcc and (b) chemically ordered $L1_0$ FePt.

This chapter reports the chemical synthesis and characterization of FePt nanoparticles. The size and shape of FePt nanoparticles were controlled by tuning the different reaction parameters of synthesis. The magnetic properties of FePt nanoparticles have been discussed which strongly depends on their morphology.

3.2 Experimental

3.2.1 Synthesis of FePt Nanoparticles

Thermal decomposition of organometallic precursors in the presence of surfactants at high temperatures has been quite successful in generating highly monodispersed metal nanoparticles.[81] This is because nucleation at a high temperature occurs almost instantaneously, thus the particle growth stage is well separated from the initial nucleation event. The presence of surfactant is essential in preparing nanoparticles as they inhibit agglomeration by passivating the particle surface, control their growth and help them to disperse in suitable solvent. FePt nanoparticles were synthesized by simultaneous reduction of platinum acetylacetonate ($Pt(acac)_2$) and thermal decomposition of iron pentacarbonyl ($Fe(CO)_5$) in the presence of oleic acid and oleyl amine which acted as surfactants (Figure 3.2). The method was adopted from the work of Sun *et al.*,[79] and slight modifications were made.

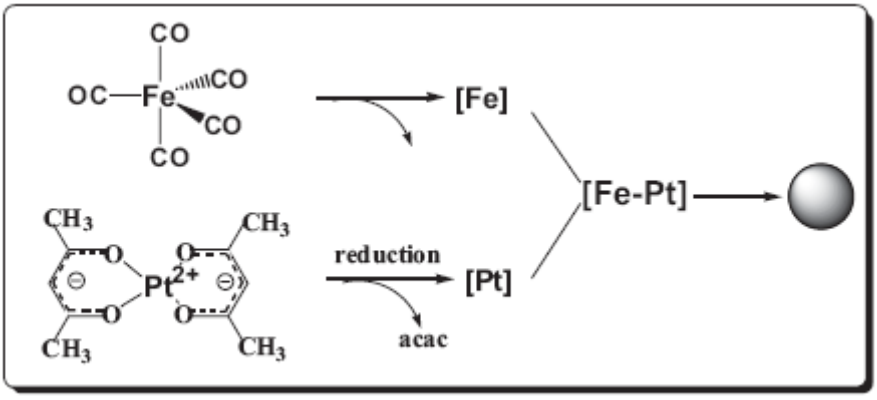

Figure 3.2 Schematic Illustration of FePt nanoparticle formation from the decomposition of $Fe(CO)_5$ and reduction of $Pt(acac)_2$.

Monodisperse FePt nanoparticles made using simultaneous chemical reduction of $Pt(acac)_2$ and thermal decomposition of $Fe(CO)_5$ have diameters in the size range of 3 to 9 nm. It is difficult to prepare FePt particles above 9 nm since Ostwald ripening doesn't seem to work for them. However, by using sequential deposition method, Platinum-iron oxide core-shell nanoparticles can be made which can be later converted to FePt nanoparticles by conventional or salt matrix annealing (explained below) in a reducing atmosphere (Figure 3.3).

The synthetic experiments were carried out using standard airless technique in argon atmosphere. In a typical procedure to prepare particles of size 2 to 9 nm, 0.5 mmol of platinum acetylacetonate was added to 125 mL flask containing a magnetic stir bar and mixed with 20 mL of octyl/benzyl ether. After purging with argon for 30 min at room temperature, the flask was heated up to 120 °C for 10 min and a designated amount of oleic acid and oleyl amine was added. Iron pentacarbonyl or iron acetylacetonate were used as an iron precursor. Iron acetylacetonate (0.5 mmol) was added at room temperature while iron pentacarbonyl (1.0 mmol) was added at 120 °C when the platinum precursor dissolved completely. The dissolution of $Pt(acac)_2$ in solvent could be followed experimentally by the change of color of the solution from off yellow to transparent yellow. After the addition of $Fe(CO)_5$, the color transition from golden to black suggested formation of nanoparticles in the solution. Then it was heated to 298 °C for 1 h before cooling to room temperature under the argon blanket. Argon gas was flowed throughout the experiment. The heating rate was varied from 1 to 15 °C per minute according to the experimental design.

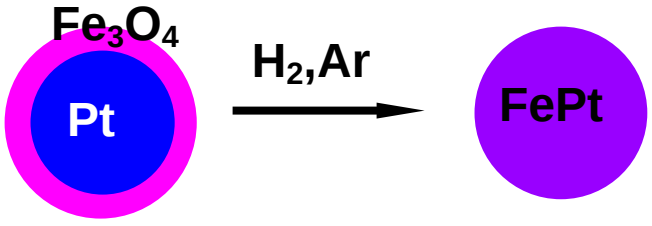

Figure 3.3 Schematic of FePt nanoparticle formation from the reduction of Pt/Fe_3O_4 core/shell nanoparticle.

The composition of the particles was controlled by changing ratio of precursors. To obtain better control in process, we examined several parameters that may have an effect on the size and shape of monodisperse FePt nanoparticles. After examining each parameter thoroughly, we found that surfactants and their concentration, type of solvents, nature of precursors, and heating rate are the key parameters which play a crucial role in size and shape control of the nanoparticles.

In a typical synthesis to prepare $Pt@Fe_3O_4$ core-shell particles, a mixture of 1,2-hexadecanediol (1.5 mmol), oleic acid (0.5 mmol), and oleylamine (0.5 mmol) in octyl ether (3 mL) was added into a 125 mL three-neck round-bottom flask under argon flow and heated to reflux temperature at 290 °C using a heating mantle. Platinum acetylacetonate ($Pt(acac)_2$) (0.5 mmol) in octyl ether (2 mL) was injected into the mixture at this temperature. The color of the reaction solution turned black immediately, indicating the spontaneous formation of nanoparticles. The reaction continued for additional 5 min, and the solution was then cooled to 220 °C. A designed amount of iron pentacarbonyl ($Fe(CO)_5$) was added using a microsyringe, and the temperature of the reaction was raised to 290 °C. The solution refluxed at this temperature for a designed period of time (5 min to 2 h) and was then cooled to ambient room temperatures.

3.2.2 Purification, Annealing and Characterization of FePt Nanoparticles

The black product from the synthesis was precipitated by adding ethanol and separated by centrifugation and redispersed in hexane. To achieve the highest purity, extra ethanol was added in this dispersion and the dispersion was centrifuged again. Because all the particles were quite homogeneous, size selection was not necessary. After washing the particles in ethanol three or more times, they were dispersed in hexane and stored in glass bottles under refrigeration. Samples for characterization were prepared by depositing a drop of the final hexane dispersion on a 3 x 3 mm silicon substrate, evaporating the solvent at room temperature and further drying in vacuum, which led to the formation of FePt nanoparticle-assembled thin

films. In conventional annealing, the samples deposited on Si substrates were then annealed at 650 °C for 1 h under the flow of forming gas (Ar + 7% H_2) in a tube furnace. To prepare TEM samples, a drop of the nanoparticle dispersion solution in octane was put on the formvar side of a 300-mesh carbon coated copper TEM grid. The solvent was allowed to evaporate slowly in air and the nanoparticles self assembled on the grid.

In salt matrix annealing, the ball-milled NaCl salt powder and fcc FePt nanoparticles (2 to 15 nm) in mass ratio of larger then 400:1 was mixed and stirred by magnetic stir bar to mix homogeneously and was continued stirring until mixture dried. The mixture was then annealed at temperatures from 700 °C for 4 hours in forming gas (93% Ar + 7% H_2) in quartz boats. After annealing, the salt was completely washed out from the samples by washing the mixtures in water and ethanol. The fine salt powder works as a separating media between the FePt nanoparticles, which keeps the particles dispersed in matrix during high temperature (700 °C) annealing, and prevents sintering and growth of the nanoparticles. Sodium chloride (NaCl) was chosen as the separating media due to its chemical stability to the FePt nanoparticles, melting point of 801 °C and high solubility in water.

The transmission electron microscopy (TEM) images were recorded on a JEOL 1200 EX electron microscope at an accelerating voltage of 120 kV. HRTEM analysis was done at Georgia Institute of Technology and images were recorded on a HITACHI HF2000 electron microscope at an accelerating voltage of 200 kV. Powder X-ray diffraction (XRD) spectra were recorded on a Philips MPD diffractometer with a Cu KR X-ray source (*i*) 1.5405 Å). The magnetic hysteresis measurements have been carried out by using superconducting quantum interference device (SQUID) magnetometer with magnetic field up to 7 T. The composition analysis was done by energy dispersive X-ray spectroscopy (EDX) and inductively coupled plasma (ICP).

3.3 Results and Discussion

3.3.1 Size control of FePt Nanoparticles

Figure 3.4 and 3.5 shows XRD patterns and TEM images of as-synthesized FePt nanoparticles of 2 to 9 nm with 1 nm difference. It can be seen from XRD patterns that the peak width decreases as the particle size increases. We can also see from the Figure 3.4 that these particles exhibit a face-centered cubic (fcc) crystal structure. As shown in Figure 3.6, the average grain size estimated from Scherrer's formula[47] for each curve in Figure 3.4 is in a good agreement with the particle size determined by statistical analysis of the TEM images (Figure 3.5) which indicates that each individual particle is a single crystal. The HRTEM of a single 7 nm

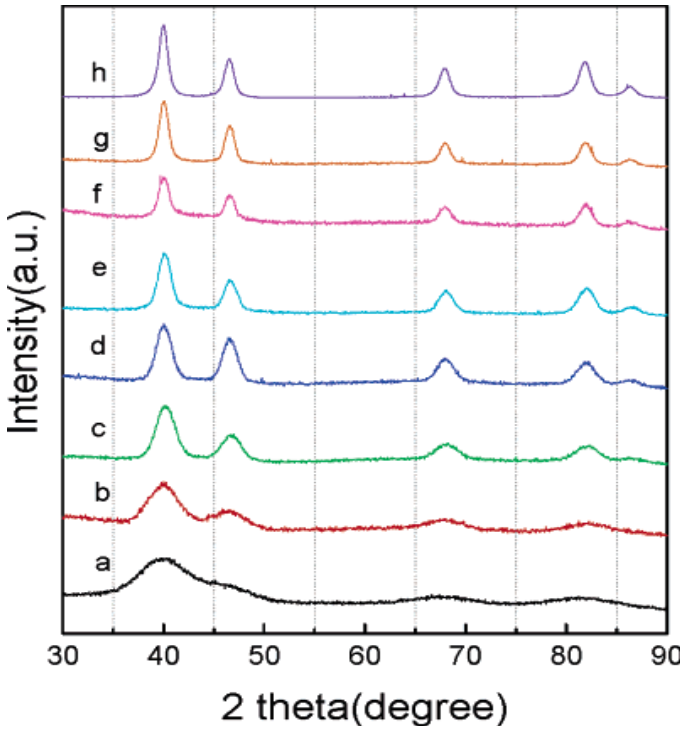

Figure 3.4 XRD curves of as-synthesized FePt nanoparticles of size (a) 2 nm, (b) 3 nm, (c) 4 nm, (d) 5 nm, (e) 6 nm, (f) 7 nm, (g) 8 nm and (h) 9 nm.

FePt nanoparticle and electron diffraction pattern reveals good crystallinity and clear lattice fringes, as shown in Figure 3.7(a) and (b), respectively. The distance between two adjacent

planes in HRTEM image was measured 0.224 nm, corresponding to (111) planes in the face-centered cubic (fcc) FePt structure.

3.3.1.1 Effect of Surfactants/Precursor Ratio

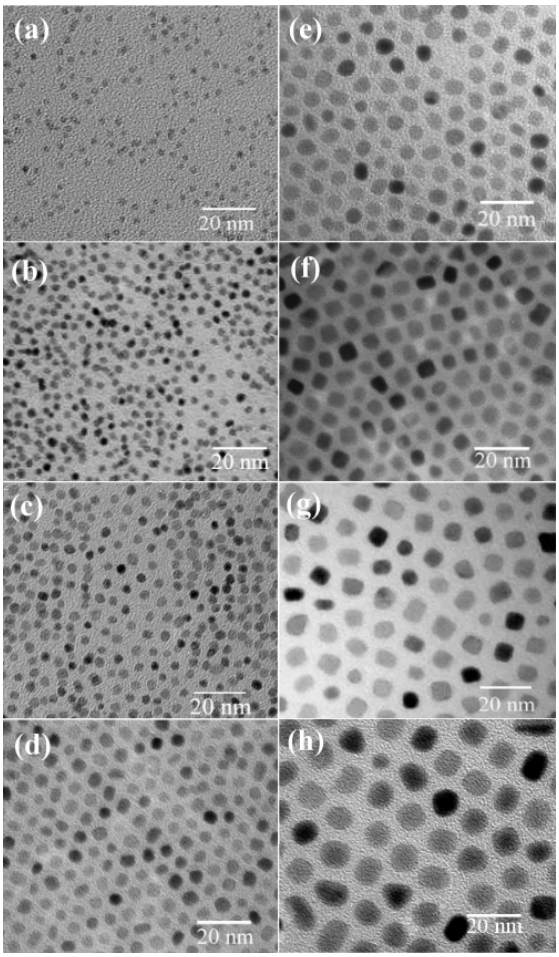

Figure 3.5 TEM images of as-synthesized FePt nanoparticles of size (a) 2 nm, (b) 3 nm, (c) 4 nm, (d) 5 nm, (e) 6 nm, (f) 7 nm, (g) 8 nm and (h) 9 nm.

Surfactants typically play a crucial role in controlling the size and shape of chemically synthesized nanoparticles. We examined the effect of the surfactants to $Pt(acac)_2$ molar ratios to observe the size of monodisperse FePt nanoparticles. The heating rate of the reaction was maintained at 5 °C/min. FePt nanoparticles with average size of 4 nm (Figure 3.5(c)) were obtained when the molar ratio of surfactants to $Pt(acac)_2$ was 1. By decreasing the molar ratio

to 0.75, the particle size decreased to 3 nm (Figure 3.5(b)) whereas by increasing the molar ratio up to 10, the particle size increased to 9 nm (Figure 3.5(h)). It is clear that the particle size increases with increasing surfactant concentration but after a certain concentration of surfactants the size did notchange (Figure 3.8). The resultant size change of the nanoparticles is thought to be the result of the change in the number of nuclei at the first step of particle formation. It is believed that the increase in the surfactant amount resulted in the formation of stable complexes with individual metal atoms of a molecular precursor. Therefore, an increase in surfactant concentration is expected to suppress the nucleation process and as a consequence, larger particle size is produced.

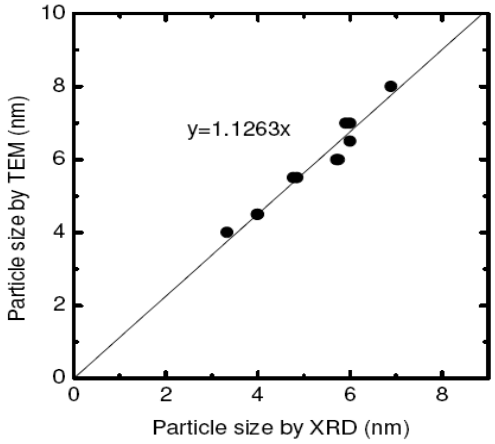

Figure 3.6 The relationship between the particle sizes obtained by TEM and calculated by XRD patterns.

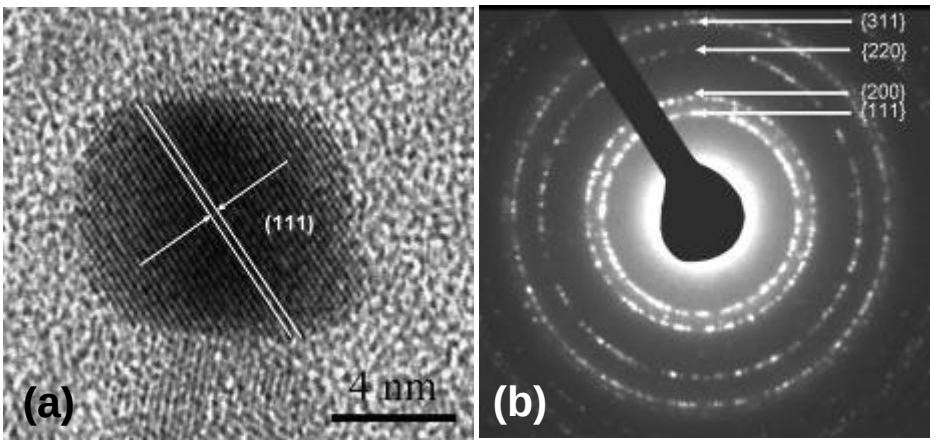

Figure 3.7 (a) HRTEM of the as-synthesized 7 nm FePt nanoparticle.and (b) Electron diffraction of as-synthesized 7 nm FePt nanoparticles showing fcc FePt pattern.

3.3.1.2 Effect of Heating Rate

The heating rate of reaction mixture was also found to be very important in the fine-tuning of the particle size. To analyze the size change with the heating rate of the reaction mixture, surfactant to precursor ratio identical to that used to synthesize 8 nm particles (Figure 3.5(g)) was chosen. As the heating rate was increased from 5 to 10 and then to 15 °C/min, we found that the average particle size was decreased from 8 to 7 and then to 6 nm (Figure 3.5(f) and 3.5(e)), respectively. With the increase in the heating rate, the nucleation rate was increased. As a result of the enhanced nucleation rate, more nuclei were formed at the initial stage. Consequently smaller particles were produced. On the other hand, the correlation between the heating rate and the particle size is not always monotonous (Figure 3.8). When the heating rate is very low, competition between the nucleation and the growth occurs and smaller particles may be produced. For example, when the heating rate was decreased to 1 °C/min, surprisingly the particle size was decreased to 5 nm. Our results suggest that nucleation rate dominates over growth rate at a very low heating rate. This competition arises due to several parameters including precursors.

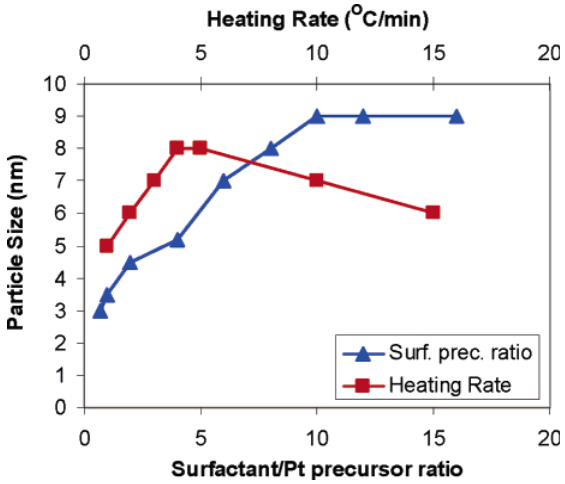

Figure 3.8 Heating rate and surfactant/Pt precursor dependence on particle size.

3.3.1.3 Effect of Precursor

$Fe(CO)_5$ was used as the iron source to synthesize particles from 3 to 9 nm. However, particle size below 3 nm was not obtained using $Fe(CO)_5$. To study the effect of precursors on the particles size, $Fe(CO)_5$ was replaced by $Fe(acac)_3$, while keeping all the synthetic conditions same. When $Fe(acac)_3$ was used, the particles of 2 nm were obtained (Figure 3.5(a)). The nature of the precursor and their physical state are believed to be the reason for the decrease in particle size. $Fe(CO)_5$ is a volatile liquid and was injected to the reaction mixture after dissolution of $Pt(acac)_2$ in octyl ether. In comparison, $Fe(acac)_3$ is a solid powder that was mixed with $Pt(acac)_2$ in octyl ether at room temperature. The reason for such small size may be a quick nucleation from precursor decomposition followed by immediate precursor depletion. The nucleation rate dominates over growth rate, and the abundance of nuclei with less growth leads to the formation of the 2 nm particles. The interesting point was that although the amount of surfactant and heating rate were varied, particle size was always found to be 2 nm when $Fe(acac)_3$ was used as the iron precursor.

3.3.1.4 Effect of Separate Reduction and Decomposition of Precursors

To prepare FePt particle of diameter larger than 9 nm size, Pt/Fe_3O_4 core-shell particles were synthesized by sequential synthesis route. Instead of simultaneous reduction and decomposition of Pt and Fe precursor respectively, first the $Pt(acac)_2$ was reduced in presence of surfactants and solvent and 10 nm Pt nanoparticles were formed. Later at intermediate

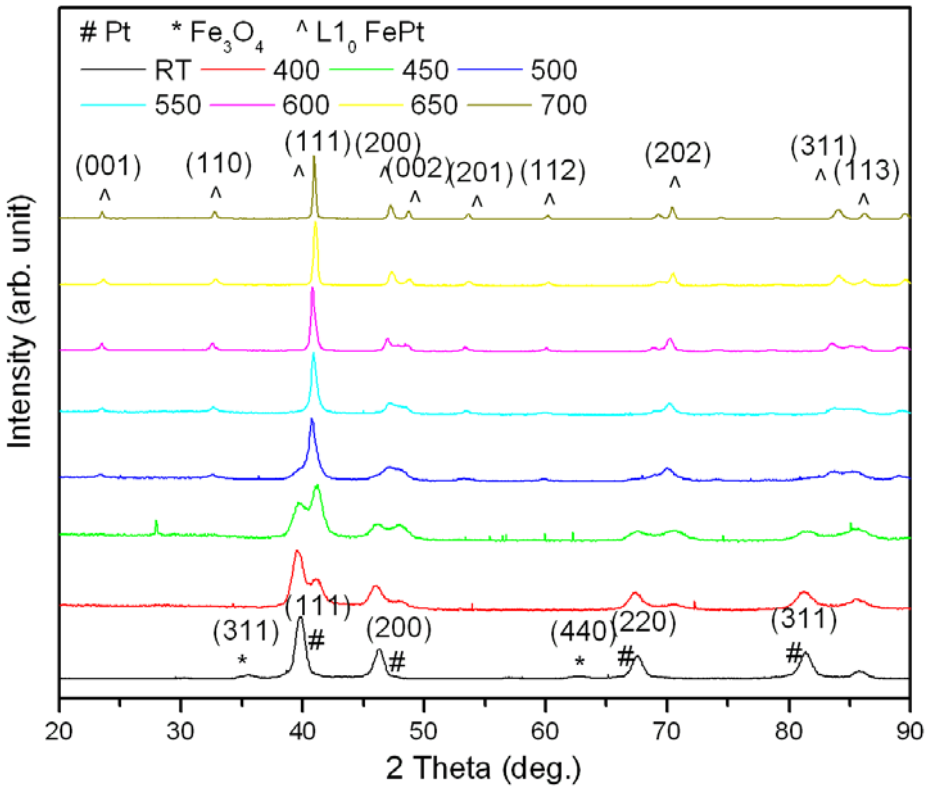

Figure 3.9 XRD of the 16 nm Pt/Fe_3O_4 core/shell nanoparticles before and after annealing at temperatures between 400 to 700 °C.

temperature, Fe precursor was injected which immediately decomposed and nucleated on surface of existing Pt nanoparticles and formed 3 nm Fe_3O_4 shell resulted in 16 nm Pt/Fe_3O_4 core/shell nanoparticle. Although various thicknesses of the Fe_3O_4 shell could be deposited on Pt cores which decided the final composition of the particle. These particles were later converted to FePt nanoparticles by conventional or salt matrix annealing in a reducing

atmosphere. Figure 3.9 shows XRD of the 16 nm Pt/Fe_3O_4 core/shell nanoparticles before and after conventional annealing at temperatures between 400 to 700 °C. It is clear from the Figure 3.9 that the iron oxide shell was reduced to iron and $L1_0$ FePt phase was formed. The formation was $L1_0$ phase was dependent of annealing temperature. We can see from the Figure 3.9 that as the annealing temperature was increased, fcc Pt and Fe_3O_4 peaks started disappearing and $L1_0$ FePt peaks started appearing. The complete ordered $L1_0$ FePt phase was obtained above 650 °C.

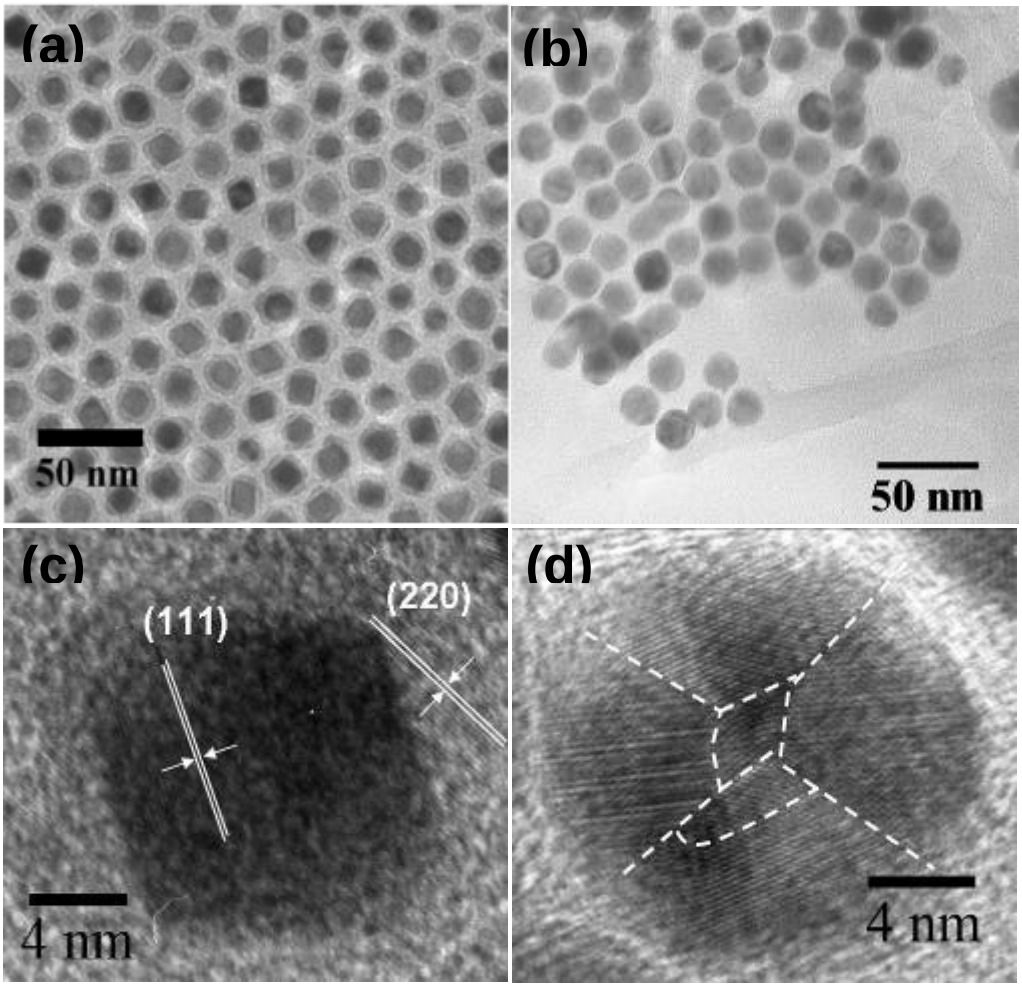

Figure 3.10 TEM of (a) as-synthesized 16 nm Pt/Fe_3O_4 core/shell nanoparticles (b) 16 nm $L1_0$ FePt nanoparticles. HRTEM of single (c) as-synthesized 16 nm Pt/Fe_3O_4 core/shell nanoparticle. (d) salt annealed polycrystalline 16 nm $L1_0$ FePt nanoparticle.

Figure 3.10(a) shows the TEM of as-synthesized 16 nm Pt/Fe_3O_4 core/shell nanoparticles. Figure 3.10(b) shows the image of a 16 nm FePt nanoparticle after salt annealing. Figure 3.10(c) and 3.10(d) shows the HRTEM image of 16 nm Pt/Fe_3O_4 nanoparticle and FePt nanoparticle respectively. We can see the FePt nanoparticle was polycrystalline because of the diffusion of Fe and Pt.

3.3.2 Shape Control of FePt Nanoparticles

3.3.2.1 Effect of Solvent

Solvents provide the media for particles to nucleate and grow. The correct composition of Fe and Pt is required to form the desired $L1_0$ phase. A solvent with high boiling point and chemical stability at higher temperature is required to achieve the correct composition of FePt by interatomic diffusion. Because of its stability at reflux temperature (295 °C), octyl ether is a most commonly used solvent for FePt nanoparticle synthesis. However, octyl ether is a very expensive solvent; therefore benzyl ether was used as an alternative solvent for most of the experiments. When benzyl ether was used as solvent, monodisperse spherical particles with narrow size distribution were obtained.

Nevertheless, while using benzyl ether it was very difficult to maintain the reflux temperature as it releases some low-boiling point byproducts at high temperature (above 270 °C) that results in the lowered temperature of the reaction mixture. Therefore, to maintain correct composition, octyl ether was used in our experiments. Interestingly, faceted cubic shape (Figure 3.11(b)) FePt nanoparticles instead of the spherical ones (Figure 3.11(a)) were obtained when octyl ether was used as the solvent. The change in shape of the nanoparticles could be related to the molecular structure of the solvents. Ether group molecules are attached in-between two benzene rings in benzyl ether whereas octyl ether has a linear structure with the ether group attached to both sides by hydrocarbon chain, which could have served as the matrix for the resultant shape. However, this shape change was only observed in particles larger than 7 nm but was hard to find in the smaller particles.

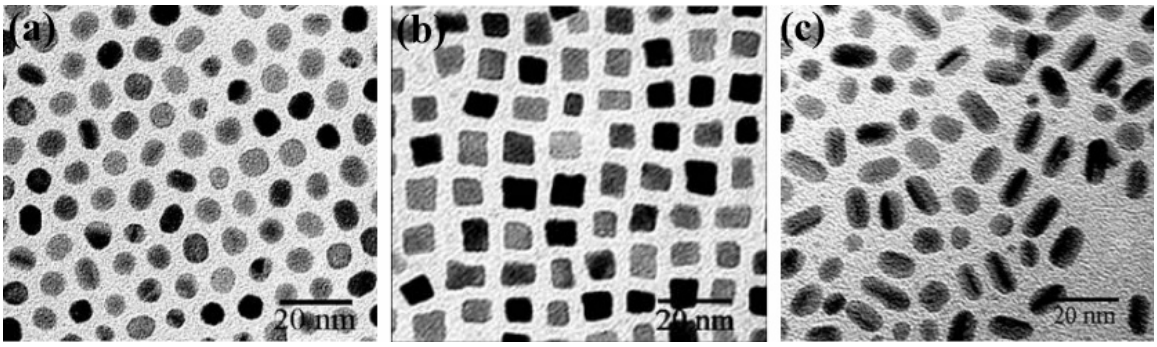

Figure 3.11 TEM image of (a) spherical, (b) cubic, and (c) rod-shape FePt nanoparticles.

3.3.2.2 Effect of Time Difference between Surfactants

The time interval of surfactant injection into the reaction mixture is another factor that influences the particle shape. In our synthesis procedure, both of the surfactants were injected simultaneously a few seconds after the injection of $Fe(CO)_5$. However, when using benzyl ether as a solvent, when oleyl amine was injected after 5 min of injection of oleic acid, rod shape nanoparticles (Figure 3.11(c)) with few spherical ones were obtained. The same result was not observed when octyl ether was used as the solvent. This is an interesting finding because rod shape nanoparticles are good candidates for anisotropic nanomagnets as they may be aligned by virtue of their shape.

3.3.3 Magnetic Properties of FePt Nanoparticles

The as-synthesized FePt nanoparticles have chemically disordered fcc structure with low-magnetic anisotropy which can be transformed into ordered $L1_0$ structure with very high magnetic anisotropy through thermal annealing above 500 °C.

3.3.3.1 Effect of Size

Room temperature and low temperature magnetic properties of the as-synthesized FePt nanoparticles were measured by SQUID. Figure 3.12 shows the hysteresis loops of as-synthesized FePt particles of 2, 4, and 8 nm. It has been found that all the nanoparticles are

superparamagnetic at 300 °K. This indicates that the thermal energy can overcome the anisotropy energy barrier of the individual particles, and the net magnetization of these nanoparticle assemblies is zero in the absence of an external field. However all the particles are ferromagnetic at 5 °K and magnetization is much higher compared to that at 300 °K (Figure 3.12). It is also observed that the saturation magnetization values of the particles are size dependent and increase with particle diameters.

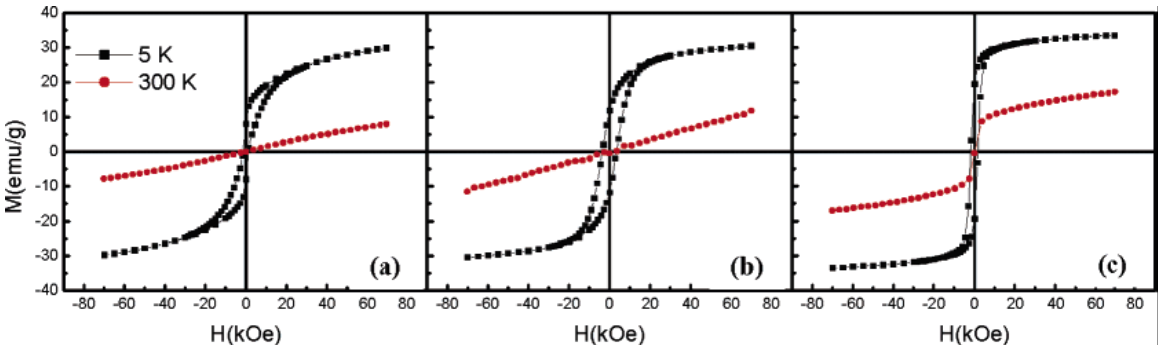

Figure 3.12 Hysteresis loops of the (a) 2 nm, (b) 4 nm, and (c) 8 nm FePt nanoparticle assemblies measured at 5 and 300 °K.

Since all different size as-synthesized particles were superparamagnetic at room temperature, their blocking temperature (T_B) was calculated by measuring the temperature dependence of magnetization with zero-field cooling (ZFC) and field cooling (FC) procedures, and found to be size dependent. On cooling, the ZFC magnetization begins to drop and deviate from FC magnetization at blocking temperature T_B. Figure 3.13 shows the plot of magnetization (M) versus temperature (T) for 2, 3, 4, 5, 6, 7, and 8 nm FePt nanoparticles with a measuring field of 100 Oe between 5 and 250 °K. The M versus T curves show peaks characteristic of superparamagnetic transitions. The peak temperature in the M versus T curve (blocking temperature) increases continuously with the increasing particle size (inset Figure 3.13); for example, the T_B values for 2, 5, and 8 nm particles are 15, 30, and 70 °K, respectively.

To obtain anistropic $L1_0$ phase, these fcc particles were deposited on a Si substrate and were annealed in forming gas (Ar + 7% H_2) at 650 °C for 1 h. After the annealing, all the particles gave a coercivity of more than 1 T. The very high coercivity indicates the phase transformation of these nanoparticles from disordered fcc to ordered $L1_0$ phase. The Hysteresis loop of annealed FePt nanoparticle assemblies show that their coercivity and magnetization depend strongly on initial FePt size. The coercivity trend seems to decrease with increase the size of FePt particles as shown in Figure 3.14(a). The highest coercivity achieved was complete 2.7 T in case of 2 nm particles (Figure 3.14(b)) while 9 nm particles gave coercivity of 1.3 T. However, magnetization was found to increase with increase in particle size.

.

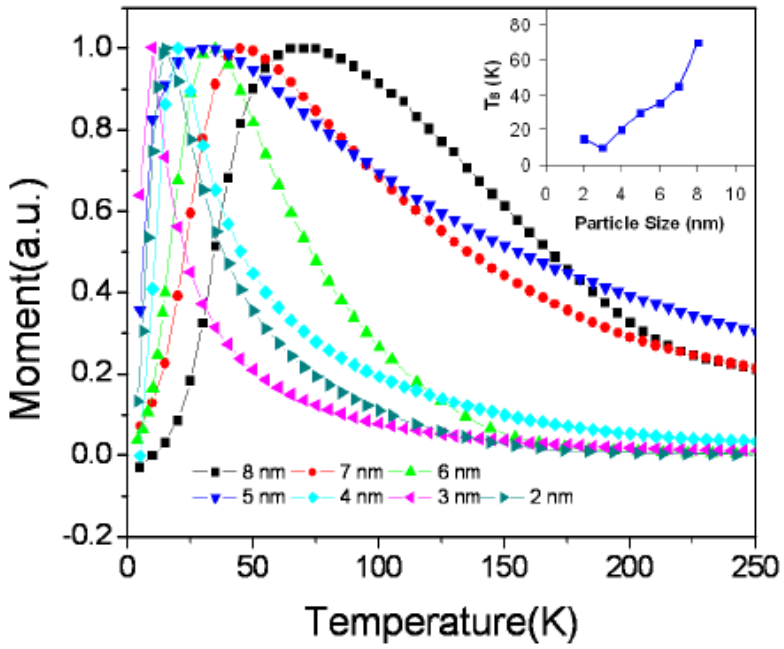

Figure 3.13. Magnetization versus temperature for 2 to 8 nm FePt nanoparticles measured at 100 Oe field.

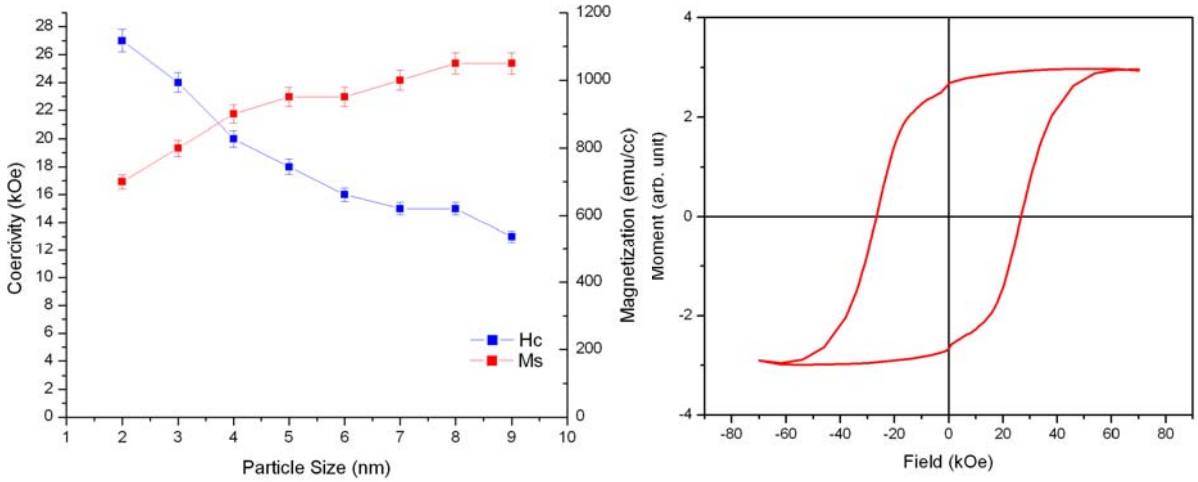

Figure 3.14 (a) Coercivity (Hc) and saturation magnetization (Ms) dependence on different size FePt nanoparticles after annealing at 650 °C for 1h (Left). (b) Hysteresis loop of 2 nm FePt particles giving the highest coercivity of 2.7 T after annealing at 650 °C for 1h (Right).

3.3.3.2 Effect of Shape

Magnetic properties of the magnetic nanoparticles can be greatly improved by magnetic alignment which means magnetization of the magnet lies only along the 'easy direction'. Shape controlled synthesis and self assembly can offer a simple solution to fabrication of magnetically aligned FePt nanoparticle arrays. As mentioned above, the particle's shape can be changed from spherical to cubic by changing reaction parameters.

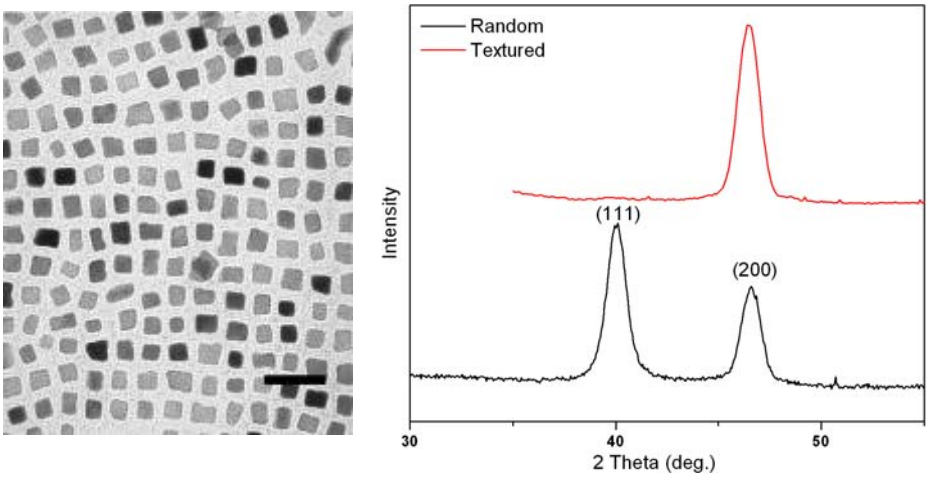

Figure 3.15 (a) TEM image of self assembly of as-synthesized 8 nm cubic FePt nanoparticles (Left, the scale bar in Figure 20 is 20 nm). (b) XRD of cubic particles after random and (100) textured assembly (Right).

Controlled evaporation of the carrier solvent from dispersion of these cubic nanoparticles led to a self-assembled two dimensional superlattice arrays as shown in Figure 3.15(a). XRD of this assembly in Figure 3.15(b) exhibits a strong (200) peak and absence of (111) peak. This is markedly different from that of a 3D randomly oriented FePt nanoparticle assembly with a strong (111) peak, indicating that each cubic nanoparticle in the assembly has a preferred crystal orientation with (100) planes parallel to substrate. However, as-synthesized particles are superparamagnetic; no difference was observed in hysteresis loop measured at room temperature. To obtain anisotropic phase, the assembly was annealed at 650 °C in forming gas, it also induced particle agglomeration which destroyed (100) texture in the assembly. As a result, there was no difference found in the parallel in perpendicular direction in the hysteresis loops of annealed assembly of nanoparticles. These results demonstrate that it is possible to use particle shape to control assembly texture and further magnetic alignment.

3.3.3.3 Effect of Composition

The 4 nm particles were chosen to observe the composition effect on magnetic properties since the composition control was found easy in 4 nm or smaller size particles compared to particles larger than 4 nm diameter. The Fe and Pt concentration in the nanoparticles can be tuned by adjusting the molar ratio (M) of Fe precursor ($Fe(CO)_5$) to

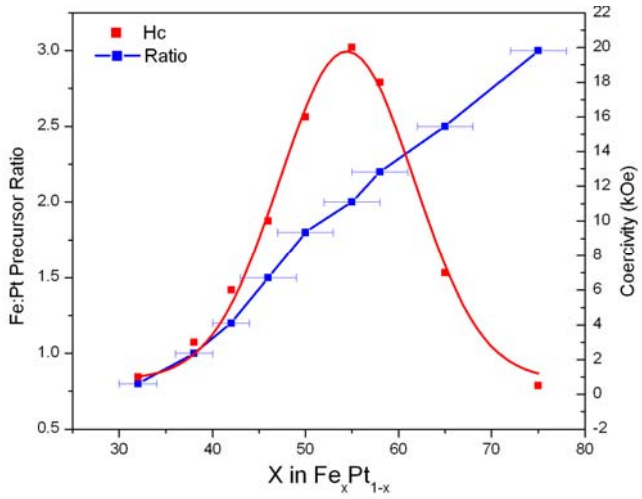

Figure 3.16 Composition dependence on coercivity (Hc) of annealed FePt nanoparticle assemblies.

Pt precursor ($Pt(acac)_2$), and the compositions ranging from $Fe_{30}Pt_{70}$ to $Fe_{75}Pt_{25}$ are obtained. On the basis of 0.5 mmol of $Pt(acac)_2$ and 0.5 mmol each of oleic acid and oleyl amine, the molar ratio between $Fe(CO)_5$ and $Pt(acac)_2$, and the resulting FePt particle compositions are shown in Figure 3.16. It was observed that the precursor molar ratio of 1:1 yielded $Fe_{38}Pt_{62}$ particles while the ratio 2:1 led to $Fe_{55}Pt_{45}$ nanoparticles. The Hysteresis loop of annealed FePt nanoparticle assemblies show that the coercivities of these annealed FePt particles depend strongly on FePt composition, also shown in Figure 3.16 and highest coercivity achieved was 20 kOe at $Fe_{55}Pt_{45}$.

3.3.3.4 Effect of Annealing Temperature

Magnetic properties of 4 nm $Fe_{55}Pt_{45}$ nanoparticles were observed after annealing them at different temperatures to observe the effect of annealing temperature. Shown in Figure 3.17(a) are Magnetization (Ms) and Coercivity (Hc) from the room temperature hysteresis loops for 4 nm FePt particles that were annealed from 500 to 700 °C with a difference of 50 °C. Both the Ms and

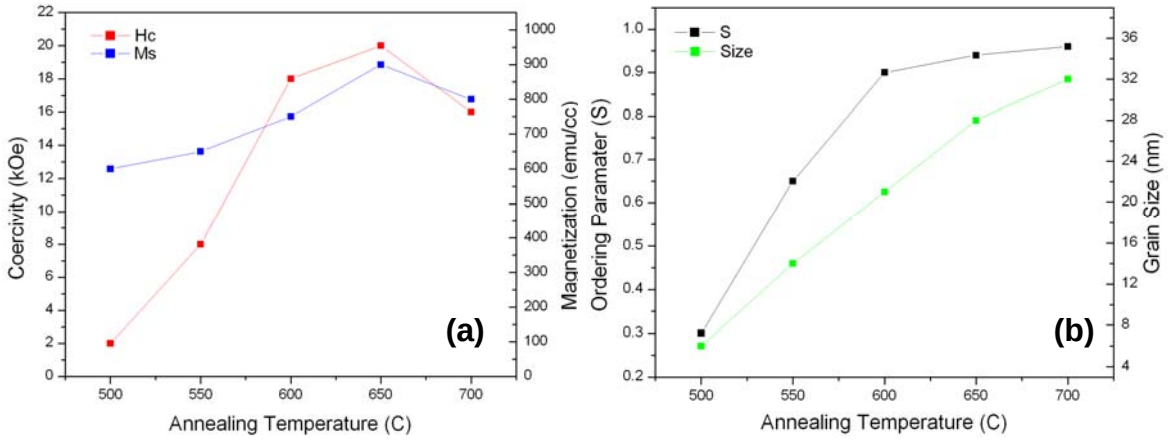

Figure 3.17 Annealing temperature dependence on (a) coercivity (Hc) and saturation magnetization (Ms) (b) Ordering parameter and final grain size for 4 nm FePt nanoparticles after annealing.

Hc values increase till 650 °C and then start decreasing. The sample annealed at 450 °C appears nearly superparamagnetic at room temperature. Increasing the annealing temperature from 500 to 650 °C increased the coercivity from 2 kOe to 18 kOe.

The reason of this increase is increment of ordered $L1_0$ phase which can be measured by ordering parameter (S) which can be calculated as

$$S = (I_{001}/ I_{002})^{0.85}$$

where I_{001} and I_{002} are intensities of peak (001) and (002), respectively. These peaks are characteristic peaks of $L1_0$ structure which start developing after annealing fcc FePt nanoparticles above 500 °C and increase with increasing annealing temperature as shown in Figure 3.18. However, the grain size of FePt nanoparticle also starts increasing with ordering parameter as the annealing temperature was increased as shown in Figure 3.17(b).

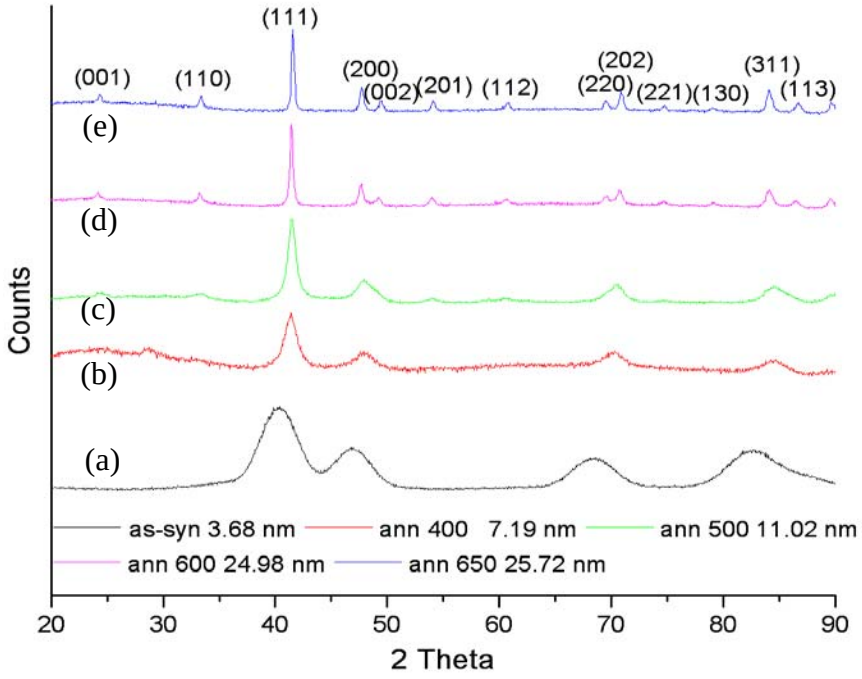

Figure 3.18 XRD and grain size of 4 nm FePt particles (a) as-synthesized and after annealing at (b) 400, (c) 500, (d) 600, and (e) 650 °C.

.

3.4 Conclusion

FePt nanoparticles of different size (2 to 16 nm) and shape (spherical, cubic, rod) with narrow size distribution have been prepared in a reproducible manner via chemical solution methods. The size and shape of these particles can be controlled in a systematic manner by tuning surfactants and their concentration, type of solvents, nature of precursors, and heating rate. The as-synthesized FePt nanoparticles were found to be superparamagnetic at room temperature and their blocking temperature was size dependent, which increased with particle size. After annealing in a reducing environment, thin film assemblies of these nanoparticles gave coercivity up to 2.7 T, which indicated their complete transformation from the disordered fcc to the ordered $L1_0$ structure. The Hysteresis loop of annealed FePt nanoparticle assemblies show that their coercivity and magnetization depend strongly on initial FePt size. The coercivity decreased while the magnetization increased with increase in the size of particles. Also, the coercivity of the FePt nanoparticles strongly depends on their composition and the highest coercivity was achieved at composition $Fe_{55}Pt_{45}$. The grain size and the ordering parameter of FePt nanoparticles were found to increase with increasing annealing temperature.

CHAPTER 4

SYNTHESIS AND CHARACTERIZATION OF BIMAGNETIC FePt/Fe_3O_4 NANOPARITCLES

4.1 Introduction

An important research direction in nanoparticle synthesis is the expansion from single-component nanoparticles to multicomponent hybrid nanostructures with discrete domains of different materials arranged in a controlled fashion. The advantages of multicomponent structures lie in three aspects. The first is to realize multifunctionality: different functionalities can be integrated, with the dimension and material parameters of the individual components independently optimized. One such example is the Co/CdSe bifunctional magneto-optic nanocrystals reported by Klimov's group.[84] The core/shell nanoparticles retain the magnetic and optical properties of each single component and permit potential applications as optical reporters and magnetic handles for bioassay. The second advantage is in providing novel functions not available in single-component materials or structures; for example, Jonker et al.[85] demonstrated a hybrid system that consisted of a ferromagnetic thin film on top of a semiconductor quantum-well structure that has been used to realize a new concept called a spin light-emitting diode (Spin-LED). The third advantage is in achieving enhanced properties and breaking the natural constraints of single-phase materials.[21,87] In 2002, Zeng *et. al.*[21] demonstrated that integration of a nanometer-scale magnetically hard phase with large coercivity and a nanometer-scale soft phase with high saturation magnetization with the two phases in intimate contact leads to a strong exchange coupling between the two phases and an enhanced energy product. The synthetic techniques to grow single component nanoparticles in the solution phase have been extended to multicomponent nanoparticles, where individual inorganic components are directly grown one on top of each other without linker molecules.

These composite particles consist of symmetric core/shell nanoparticles,[85,88-91] nonsymmetric heterodimers,[92-95] and other multi-component heterostructures.[96-98]

Exchange coupled hard/soft magnetic nanocomposites are future candidate of high energy permanent magnets. As mentioned in the last paragraph, Zeng *et. al.*[21] reported mixing of hard and soft magnetic nanoparticles that were synthesized separately to form nanoscale hard/soft nanoparticle assemblies. The mixing approach[21,99,100] requires precise control over the mass ratio and diameters of both the hard and soft magnetic nanoparticles, and the mixed nanoparticle assembly conditions have to be controlled carefully to achieve homogeneous distribution of different phases. Bimagnetic nanoparticles where each nanoparticle contains hard and soft ferromagnetic material are a better candidate for exchange coupled nanocomposite magnets since no blending process is necessary because each particle is a nanocomposite.[88,101,102] This method is more convenient in controlling dimensions of different components in order to achieve desired intimate interphase contact and morphology homogeneity. Exchange-coupled hard/soft bimagnetic nanoparticles are also proposed for future high density recording media over single hard phase nanoparticles since their coercivity is within the field limit imposed by writing head.[103]

This chapter reports synthesis and characterization of FePt/Fe_3O_4 bimagnetic nanoparticles by a one-pot sequential method. The soft magnetic Fe_3O_4 phase was grown on FePt nanoparticles directly, either coated or attached to FePt nanoparticles in a controlled manner resulting in two different morphologies; core/shell and heterodimers. Magnetic properties of each bimagnetic nanoparticle can be tuned by varying the dimension of the FePt as well as the Fe_3O_4. After being annealed in a reducing atmosphere, the FePt/Fe_3O_4 bimagnetic nanoparticles transformed to an exchange-coupled FePt/Fe_3Pt hard magnetic nanocomposite with enhanced energy products. Such bimagnetic nanoparticles represent a novel class of nanostructured magnetic materials that will allow precise engineering of magnetic properties by selectively tuning anisotropy, magnetization, and the dimensions of both hard and

soft magnetic material, and can further be used to fabricate devices for novel nanomagnetic applications.

4.2 Experimental

Bimagnetic FePt/Fe_3O_4 nanoparticles were synthesized by one step and two step method. In two step method, first as-synthesized FePt nanoparticles were synthesized and then later used as seeds and mixed with iron precursor, reducing agent and surfactants in a solvent. Fe_3O_4 coating was achieved by heating the mixture at elevated temperature. In one step method also first as-synthesized FePt nanoparticles were synthesized, then extra Fe precursor ($Fe(CO)_5$) was added in the same pot at intermediate temperature to form Fe_3O_4 on FePt nanoparticles.. The detailed procedures to prepare by one and two step synthesis of FePt/Fe_3O_4 nanoparticles have been given in the following paragraphs.

4.2.1 Two-step Synthesis of FePt/Fe_3O_4 Nanoparticles

In two step method, first FePt nanoparticles were synthesized as explained in section 3.2. Then, these as-synthesized FePt nanoparticles were used as seeds to prepare FePt/Fe_3O_4 bimagnetic nanoparticles by seed mediated approach. In a typical two step synthesis, $Fe(acac)_3$ (0.3 mmol), 1,2-hexadecanediol (1.5 mmol), oleic acid (0.3 mmol) and oleyl amine (0.3 mmol), and phenyl ether (10 mL) were mixed and magnetically stirred under a flow of argon. 50 mg of FePt nanoparticles in 5 mL hexane was also added. The mixture was heated at 100 °C for 20 min to remove hexane, and then at 200 °C for 1 h. Under a blanket of Ar gas, the mixture was heated to reflux (265 °C) for another 30 min. The black mixture was cooled to room temperature by removing the heat source. The product, FePt/Fe_3O_4 core/shell bimagnetic nanoparticles, was precipitated, centrifuged and re-dispersed under ambient condition as mention in the method explained in section 3.2. The Fe_3O_4 shell thickness on FePt nanoparticles were tuned by adjusting the mass ratio between FePt seeds and $Fe(acac)_3$. The mass of FePt seeds were kept same (50 mg), hence Fe_3O_4 was adjusted by changing amount of ($Fe(acac)_3$).

4.2.2 One-step Synthesis of FePt/Fe_3O_4 Nanoparticles

In a one step synthesis of bimagnetic FePt/ Fe_3O_4 nanoparticles, 0.5 mmol of platinum acetylacetonate was added to 125 mL flask containing a magnetic stir bar and mixed with 10 mL of octyl/benzyl ether. After purging with argon for 30 min at room temperature, the flask was heated up to 120 °C until the platinum precursor dissolved completely in the solvent. Then, 1.0 mmol of iron pentacarbonyl and a designated amount of oleic acid and oleyl amine were added at 120 °C. The flask was then heated to 230 °C for 1 h and then refluxed for 1 h before cooling down to 205 °C for further reaction. A designated amount of iron pentacarbonyl was injected into the flask at 205 °C and the temperature of the reaction mixture was raised to 290 °C for 30 min before cooling down to ambient temperature. The black product was precipitated by adding ethanol and separated by centrifugation and redispersed in hexane. By controlling the molar amount of Fe precursor in the second step, the dimension of Fe_3O_4 phase was readily tuned. The amount of Fe and Pt precursors in the first step was always kept constant. The morphology of these bimagnetic FePt/Fe_3O_4 nanoparticles was changed by merely changing the solvent in the reaction. When benzyl ether was used as the solvent, core/shell nanoparticles were obtained, while in the case of octyl ether, heterodimer nanoparticles were observed. Due to simplicity and the better morphological control of bimagnetic FePt/ Fe_3O_4 nanoparticles, this method was chosen over the two step synthesis for all the experiments.

4.2.3 Purification, Annealing and Characterization of FePt/Fe_3O_4 Nanoparticles

After being washed in ethanol three or more times, the bimagnetic nanoparticles were dispersed in hexane and stored in glass bottles under refrigeration. Samples for magnetic characterization were prepared by depositing a drop of the final hexane dispersion on a 3x3 mm^2 silicon substrate, evaporating the solvent at room temperature, and further drying in vacuum, which led to the formation of FePt/Fe_3O_4 nanoparticle-assembled thin films. The samples were then annealed at 650 °C for 1 h under the flow of forming gas (Ar+7%H_2) in a tube furnace. To prepare TEM samples, a drop of the nanoparticle dispersion solution in octane

was put on the formvar side of a 300-mesh carbon coated copper TEM grid. The solvent was allowed to evaporate slowly in air and the nanoparticles self assembled on the grid.

The transmission electron microscopy (TEM) images were recorded on a JEOL 1200 EX electron microscope at an accelerating voltage of 120 kV. HRTEM analysis was done at Georgia Institute of Technology and images were recorded on a HITACHI HF2000 electron microscope at an accelerating voltage of 200 kV. Powder X-ray diffraction (XRD) spectra were recorded on a Philips MPD diffractometer with a Cu KR X-ray source (*i*) 1.5405 Å). The magnetic hysteresis measurements have been carried out by using superconducting quantum interference device (SQUID) magnetometer with magnetic field up to 7 T. The composition analysis was done by energy dispersive X-ray spectroscopy (EDX) and inductively coupled plasma (ICP).

4.3 Results and Discussion

4.3.1 Morphology Control of FePt/Fe_3O_4 Nanoparticles

As mentioned earlier, when octyl ether was used as the solvent, heterodimer FePt/Fe_3O_4 nanoparticles were obtained while when benzyl ether was used, core/shell FePt/Fe_3O_4 nanoparticles were found. It is interesting to know the mechanisms of formation of the core/shell and heterodimer structured nanoparticles. Since FePt nanoparticles were already presented in the reaction mixture, Fe_3O_4 nucleated preferably on surface of the FePt seeds rather than nucleating separately to form independent Fe_3O_4 nanoparticles. As shown schematically in Figure 4.1, the final morphology depends on whether the FePt surface allows only a single nucleation site or multiple ones. As suggested by Yu *et al.*,[92] free electrons in the solution may also catalyze the Fe_3O_4 nucleation. Solvents which contain aromatic ring, such as benzyl ether, are good free electron donors. Their coordination to the FePt nanoparticles may replenish the electronic deficiency on the latter, consequently allow additional nuclei to form on the FePt surface, which can grow and eventually coalesce to form core/shell structures. In

contrast, solvents with largely saturated hydrocarbon chains such as octyl ether are not effective electron donors, and once a single Fe_3O_4 nucleus is present further nucleation may not be possible without electron donation from the solvent. Further growth of Fe_3O_4 from a single site then can lead to formation of a heterodimer nanoparticle.

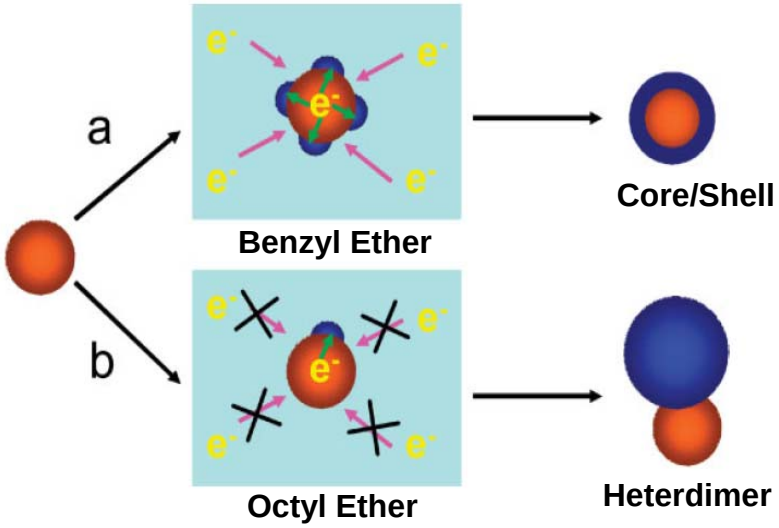

Figure 4.1 A schematic diagram showing the mechanism of formation of core/shell nanoparticles in benzyl ether (top) and heterodimers in octyl ether (bottom).

4.3.2 Size Control of FePt/Fe_3O_4 Nanoparticles

The size of the FePt in bimagnetic FePt/Fe_3O_4 nanoparticles was controlled from 4 to 8 nm by changing the surfactant to platinum precursor ratio during the synthesis of FePt nanoparticles. The dimension of Fe_3O_4, both in core/shell and heterodimers nanoparticles was tuned by controlling the molar amount of Fe precursor in the second step. In case of core/shell nanoparticles, Fe_3O_4 shell thickness was tuned from 1 to 3 nm while in case of heterodimers nanoparticles, the dimension of Fe_3O_4 was tuned from 3 to 10 nm. The main reason to control the size and morphology of FePt/Fe_3O_4 bimagnetic nanoparticles was to optimize the effective exchange coupling between FePt and Fe_3O_4 since the exchange coupling strongly depends on the dimensions and interaction of hard and soft phases.[12]

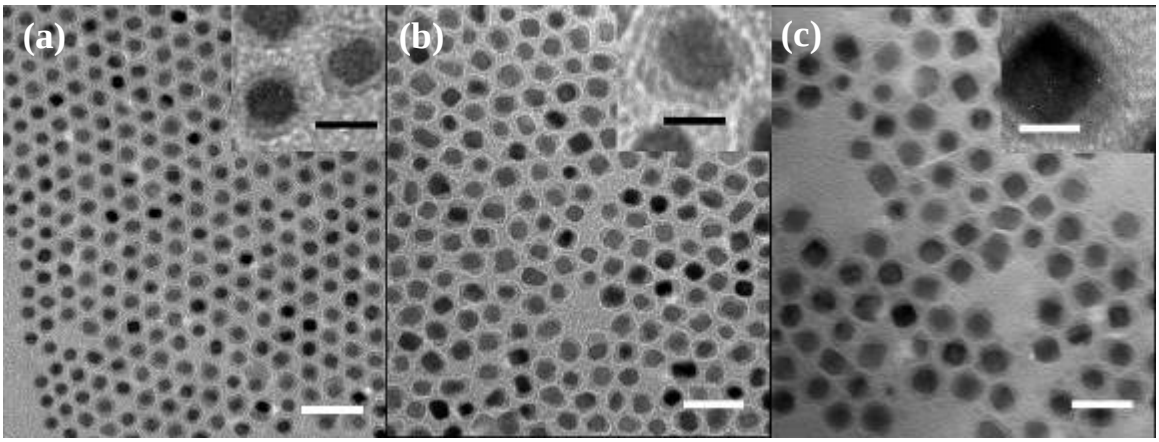

Figure 4.2 TEM of as-synthesized FePt/Fe_3O_4 core/shell nanoparticles with core diameter (a) 4 nm (b) 6 nm and (c) 8 nm (The scale bars in main image and inset image is 20 nm and 5 nm, respectively).

Figures 4.2 and 4.3 show TEM images of core/shell structured FePt/Fe_3O_4 nanoparticles with different core and shell dimensions. For each particle, the darker region is the FePt core and the lighter part is the Fe_3O_4 shell. The different contrasts between these two regions are due to the different electron penetration efficiencies of the metallic FePt and the oxide Fe_3O_4. The reaction conditions have to be well controlled in order to prevent any separate nucleation of Fe_3O_4 nanoparticles, especially when the shell thickness is increased. Figure 4.2 shows TEM images of core/shell structured FePt/ Fe_3O_4 nanoparticles with a systematic control in size of the FePt core between 4 and 8 nm. Figure 4.3 shows FePt/Fe_3O_4 core/shell nanoparticles with FePt core size 7 nm and Fe_3O_4 shell thickness from 0 to 3 nm. It is clear from Fig. 4.2 and 4.3 that the monodispersed FePt nanoparticles of different sizes are homogeneously coated with Fe_3O_4 shells with controllable shell thickness. Similarly, Figure 4.4 shows TEM images of bimagnetic FePt/Fe_3O_4 heterodimer nanoparticles with FePt size 8 nm and Fe_3O_4 size from 3 to 10 nm.

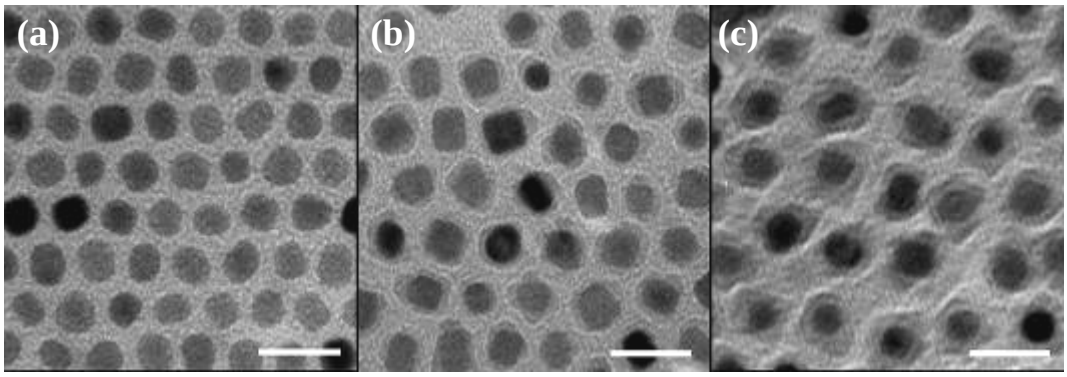

Figure 4.3 TEM of as-synthesized (a) 7 nm FePt nanoparticles coated with (b) 1 nm and (c) 2 nm Fe_3O_4 shell (The scale bar is 20 nm).

Figures 4.5(a)–4.5(f) show XRD patterns of the as-synthesized FePt/Fe_3O_4 core/shell nanoparticles with FePt core sizes of 4, 5, 6, 7, and 8 nm with 1 nm Fe_3O_4 shells. The patterns contain two sets of peaks, with one set matching with the disordered fcc FePt and the other with cubic spinel structured Fe_3O_4. It can also be seen that the width of (111) peak of FePt decreases as the FePt size increases. The size values of the FePt nanoparticles calculated using Scherrer's formula[47] are consistent with what are observed from the TEM images.

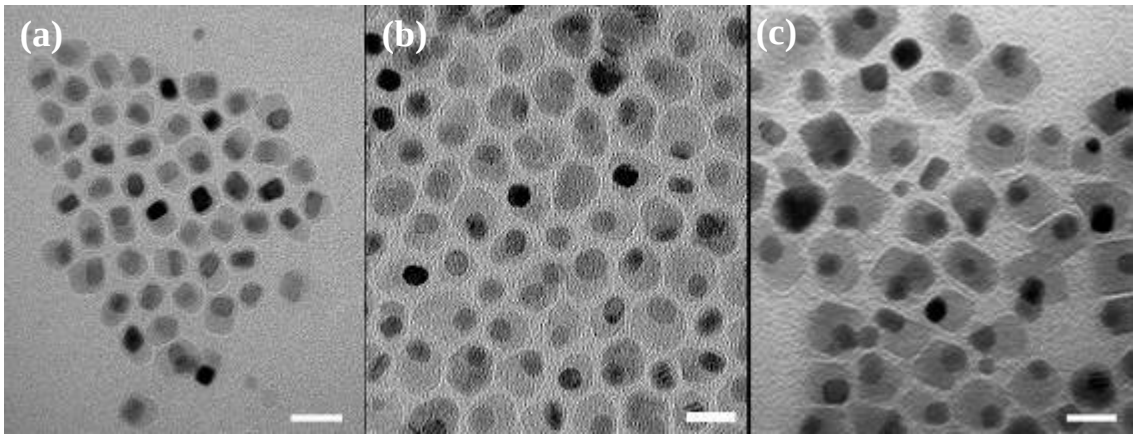

Figure 4.4 TEM of as-synthesized FePt/Fe_3O_4 heterodimer nanoparticles with 8 nm FePt core attached with (a) 3 nm, (b) 6 nm and (c) 8 nm Fe_3O_4 (The scale bar is 20 nm).

The HRTEM and electron diffraction pattern of the as-synthesized 8nm/2nm FePt/Fe_3O_4 core/shell and 8nm/8nm heterodimer nanoparticle reveals good crystallinity and clear lattice fringes, as shown in Figure 4.6 and 4.7, respectively. The lattice fringes in the HRTEM image correspond to a group of atomic planes within the particle, indicating that the particle is a single crystal. In HRTEM image of core/shell FePt/Fe_3O_4 nanoparticle (Figure 4.6(a)), only the lattice fringes of shell was clearly visible. The distance between two adjacent planes was measured 0.253 mn, corresponding to (311) planes in the spinel-structured Fe_3O_4 structure. The interfringe of core region of the FePt/Fe_3O_4 core/shell nanoparticle was difficult to index due to the overlapping of FePt core and Fe_3O_4 shell fringes since FePt nanoparticles are completely encapsulated by the Fe_3O_4 shell.

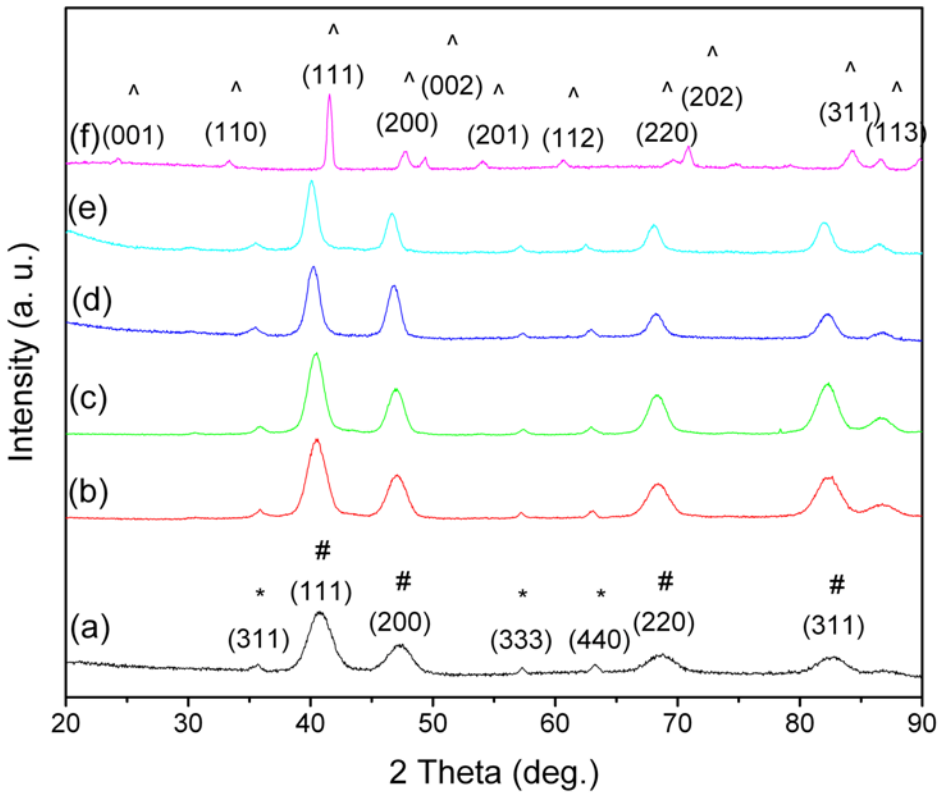

Figure 4.5 XRD of the as-synthesized FePt/Fe_3O_4 core/shell nanoparticles with FePt (#) core diameter (a) 4 nm, (b) 5 nm, (c) 6 nm, (d) 7 nm, (e) 8 nm with 1 nm Fe_3O_4 (*) shell thickness and (f) Fe_3Pt/FePt (^) nanocomposite after annealing of 8 nm FePt/1 nm Fe_3O_4 after annealing at 650 °C for 1 h.

However, in HRTEM image of the heterodimer FePt/Fe_3O_4 nanoparticle, the lattice fringes of FePt was clearly visible and their interfringe spacing was found 0.224 nm which corresponds interplanar distance of (111) planes in face centered cubic FePt. The interfringe spacing of Fe_3O_4 was 0.298 nm corresponding to (220) plane of spinel-structured Fe_3O_4 structure (Figure 4.6(b)).

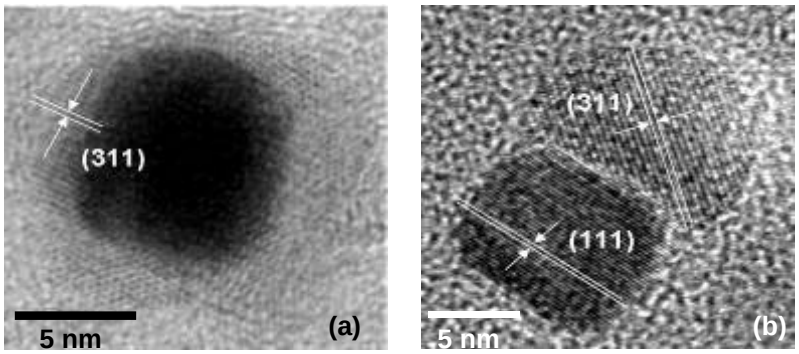

Figure 4.6 HRTEM of the as-synthesized (a) 8nm/2nm FePt/Fe_3O_4 core/shell and (b) 8nm/8nm heterodimer nanoparticle.

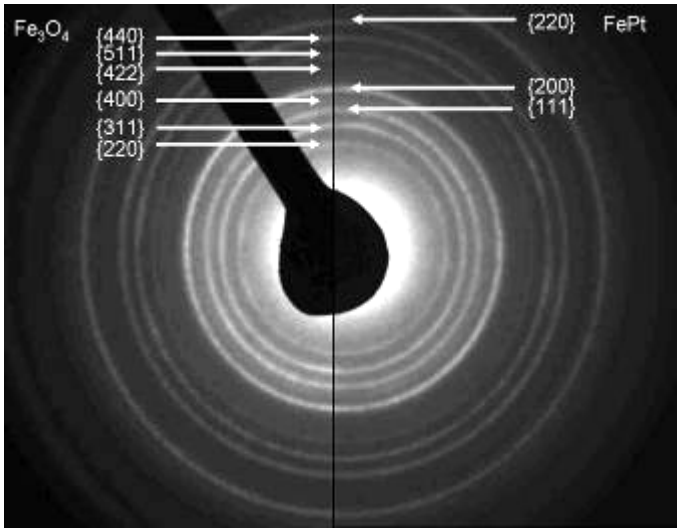

Figure 4.7 Electron diffraction pattern of the bimagnetic FePt/Fe_3O_4 core/shell nanoparticles showing fcc FePt and cubic spinel Fe_3O_4 patterns.

4.3.3 Magnetic Properties of FePt/Fe_3O_4 Nanoparticles

The as-synthesized FePt and FePt/Fe_3O_4 nanoparticles were found to be superparamagnetic at room temperature due to the low magnetocrystalline anisotropy of disordered fcc FePt. To obtain hard magnetic nanocomposite, the as-synthesized FePt/Fe_3O_4 nanoparticles were annealed in a reducing atmosphere (7% H_2+ 93% Ar) at 650 °C for 1 h. As shown in Figure 4.5(f), the XRD patterns confirmed the developed FePt/Fe_3Pt nanocomposite magnets being annealed at 650 °C. The appearance of FePt $L1_0$ peaks in XRD patterns showed the transformation of FePt phase from disordered fcc FePt structure to the magnetically hard $L1_0$ structure. The Fe_3O_4 was transformed into Fe_3Pt magnetic soft phase during the reductive annealing. The similar works have been reported for the FePt/Fe_3O_4 mixtured[104] and bricklike[105] nanoparticles systems. During the first step of the reaction, the composition of Fe/Pt in FePt nanoparticles was kept $Fe_{52}Pt_{48}$ in all experiments since it is an optimized composition to obtain highest coercivity from FePt nanoparticles.[88] The ratio of Fe/Pt in core/shell and heterodimers FePt/Fe_3O_4 nanoparticles was higher than that of FePt nanoparticles due to the presence of Fe_3O_4 phase. For example, for 8 nm/1 nm and 8 nm/3 nm as-synthesized FePt/Fe_3O_4 core/shell nanoparticles, the composition of Fe/Pt was found 61/39 and 74/26, respectively. As a comparison, annealing an assembly containing iron-rich $Fe_{65-70}Pt_{30-35}$ alloy nanoparticles led to materials that are magnetically much softer (H_c less than 1 kOe). This suggests that the hard magnetic property of the annealed hard/soft nanoparticle assembly originates from exchange-coupled hard and soft phases, not from the homogeneous iron-rich FePt alloy.

4.3.3.1 Coercivity and Magnetization

As mentioned above, after being annealed in a reducing atmosphere, the FePt/Fe_3O_4 bimagnetic nanoparticles transformed into a FePt/Fe_3Pt hard magnetic nanocomposite. As dimension of Fe_3O_4 in bimagnetic FePt/Fe_3O_4 nanoparticles was increased systematically, the magnetization of the nanocomposite was found to increase while the coercivity decreased as

shown in Figure 4.8 and 4.9. The increase in magnetization is attributed to the formation of high-magnetization Fe_3Pt soft phase during the annealing under the reducing atmosphere. However, the low magnetocrystalline anisotropy of the Fe_3Pt phase leads to a decrease in coercivity of the nanocomposite magnets. The dependence of saturated magnetization and coercivity on the soft-phase fraction is quite similar to the numerical simulations, which were reported for the isotropic nanocomposite magnets.[106,107] Prior to Fe_3O_4 coating/attachment, there was variation in saturation magnetization (Ms) and coercivity (Hc) in the different size FePt nanoparticles due to the slight difference in the average composition of particles. The 8 nm FePt particles had lowest coercivity but highest magnetization and vice versa for 4 nm FePt particles. However, this difference started diminishing as Fe_3O_4 was coated/attached on FePt nanoparticles. The reason of was the proportion of Fe_3O_4 in FePt/Fe_3O_4 nanoparticles. For FePt/Fe_3O_4 nanoparitcles with different size FePt and similar Fe_3O_4 shell thickness, the proportion of Fe_3O_4 was higher in particles with smaller FePt which resulted in higher increase in magnetization and decrease in coercivity. Hence, though 4 nm FePt particles' magnetization

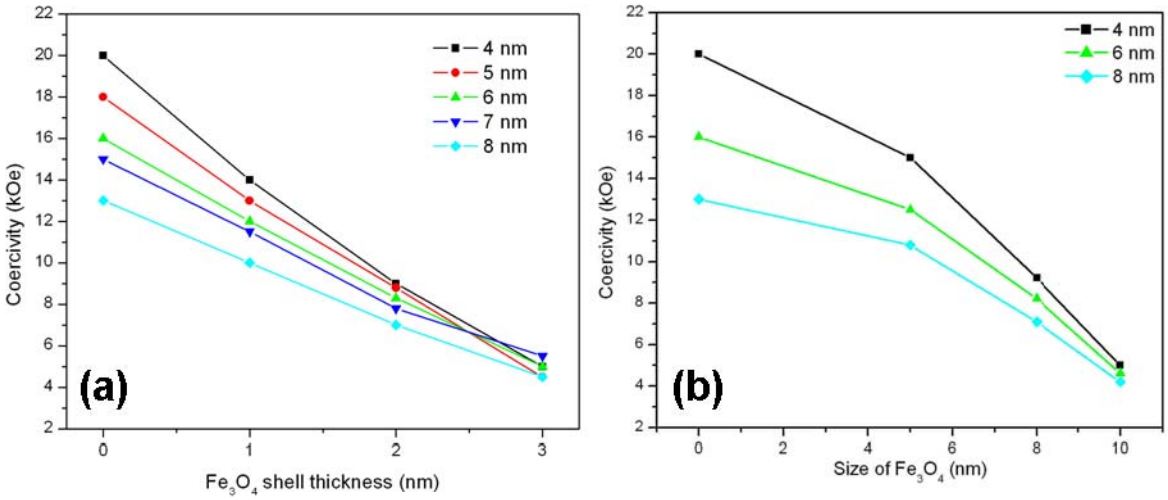

Figure 4.8 Variation in coercivity of the annealed FePt/Fe_3O_4 (a) core/shell nanoparticles of different FePt core sizes (4–8 nm) and Fe_3O_4 shell thickness (0–3 nm) and (b) heterodimer nanoparticles of different sizes FePt (4–8 nm) and Fe_3O_4 (0–10 nm).

was lower than 8 nm FePt, after coating 1 nm Fe_3O_4 shell on both, the increase in magnetization and decrease in coercivity was higher in 4 nm FePt which decreased the difference between them. If the shell thickness was increased to 2 nm, the different further decreased and so on.

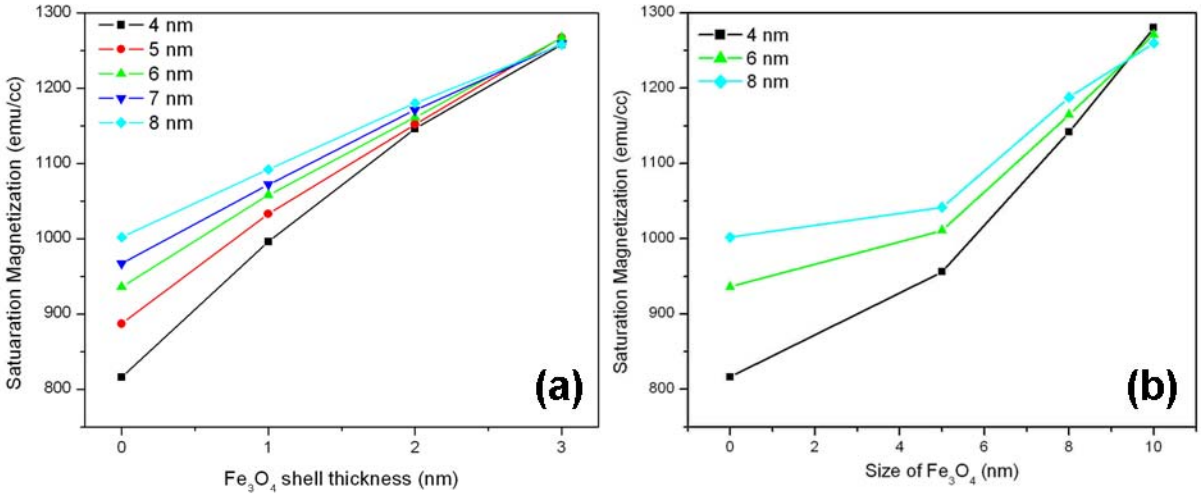

Figure 4.9 Variation in saturation magnetization of the annealed FePt/Fe_3O_4 (a) core/shell nanoparticles of different FePt core sizes (4–8 nm) and Fe_3O_4 shell thickness (0–3 nm) and (b) heterodimer nanoparticles of different sizes FePt (4–8 nm) and Fe_3O_4 (0–10 nm).

4.3.3.2 Energy Product

The energy product ($(BH)_{max}$) dependence on the soft phase dimension of the core/shell and heterodimers FePt/Fe_3O_4 nanoparticles with different sizes is given in Fig. 4.10. It is found that unlike coercivity and saturation magnetization, the relation between $(BH)_{max}$ and Fe_3O_4 dimension is not monotonous. In the case of core/shell particles, the $(BH)_{max}$ was increased initially with increasing Fe_3O_4 shell thickness and decreased after certain Fe_3O_4 shell thickness. As mentioned in 1.3.7, for the nanocomposite with sufficiently high H_c values ($H_c > 2\pi M_s$), the maximum energy product is limited by equation 1.6 $(BH)_{max} \leq (2\pi M_s)^2$. It is clear from results in

previous section that increasing the soft phase dimension results in a trade off between the magnetization and coercivity. Hence, in our case the magnetization was increased the expense of coercivity by increasing the Fe_3O_4 shell thickness and the energy product was increased (up to 2 nm Fe_3O_4 shell thickness). However, if the coercivity falls below the sufficiently high values as in case of 3 nm Fe_3O_4 shell thickness, then the energy product starts again decreasing. Our optimized conditions show that the highest energy product 17.8 MGOe was obtained in 8 nm/2 nm FePt/Fe_3O_4 core/shell nanoparticles after being annealed at 650 °C for 1h. This value is 36% higher than the theoretical value of 13 MGOe for the nonexchange-coupled isotropic FePt single-phase material. Unlike core/shell particles, the $(BH)_{max}$ from the heterodimers nanoparticles was not improved after being attached with Fe_3O_4. Instead of improvement, the $(BH)_{max}$ was found even lower than FePt nanoparticles of all different sizes (Fig. 4.10(b)). This is because energy products are not only dependent on the magnetization and coercivity but also on the hysteresis loop squareness which has been discussed in the next paragraph.

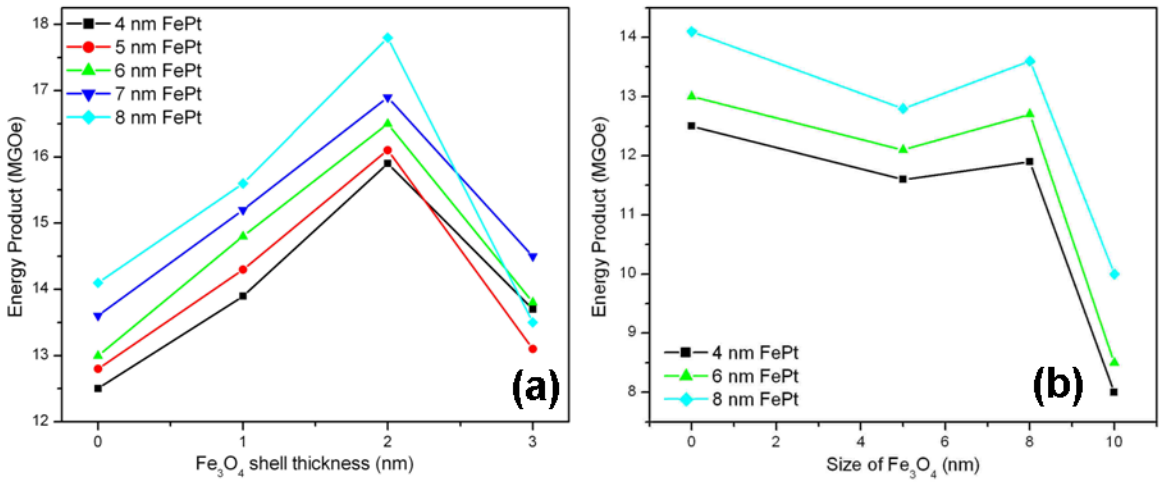

Figure 4.10 Variation in maximum energy product of the annealed FePt/Fe_3O_4 (a) core/shell nanoparticles of different FePt core sizes (4–8 nm) and Fe_3O_4 shell thickness (0–3 nm) and (b) heterodimer nanoparticles of different sizes FePt (6–8 nm) and Fe_3O_4 (0–10 nm).

Figures 4.11(a) and 4.11(b) show the hysteresis loops of annealed core/shell and heterodimer FePt/Fe_3O_4 nanoparticles, respectively. The dimension of FePt core was kept same of 8 nm as an example. The hysteresis loop of the annealed single-phase FePt nanoparticles is also included in the Figure 4.11 for comparison purpose. It can be seen that the single-phase FePt nanoparticles have the highest coercivity but the lowest magnetization. All the hysteresis loops of core/shell particles were found smooth (Figure 4.11(a)) however, one can see kinks in the hysteresis loops for the heterodimer nanoparticles (Figure 4.11(b)), indicating less effective exchange coupling between the hard and the soft phases. It was the main reason of lesser energy product of heterodimers nanoparticles than core/shell nanoparticles.

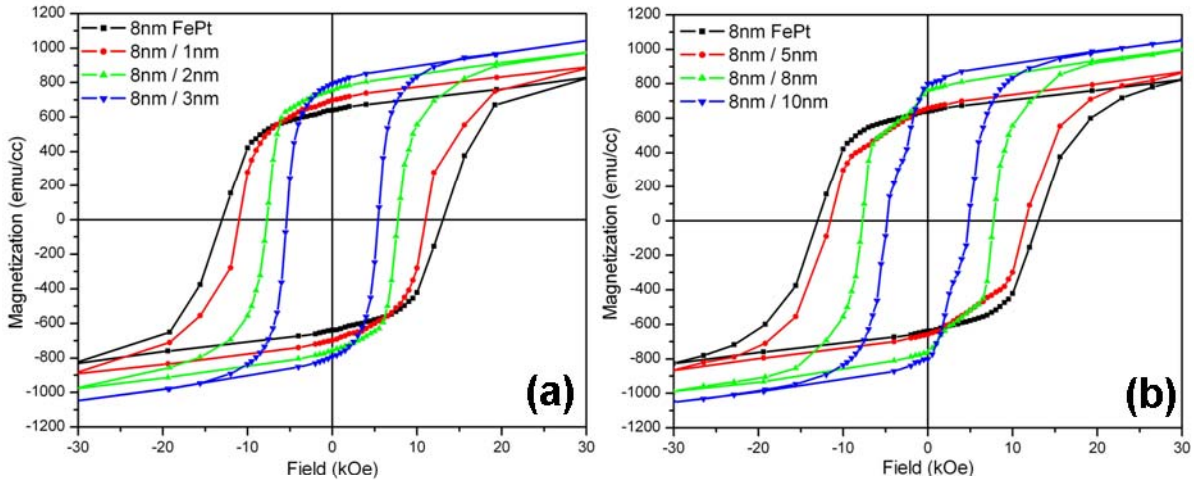

Figure 4.11 Room-temperature hysteresis loops of annealed FePt/Fe_3O4 (a) core/shell nanoparticles with 8 nm FePt core and Fe_3O_4 shell thickness increasing from 1 to 3 nm. (b) Heterodimer nanoparticles with 8 nm FePt and Fe_3O_4 from 5 to 10 nm at 650 °C for 1 h.

4.3.3.3 Delta M Curves

To further understand the difference in exchange coupling strength caused by the morphology, Henkel plots (δ*m* plots, also called as delta M plots) of the annealed core/shell and heterodimer nanoparticles with similar composition were measured. The soft-phase fraction in the core/shell particles with 2 nm shells was about the same as in the heterodimers particles

with 8 nm Fe_3O_4 attachments, both were around 50% volume. The δ*m* values can be measured by $\delta m = m_d(H) - [1 - 2m_r(H)]$, where m_d is normalized demagnetization remanence and m_r is the normalized isothermal magnetization remanence.[108,109] Figure 4.12 shows the δ*m* curves of the 8 nm/2 nm core/shell and 8 nm/8 nm heterodimer FePt/Fe_3O_4 nanoparticles after annealing at 650 °C for 1 h. It is clearly seen that the positive δ*m* values were obtained in both the core/shell and heterodimer nanoparticles, indicating the exchange coupling between the hard and soft phases. Moreover, the δ*m* value of the annealed core/shell nanoparticles is substantially higher than that of the annealed heterodimer nanoparticles. This confirmed that the exchange coupling in the core/shell nanoparticles is stronger than that in the heterodimer nanoparticles. More interestingly, the curve for the heterodimers sample shows more negative portion, which is a measure for dipolar interaction. We observed that the negative portion is enhanced when large amount of soft phase is added to nanocomposite magnets. However, as we indicated that the soft phase fraction in these two samples is the same. This difference may be explained by a less homogeneous distribution of the soft phase in the nanocomposite magnets made from heterostructured nanoparticles.

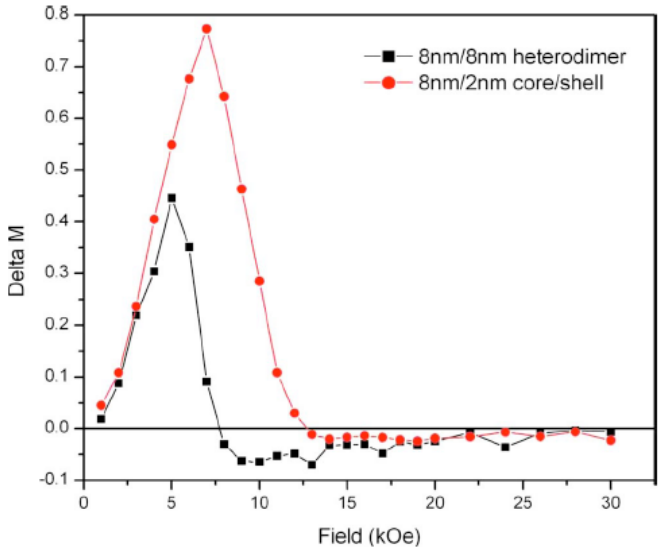

Figure 4.12 Delta M curves of 8 nm/2 nm core/shell and 8 nm/8 nm heterodimer FePt/Fe_3O_4 nanoparticles after annealing at 650 °C for 1 h.

4.4 Conclusion

$FePt/Fe_3O_4$ bimagnetic nanoparticles of two different morphologies; core/shell and heterodimer have been prepared in a one and two step synthesis by reduction in platinum acetylacetonate and thermal decomposition of iron pentacarbonyl. The morphology of the nanoparticles was controlled by changing solvent in the reaction. The size of FePt and Fe_3O_4 was tuned by changing different reaction parameters. The size of FePt was tuned from 4 to 8 nm and the size of Fe_3O_4 was tuned from 1 to 3 nm in core/shell and 5 to 10 nm in heterodimers. After being annealed in a reducing atmosphere, the $FePt/Fe_3O_4$ nanoparticles form a hard magnetic nanocomposite with enhanced magnetic properties, which are closely related to dimensions of the soft and hard phase components and their morphology. The heterodimer nanoparticles resulted in relatively poor magnetic properties compared to the core/shell nanoparticles due to insufficient exchange coupling. By optimizing the dimensions of the FePt and Fe_3O_4 in core/shell bimagnetic nanoparticles, energy product up to 17.8 MGOe has been achieved, which is 36% higher than the theoretical value for isotropic single-phase FePt. These bimagnetic nanoparticles can be excellent building blocks for high performance nanocomposite magnets and high density recording media.

CHAPTER 5

WARM COMPACTION OF $FePt/Fe_3O_4$ NANOPARTICLES

5.1 Introduction

Exchange-coupled hard/soft nanocomposite magnets have attracted great interest[110-113] in the last decade because of their potential in achieving giant energy product $(BH)_{max}$ that may be as large as 100 MG Oe.[7,107] The magnetic behavior of these exchange-coupled nanocomposite is closely related to grain size and nanostructured morphology. Effective interphase exchange coupling can be obtained only if dimensions of the soft-phase component in a nanocomposite magnet are not larger than a twice the domain wall thickness of hard phase component. [12,114–118] This critical thickness is typically in the range of several nanometers. The grain size in nanocomposite magnets fabricated by conventional top down methods, including mechanical alloying and rapid quenching, usually has a wide distribution, and can hardly be controlled below the critical length. An alternative bottom-up approach therefore is necessary to fabricate nanocomposite magnets with controllable nanoscale morphology.

FePt nanoparticles synthesized by chemical solution methods have aroused significant attention because of their very small particle size and size distribution, which make them ideal building blocks for exchange-coupled nanocomposite bulk magnets.[21,71,119,120] The biggest challenge for the bottom-up approach is how to produce bulk nanostructured magnets without losing the homogenous nanoscale morphology. Conventional compaction and condensation techniques cannot be applied to nanoparticles since those techniques require extensive heat treatments which lead to excessive grain growth which can destroy the nanoscale morphology. To date, there have been very limited data reported on direct compaction of intermetallic nanoparticles, especially for nanoparticles with size down to several nanometers. Recent attempts to fabricate bulk nanostructured magnets by using unconventional compaction

techniques including plasma sintering and dynamic compaction have resulted limited success.[121-123] Bulk samples with density up to 80% theoretical value have been obtained. The challenge remains in producing bulk nanostructured magnets with density close to theoretical values.

High-pressure warm compaction is one of the advanced compaction techniques in powder metallurgy and has been widely used in automobile parts manufacturing in the past decade.[124–127] This technique is established on the knowledge that metallic powders have better plasticity and compressibility at elevated temperatures and therefore are easier to be deformed to form high density bulks under a certain pressure, compared with cold pressing. Unlike hot pressing, warm compaction is performed at modest temperatures at which the metallic powders are chemically stable and no excessive grain growth occurs.

In this chapter, preparation and characterization of bulk FePt/Fe_3Pt nanocomposite magnets have been reported. The chemically synthesized core/shell FePt/Fe_3O_4 nanoparticles and FePt+Fe_3O_4 mixed nanoparticles were compacted at 400 °C, 500 °C and 600 °C to compare the magnetic and structural properties. Later the FePt/Fe_3O_4 compacted samples were post annealed at 650 °C in forming gas (93% Ar + 7% H_2) for 1h. Fe_3O_4 was reduced and the samples were converted into $L1_0$ FePt/Fe_3Pt magnetic nanocomposite. The high coercivity of $L1_0$ FePt and high magnetization of Fe_3Pt resulted in high energy product of the FePt/Fe_3Pt nanocomposite magnets. The density of the compacted sampled was as high as 85% of theoretical values. By doing micro structural (XRD, TEM) characterization, it was found that the nanoscale morphology can be retained after compaction and even after post-annealing for both core/shell and mixed nanoparticles bulk samples. From magnetic characterization, it was found that the bulk samples compacted of core/shell nanoparticles have more effetive better exchange coupling and therefore higher energy product than compacted samples of mixed nanoparticles.

5.2 Experimental

5.2.1 Synthesis of Core/Shell and Mixed FePt/Fe_3O_4 Nanoparticles

8 nm/2 nm FePt/Fe_3O_4 bimagnetic core/shell nanoparticles were chosen for compaction, since they give the highest energy product in nanoparticles assembled thin films as discussed in Chapter 4. To prepare mixture of FePt and Fe_3O_4 nanoparticles, 8 nm FePt and 4 nm Fe_3O_4 nanoparticles were mixed in such a ratio (6:1) that their ratio of Fe and Pt were same as in 8 nm/2 nm FePt/Fe_3O_4 core/shell nanoparticles. The FePt and bimagnetic core/shell FePt/Fe_3O_4 nanoparticles were synthesized by standard airless chemical solution procedures as mentioned in chapter 3 and 4. The 8 nm FePt nanoparticles used in FePt/Fe_3O_4 mixture were synthesized with procedure given in Chapter 3 and were exactly similar in composition and magnetic properties to the 8 nm FePt particles used as seeds for FePt/Fe_3O_4 core/shell nanoparticles synthesis. To prepare 4 nm Fe_3O_4 nanoparticles, $Fe(acac)_3$ (2 mmol) was mixed in phenyl ether (20 mL) with 1,2-hexadecanediol (10 mmol), oleic acid (6 mmol), and oleylamine (6 mmol) under nitrogen and was heated to reflux for 30 min. After cooling to room temperature, the dark-brown mixture was treated with ethanol under air, and a dark-brown material was precipitated from the solution. The product was dissolved in hexane in the presence of oleic acid and oleylamine and reprecipitated with ethanol to give 5-nm Fe_3O_4 nanoparticles. The FePt/Fe_3O_4 nanoparticles (core/shell and mixture) were centrifuged 3 times with ethanol and finally dried in vacuum for 24 hours.

5.2.2 Warm Compaction of FePt/Fe_3O_4 Nanoparticles

The dried nanoparticles were heated under Ar atmosphere at 350 °C for 1 h to remove surfactants. Then 1.0g of these start powders were then compacted with a warm-compaction Rockland press under pressure of 2.0 GPa for 15 min at temperatures ranging from 400 °C to 600 °C. The obtained bulk samples had dimensions 7.5 mm diameter and 2.5 mm thickness. The Archimedes method was employed for measurements of bulk sample density. The detailed procedure of compaction experiment is as follows:

First the sample assembly placed in pressure vessel. Then the ram spacer, piston, pressure vessel and pressure plates were placed on the press in the same order (Figure 5.1). The sample assembly was prepared as shown in the Figure 5.2. The thermocouple assembly was inserted through the hole in the top plate. Water was used as coolant in the press. The pressure plates and pressure vessel were coated with grease to avoid the corrosion by water. The initial pressure from top was applied up to 4000 psi. Then the water supply was connected. Then the top pressure was increased till 7000 psi and kept it constant. Then the bottom pressure was applied until 3000 psi. The temperature controller was switched on and the heating was started.

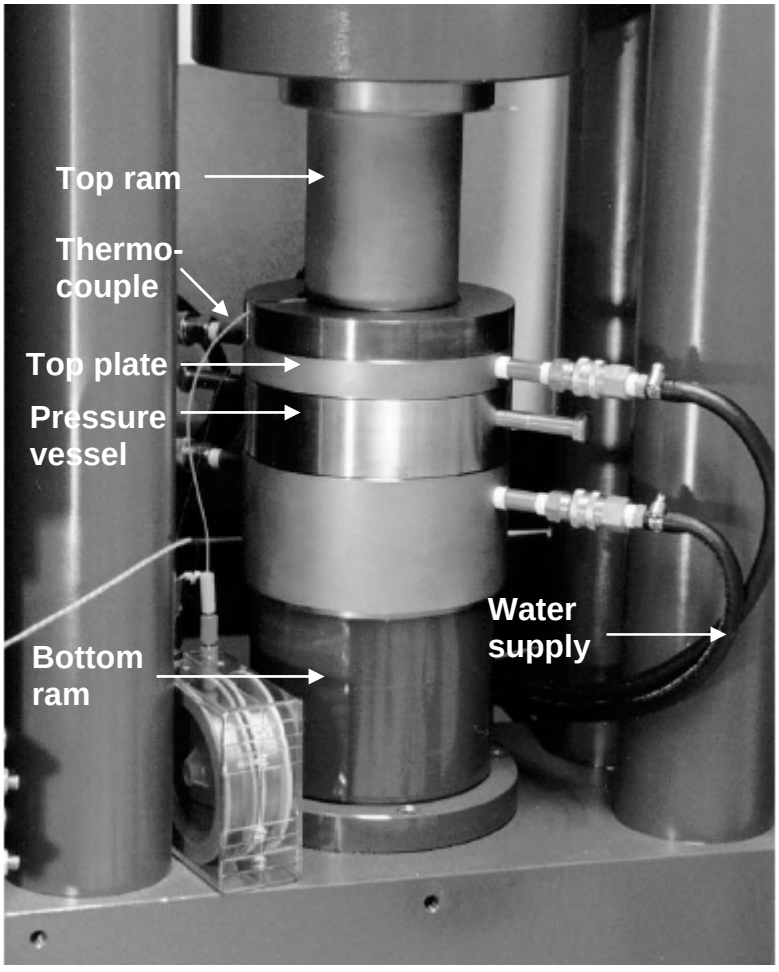

Figure 5.1 Photograph of Rockland press with assembled parts.

Heating was achieved by passing an electrical current through a graphite furnace placed inside sample assembly. Temperature was controlled by a Eurotherm temperature controller and silicon controlled rectifier supplied by Rockland Research. The heating was controlled manually though the heating rate was kept 100 ºC per minute. As the final compaction temperature was reached, the bottom pressure was increased further till 6300 psi (calibrated for 2 GPa in press) and kept for 15 minutes. After that, the temperature was decreased to room temperature and then the bottom pressure was completely released slowly. Then the water supply was removed and in the end the top pressure was released. Finally, the compacted sample was taken out from the pressure vessel.

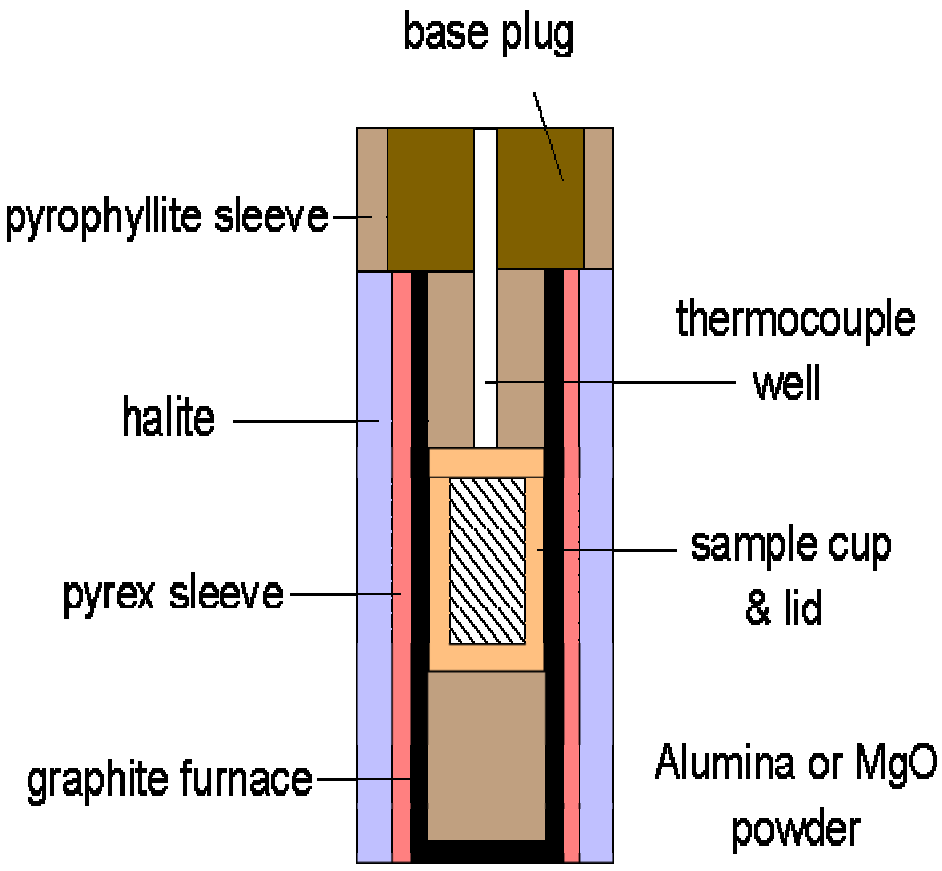

Figure 5.2 Schematic of internal parts of warm compaction sample assembly.

5.2.3 Annealing and Characterization of Compacted FePt/Fe_3O_4 Nanoparticles

The density of the compacted sampled was measured using Archimedes method. Then a part of compacted samples were then annealed at 650 °C for 1 h under the flow of forming gas (Ar+7%H_2) in a tube furnace. Both the unannealed and annealed compacted sample were then used for magnetic and structural analysis. The morphology and crystalline structure were characterized by scanning electron microscopy (SEM), transmission electron microscopy (TEM), and x-ray diffraction (XRD). The composition of the compacted samples were checked by energy dispersive x-ray (EDX) analysis in SEM. Magnetic properties were measured with superconducting quantum interference device (SQUID) magnetometer with a maximum applied field of 70 kOe. The TEM images were recorded on a JEOL 1200 EX electron microscope at an accelerating voltage of 120 kV. Powder X-ray diffraction (XRD) spectra were recorded on a Philips MPD diffractometer with a Cu Kα X-ray source (*i*) 1.5405 Å).

TEM samples of as-compacted samples were prepared using the conventional bulk TEM sample preparation technique. A disc of less than 3 mm diameter and 1 mm thickness was cut from an as-compacted sample. Then pyrex (sample holder) with a small piece of low melting wax was placed on hot plate which was set at 150 °C. When the wax melted, the disc was placed onto pyrex where the wax was located. Then pyrex was removed from hot plate and disc was mounted on the pyrex when the wax was cured. The pyrex was placed in a disc grinder to carry out mechanical polishing on sand papers or diamond paper with different grit size. The sample was polished until a mirror-finished surface was obtained. Then the disc was removed from the pyrex by melting the wax on the hot place and cleaned in the acetone to remove the remaining wax. Then the polished side of disc was mounted down onto the pyrex using low melting wax and the other side of the disc was mechanically polished on 600 grit sand paper to reduce the thickness of the sample to ~100 μm. Then the pyrex was placed on precision dimple grinder and sample was polished using Cu wheel and fine diamond paste until it is thinned to a thickness of ~15 μm. Then the sample was polished using felt polishing ring and alumina

polishing suspension to get a mirror finished surface. Then the sample was removed from pyrex and placed into ion-mill (PIPS, 4.5 kV) until perforation.

5.3 Results and Discussion

Figure 5.3 shows the TEM image of as-synthesized 8 nm/2nm core/shell and mixed 8 nm FePt/ 4 nm Fe_3O_4 nanoparticles. The ratio of Fe and Pt was kept same as in both of them to obtain similar magnetic properties. The main purpose to prepare FePt/Fe_3O_4 nanoparticles with two different morphologies was to compare their post-compaction magnetic properties and

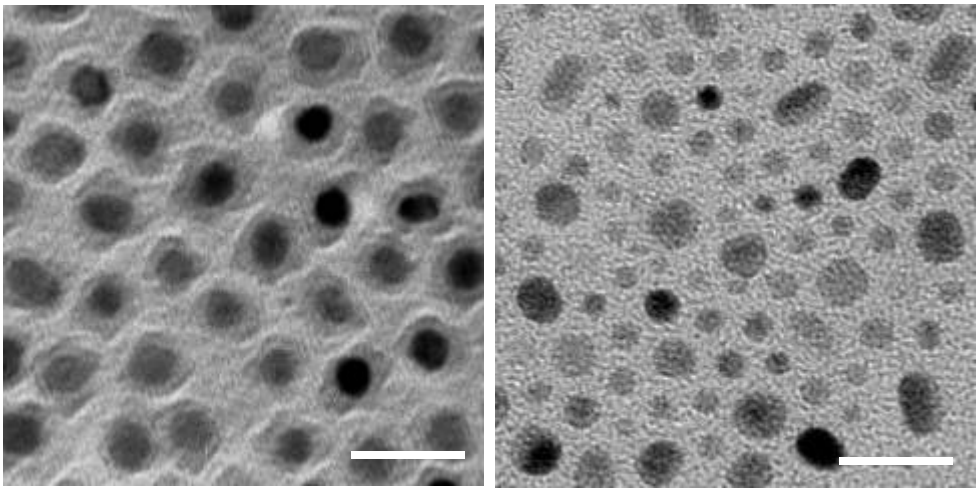

Figure 5.3 TEM image of as-synthesized (a) 8 nm/2nm core/shell and (b) mixed 8 nm FePt/ 4 nm Fe_3O_4 nanoparticles (the scale bar is 20 nm).

Figure 5.4 Photographic image of bulk sample of core/shell nanoparticles compacted at 600 ºC.

find out which morphology given better exchange coupling and hence higher energy product. Figure 5.4 shows the photographic image of bulk sample of core/shell nanoparticles compacted at 600 ºC.

5.3.1 Density

It is known that the limit for density of a randomly packed particle system is only 64% if no deformation is involved.[128] To obtain a higher density, it is necessary to realize plastic deformation of the particles. For nanoparticles, the deformation is not as easy as for large particles because of the reduced dislocations in the particles, which explains low density values obtained in nanoparticle compacts. Figure 5.5 shows the dependence of density of the core/shell and mixed nanoparticles bulk samples on the compaction temperature (*T*cp). One can see that the density increased monotonously with compaction temperature for both core/shell and mixed FePt/Fe_3O_4 nanoparticles compacts. The mixed nanoparticles compact prepared at pressure 2.0 GPa and *T*cp of 600 °C has the highest density (11.7 g/cm^3) which is about 84% of the full density value (14.5 g/cm^3) for the FePt/Fe_3Pt composite. Such high density is a result of a significant plastic deformation of the nanoparticles at the applied high pressure.

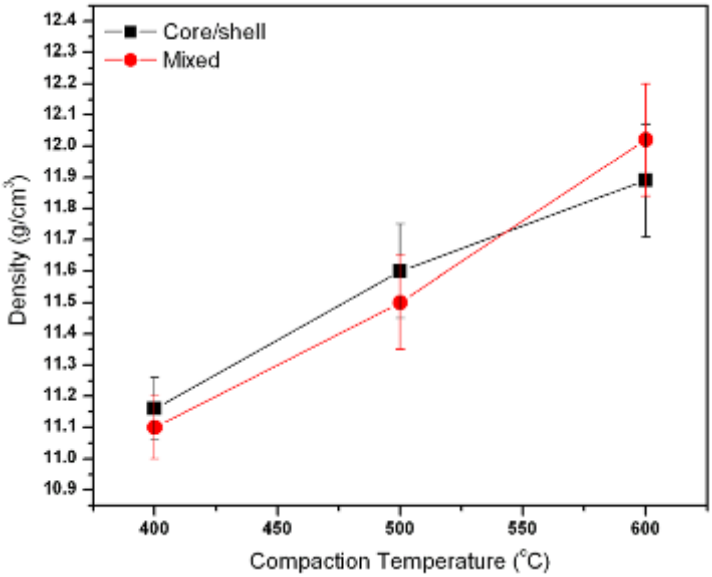

Figure 5.5 Dependence of density on compaction temperature for (a) core/shell and (b) mixed FePt/Fe_3O_4 nanoparticles compacts.

5.3.2 Phase Transition

XRD patterns of the bimagnetic core/shell FePt/Fe_3O_4 nanoparticles bulk samples compacted at 400, 500 and 600 °C are shown in Figure 5.6. For comparision, the XRD pattern of uncompacted core/shell nanoparticles (starting powders) have also been shown. It can be seen that the starting powders mainly consists of fcc FePt and Fe_3O_4 phases. The compaction at 400 °C led to the phase transition of FePt component from fcc to $L1_2$ structure while Fe_3O_4 was still existing. With increasing *T*cp up to 600 °C, the fcc FePt phase completely converted into $L1_2$ phase and the Fe_3O_4 still existed.

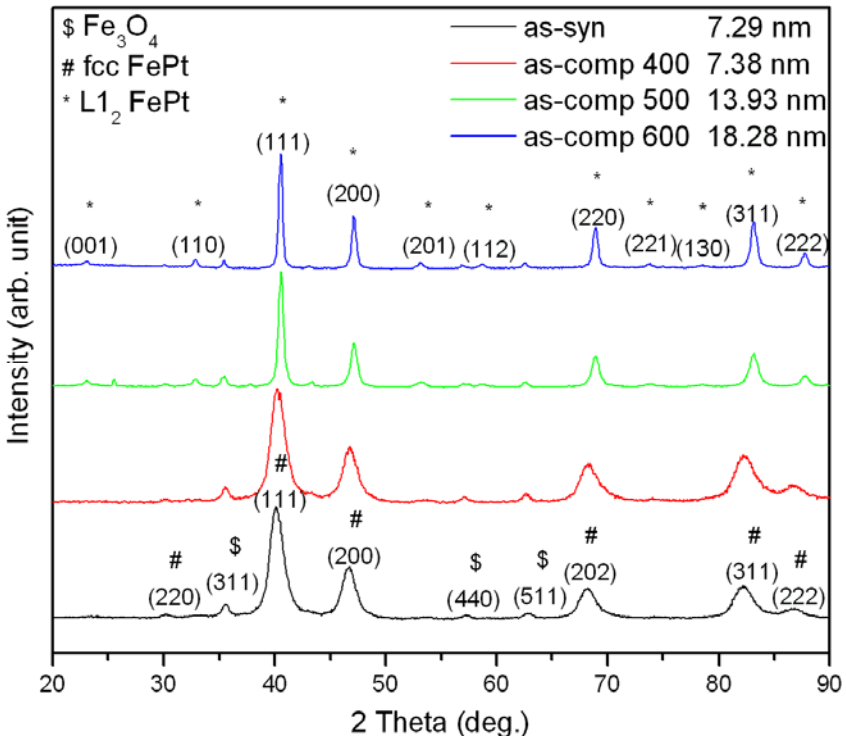

Figure 5.6 XRD of as-synthesized core/shell FePt/Fe_3O_4 nanoparticles and their bulk samples compacted at 400, 500 and 600 °C.

Since the $L1_2$ phase of as-compacted samples had low magnetic anisotropy, they were annealed at 650 °C for 1 hour in forming gas to convert $L1_2$ FePt phase into high anisotropic $L1_0$

phase. During annealing Fe_3O_4 was reduced and converted into Fe or Fe_3Pt and as a result, FePt/Fe_3Pt nanocomposite was formed. Figure 5.7 shows XRD of core/shell FePt/Fe_3O_4 nanoparticles (starting powders) and their bulk samples compacted at 400, 500 and 600 °C and post-annealed at 650 °C for 1 hour in forming gas. It can be seen that both, powders and compacted samples converted to chemically ordered $L1_0$ FePt phase. However, it is very hard to index Fe_3Pt peaks separately since they are very similar to $L1_0$ FePt peaks. The grain size calculated from the XRD patterns using Scherrer's formula also has been given in the Figure 5.7. The final grain size in annealed free powders was found higher than post annealed compacted samples which indicated control in grain growth after warm compaction of nanoparticles.

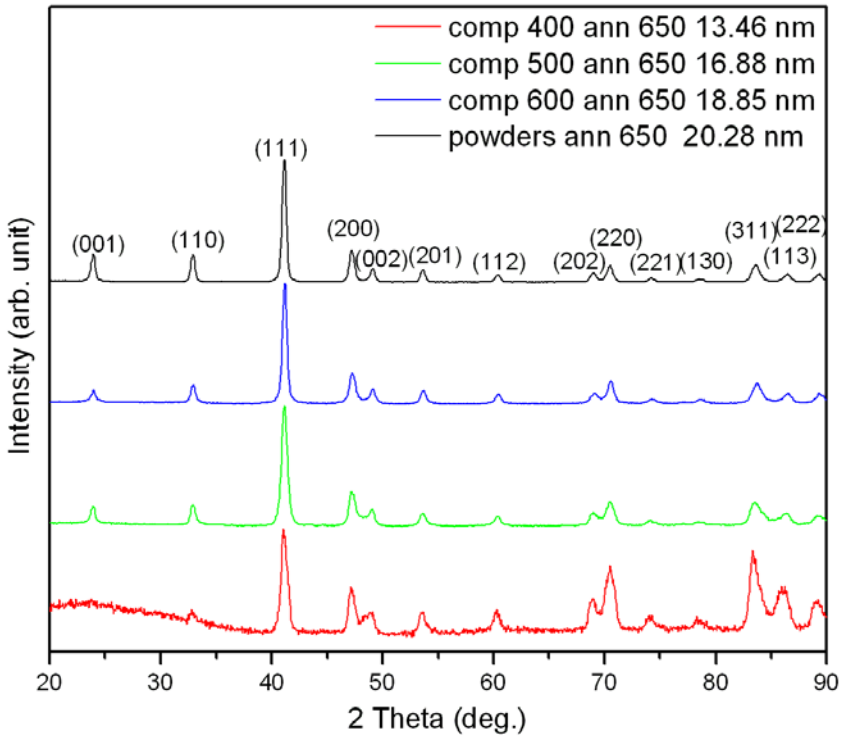

Figure 5.7 XRD of core/shell FePt/Fe_3O_4 nanoparticles and their bulk samples compacted at 400, 500 and 600 °C and post annealed at 650 °C for 1 h in forming gas.

5.3.3 Grain Size

To quantitatively determine the effect of warm compaction on the microstructure, the grain size of FePt were determined from the XRD patterns in Figure 5.6 and 5.7 using the Scherrer's formula.[129] Figure 5.8 shows the dependence of grain size on the compaction temperature for both core/shell and mixed FePt/Fe_3O_4 starting powders and their compacts. As we can see from Figure 5.8, the grain size increased linearly with *Tcp* up to 20.9 and 22.1 nm for core/shell and mixed nanoparticles, respectively when *T*cp was 600 °C. Nevertheless, the grain size was still under control in the nanoscale. The grain size of post-annealed (forming gas at 650 °C for 1 h) compacted samples was also included in Figure 5.8 to illustrate the effect of heat treatment on the morphology. It is found that the annealing led to the grain growth from 7.3 to 13.4 nm for the 400 °C core/shell nanoparticles compacted sample, while only from 18.1 to 19.8 nm for the sample with *Tcp* was 600 °C. The similar pattern was obtained for mixed nanoparticles though the grain size in mixed nanoparticles was higher than core/shell nanoparticles in both as-compacted and post annealed compacted samples. It may be because the Fe_3O_4 shell in core/shell nanoparticles protected the FePt core from sintering as reported previously.[119]

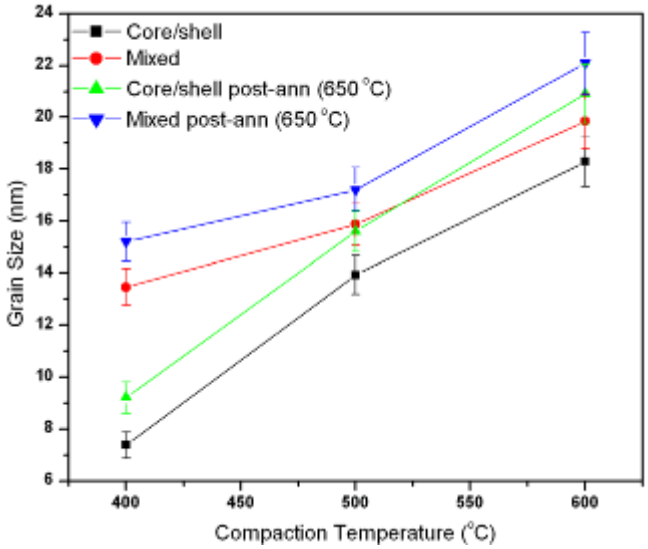

Figure 5.8 Dependence of grain size on compaction temperature for FePt/Fe_3O_4 core/shell and mixed nanoparticles as-compacted and post-annealed compacted samples.

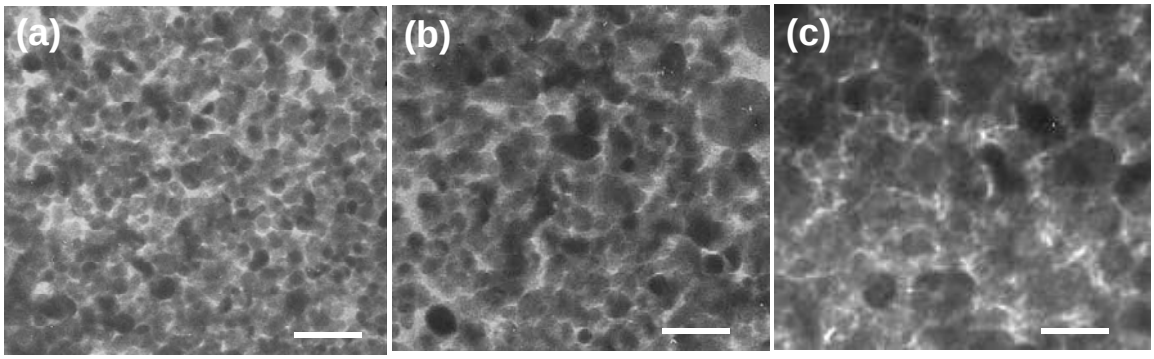

Figure 5.9 TEM images of FePt/Fe_3O_4 core/shell nanoparticles bulk samples compacted at (a) 400, (b) 500, and (c) 600 °C (the scale bar is 20 nm).

Figure 5.9 shows the bright field TEM images of the bulk samples of core/shell FePt/Fe_3O_4 nanoparticles compacted under 2.0 GPa pressure at 400, 500 and 600 °C. The TEM images show that grain size increases with *T*cp as expected. The grain size is about 7±2 nm, 14±3 and 20±5 nm for the 400, 500 and 600 °C-compacted samples, respectively. The grain size and size distribution are quite small compared to those for bulk materials fabricated by traditional techniques. This is also in agreement with Figure 5.8 that exhibits the dependence of average grain size on the compaction temperature.

5.3.4 Exchange Coupling and Magnetic Properties

5.3.4.1 Magnetization and Coercivity

Figure 5.10 shows the dependence of saturation magnetization (*Ms)* measured in an applied field of 7 T) and coercivity (*Hc)* on compaction temperature (*T*cp) for as-compacted samples of core/shell and mixed FePt/Fe_3O_4 nanoparticles while assuming their density equal to theoretical density. The value of *Ms* and *Hc* at *T*cp = 20 °C is actually from the starting powders for both core/shell and mixed FePt/Fe_3O_4 nanoparticles. The starting core/shell powders had almost no coercivity, while the 400 °C compacted sample gave *Hc* of 288 Oe which was further increased to 322 Oe with increase in Tcp from 400 to 600 °C. The similar pattern was also observed starting mixed powders. The slight increase in coercivity originated from the formation

of the $L1_2$ phase. $L1_2$ FePt is a face centered cubic structure and chemically ordered, in which the Pt atoms occupy the face centers while the Fe atoms occupy the corners. Due to the ordering, It is ferromagnetic and exhibit a low coercivity and saturation magnetization of 720 emu/cc. However, the magnetization of fcc FePt phase is 950 emu/cc. This was also the reason the *Ms* value was decreased when particles were compacted at 400 °C. The further increase of *T*cp resulted in a further decrease of *Ms*, due to the complete development of $L1_2$ FePt phase during the compaction. There was a slight difference in Ms values of core/shell and mixed nanoparticles compacted samples for any compaction temperature which could be due to the difference in their final grain size as discussed in section 5.3.3.

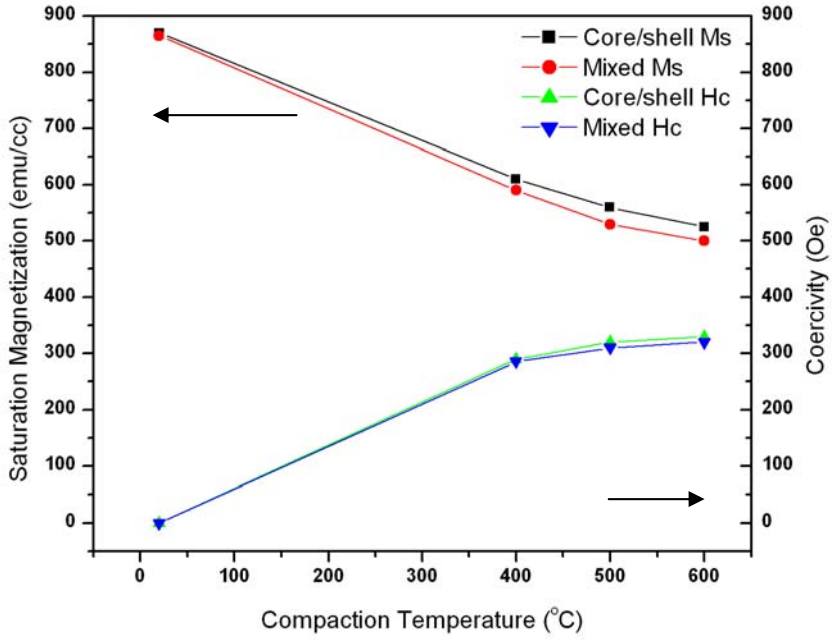

Figure 5.10 The dependence of saturation magnetization (*Ms)* and coercivity (*Hc)* on compaction temperature (*T*cp).

Since the coercivity of as-compacted $FePt/Fe_3O_4$ samples was significantly low, they were annealed under forming gas (93% Ar + 7% H2) for 1 h to improve their coercivity. The magnetization as well as their coercivity and hence the energy product of the compacted

samples were drastically increased after annealing. Figure 5.11 shows dependence of Remenance Ratio (Mr/Ms) on compaction temperature (*Tcp*) for the post-annealed core/shell and mixed nanoparticles bulk samples. The increase in *Ms* of the post-annealed compacted samples (both core/shell and mixed FePt/Fe_3O_4 nanoparticles) was attributed to the decomposition of Fe_3O_4 phase and the formation of Fe or Fe_3Pt with high magnetization in the reducing atmosphere. *Ms* value up to 1090 emu/cm3 was obtained by post-annealing. It is also found that the *Ms* of the core/shell and mixed nanoparticles post annealed compacted samples was very similar. However, the Mr values were higher for core/shell nanoparticles compacts which resulted in higher values of remanence ratio (*Mr/Ms*) for core/shell nanoparticles compacts as shown in Figure 5.11. This may be due to the better hard/soft phase exchange coupling in core/shell nanoparticles than mixed nanoparticles. This phenomenon has been explained in details later in the section 5.3.4.3.

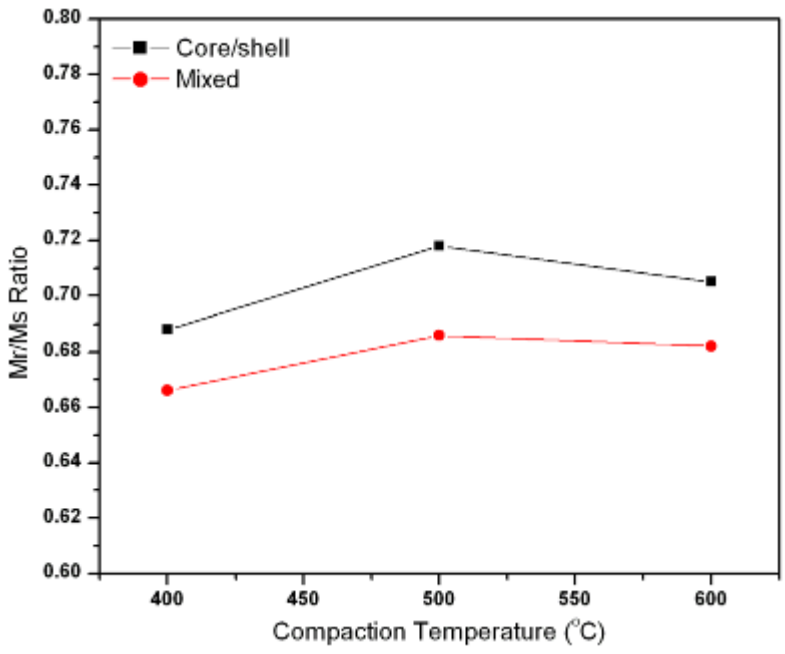

Figure 5.11 Dependence of remanence ratio (Mr/Ms) on compaction temperature (*Tcp*) for the post-annealed FePt/Fe_3O_4 core/shell (c/s) and mixed (mix) nanoparticles bulk samples.

Figure 5.12 shows dependence of coercivity *(Hc)* on compaction temperature (*Tcp*) of the post-annealed core/shell and mixed nanoparticles bulk samples. Similar to Ms, the Hc of all the compacted samples increased after annealing which shows that the phase transition from $L1_2$ to $L1_0$ resulted in magnetic hardening. It is also found that the *Hc* of the core/shell and mixed nanoparticles sample was also very similar however, the Hc seems to decrease with higher compaction temperature. The reason of this decrease may be an overgrowth in grain size due to post annealing of samples. The grain size of samples was already increased after compaction and was highest for samples compacted at 600 C. Therefore further growth of grain size during annealing attributed to deterioration of coercivity based on their compaction temperature.

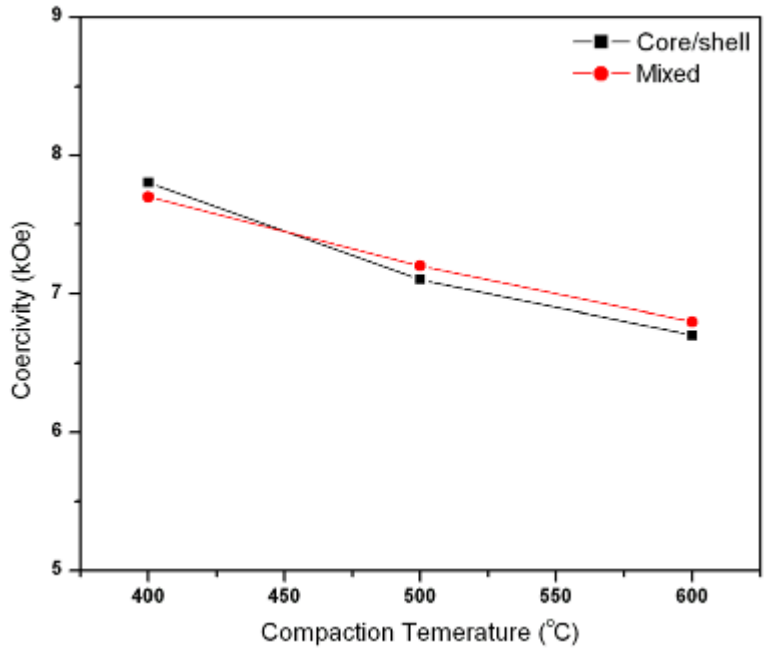

Figure 5.12 Dependence of coercivity *(Hc)* on compaction temperature (*Tcp*) for the post-annealed core/shell and mixed nanoparticles bulk samples.

5.3.4.2 Energy Product

All the efforts in controlling grain size are made for the purpose to realize intergrain magnetic exchange coupling and thus to achieve high energy products ($(BH)_{max}$). The energy

product dependence on compaction temperature (*Tcp*) of the post-annealed core/shell and mixed nanoparticles bulk samples has been given in Figure 5.13. The energy product for post-annealed core/shell nanoparticles compacts were found higher than mixed nanoparticles which could be due to the higher Mr values of core/shell nanoparticles compacts (Figure 5.10). The higher Mr values improve the squareness of the hysteresis loops and therefore the energy products. The energy product based on the theoretical density was highest for bulk samples compacted at 500 ºC for both core/shell and mixed $FePt/Fe_3O_4$ nanoparticles. The highest energy product in all the bulk samples found was 18.1 MGOe (core/shell nanoparticles compacted at 500 ºC and post annealed at 650 ºC) based on the theoretical density which is 39.2% higher than the theoretical limit 13 MG Oe for the single phase isotropic FePt magnets. If compared with the highest energy product obtained in core/shell nanoparticles assembled thin films (17.8 MGOe), these results clearly imply that there was no deterioration of magnetic properties of nanoparticles after compaction.

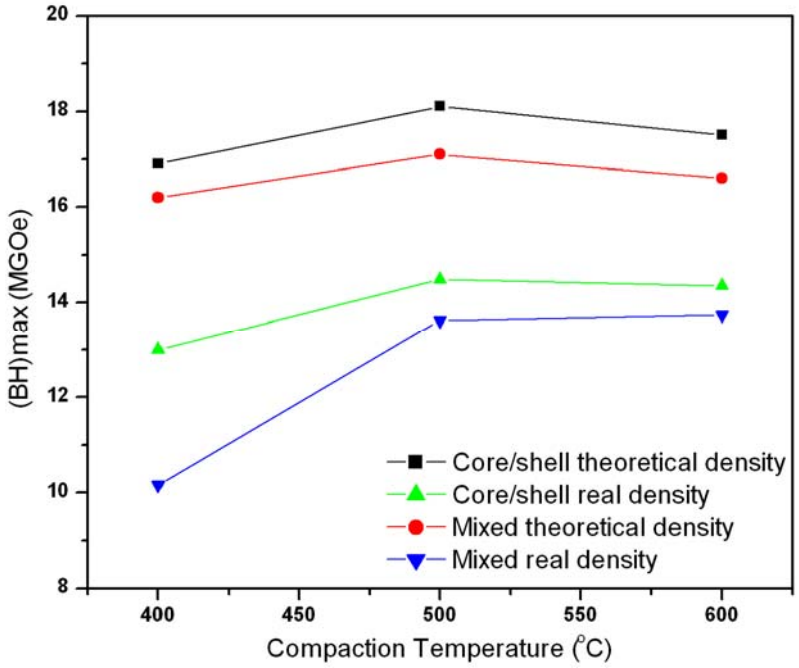

Figure 5.13 Dependence of energy product *((BH)$_{max}$)* on compaction temperature (*Tcp*) for post-annealed core/shell and mixed nanoparticles bulk samples based on their theoretical and real densities.

The energy products for core/shell and mixed nanoparticles compacts based on their real density also has been given in the Figure 5.13. Based on the real density, the highest energy product found for core/shell nanoparticles was 14.5 MGOe (compacted at 500 C) and 13.8 MGOe for mixed nanoparticles (compacted at 600 ºC).

5.3.4.3 Delta M Curves

To understand the difference in exchange coupling strength in core/shell and mixed nanoparticles compacts, Delta M (δ*m)* measurements (Henkel plots) were performed as discussed in section 4.3.3.3.[130–132] The value of the δ*m* can be calculated as δ*m* = m_d (*H*)−[1−2m_r (*H*)] where m_d is demagnetization remanence and m_r is isothermal magnetization remanence. Both of these values are normalized by the saturation remanence. Nonzero δ*m* is caused by magnetic interactions between particles or grains. The positive δ*m* is interpreted as a sign for magnetic exchange coupling and the negative δ*m* is a sign of magnetic dipolar interaction. Figure 5.14 shows δm plots of core/shell and mixed nanoparticles bulk samples compacted at 500 °C and post annealedat 650 °C. These particular samples were chosen to compare since they both gave the highest energy product. The δm value for the core/shell sample is found higher than mixed nanoparticles compacted sample, indicating stronger exchange coupling in the former. This is also reflected by the shape of the demagnetization curves of core/shell and mixed nanoparticles bulk samples compacted at 500 °C and post annealed at 650 °C, as shown in the Figure 5.15. The squareness of core/shell nanoparticles compacted samples was better than mixed nanoparticles compacts. The remanence ratio (*Mr* /*Ms*) was calculated where *Mr* and *Ms* is the remanent and saturation magnetization. The *Mr*/*Ms* of the core/shell nanoparticles compacted sample (0.72) is higher than that of the mixed nanoparticles compacted samples (0.67), which is also consistent with the δ*m* measurement.

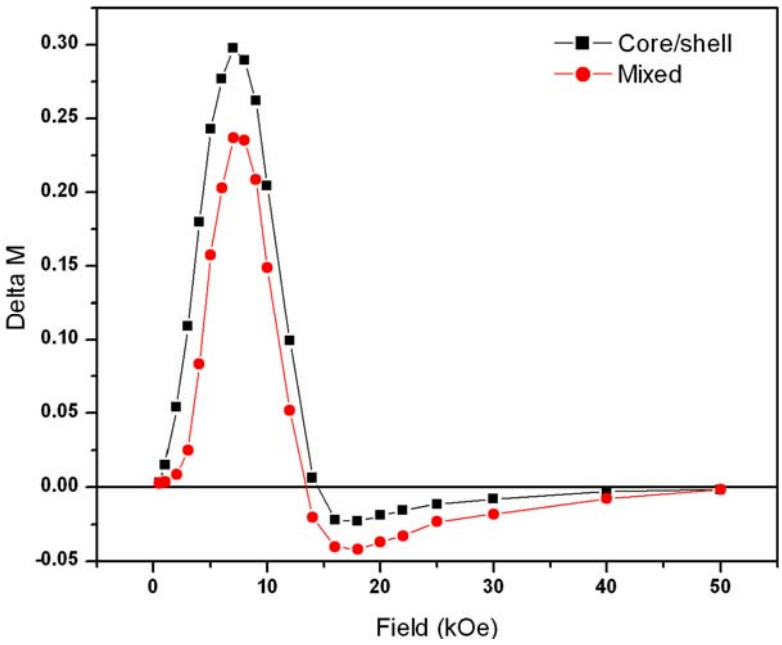

Figure 5.14 δm plots of core/shell and mixed nanoparticles bulk samples compacted at 500 °C and post annealed at 650 °C.

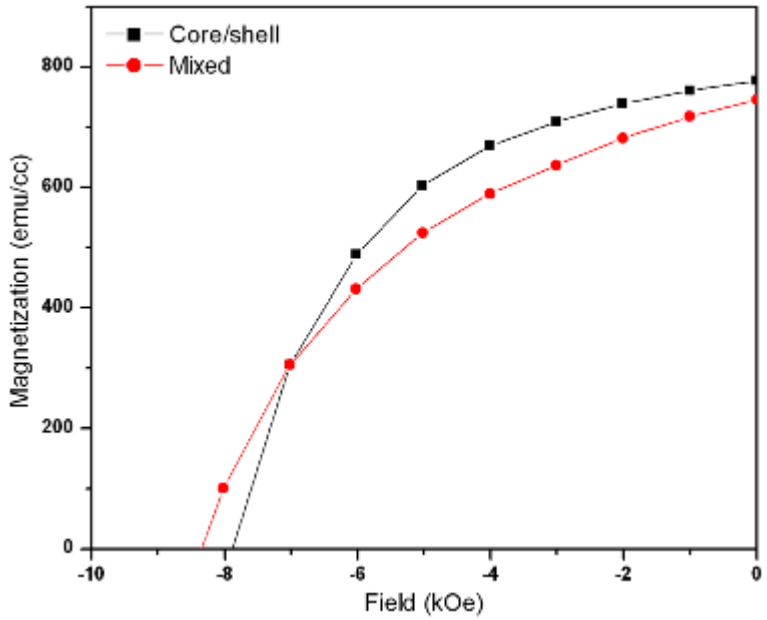

Figure 5.15 Demagnetization curve of core/shell and mixed nanoparticles bulk samples compacted at 500 °C and post annealed at 650 °C.

5.4 Conclusion

High density FePt/Fe_3Pt bulk nanocomposite magnets have been obtained by the warm compaction method. The chemically synthesized 8 nm/2 nm FePt/Fe_3O_4 core/shell and 8nm FePt/ 4nm Fe_3O_4 mixed nanoparticles with similar magnetic properties were compacted under 2.0 GPa at 400 °C, 500 °C and 600 °C. A density up to 84% of the full density has been achieved while the nanoscale morphology is retained. The fcc FePt phase was changed to $L1_2$ FePt phase during the compaction while Fe_3O_4 phase still existed. After annealing 650 °C in forming gas (93% Ar + 7% H_2) for 1h, the FePt/Fe_3O_4 compacted samples were converted into $L1_0$ FePt/Fe_3Pt magnetic nanocomposite. The nanoscale morphology was retained even after post-annealing for both core/shell and mixed nanoparticles bulk samples. Magnetic properties of bulk samples were significantly improved after annealing. There was no deterioration of magnetic properties of nanoparticles after compaction. The highest energy product in all the bulk samples found was 18.1 MGOe (core/shell nanoparticles compacted at 500 ºC and post annealed at 650 ºC) based on the theoretical density which is 39.2% higher than the theoretical limit of 13 MG Oe for the single phase isotropic FePt magnets. Based on the real density, the highest energy product found was 14.5 MGOe. It was found by measuring δm that the core/shell nanoparticles compacted samples have more effective exchange coupling and hence higher energy products than mixed nanoparticles compacted samples. Our results show that warm compaction technique is promising for producing high performance bulk nanocomposite magnets for advanced applications.

CHAPTER 6

SYNTHESIS AND CHARACTERIZATION OF FePt/Au and FePtAu NANOPARTICLES

6.1 Introduction

Magnetic nanoparticles have been proposed for biomedical applications[54, 66] due to their controllable size (5-100 nm) and ability to move under external magnetic fields. However, as-synthesized particles can not be used directly without further functionalization. They must be chemically stable, biocompatible and their surface should be easy to functionalize. If thin Au layer is coated on the surface of magnetic nanoparticles then the gold coated magnetic nanoparticles can be easily used in magnetically driven biomedical applications since Au satisfies all three conditions mentioned above. [133,134] However, so far for all the biomedical applications, only Au coated superparamagnetic nanoparticles have been available. There are several reports on the synthesis of binary metallic oxide/Au nanoparticles either in form of core/shell[135,136] or dumb-bell shapes where gold has been coated or attached to metallic oxide magnetic nanoparticles.[137,138] However, the bio-applications of oxide/Au nanocomposites are limited due to the super-paramagnetic behavior of the oxide nanoparticles. Single domain ferromagnetic nanoparticles can have better signals in magnetic sensors or respond more readily to an applied field gradient than superparamagnetic nanoparticles of the same size. Currently available ferromagnetic nanoparticles such as Fe and Co less than 10 nm are superparamagnetic. On the other hand, nanoscale Fe particles are so unstable that they will spontaneously burst into flames when exposed to air. Co particles are less reactive, but an oxide coating will still form if exposed to air. FePt nanoparticles are an important class of magnetic nanoparticles since they show ferromagnetism and chemical stability even when particle size down to 3 nm.[139] The syntheses of FePt/Au heterostructured nanoparticles have been reported as a strong candidate of biological detection.[140,141]

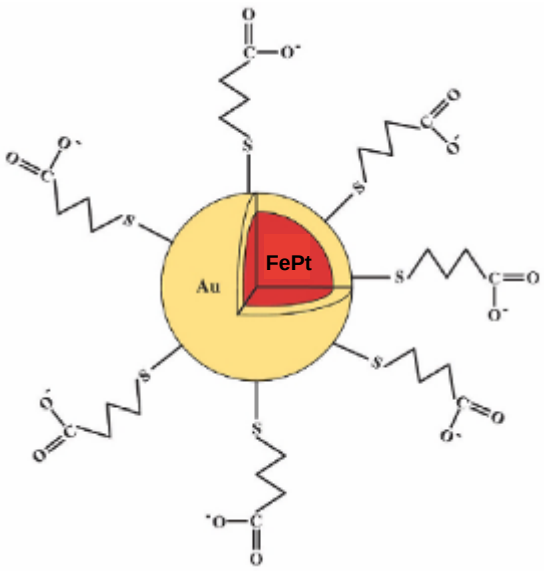

Figure 6.1 Au coated FePt nanoparticles attached to functional groups through Au-S bonds.

In the first part of this chapter, we report the synthesis of FePt/Au core/shell nanoparticles using solution phase chemistry. First FePt nanoparticles were synthesized and then coated with Au layer. Au coating not only prevent any reaction with the external environment, it also provides a good surface for subsequent functionalization with chemical or biological agents (Figure 6.1). For example, if we want to attach an organic molecule to the particle, we can take a thiol or S group and use a covalent bond with the Au to attach it. Though as-synthesized FePt nanoparitcles has disordered fcc crystal structure and are superparamagnetic in nature, they can be converted to $L1_0$ phase which is ferromagnetic after annealing at 400 °C.

Another potential application, for which FePt nanoparticles are the most suitable candidates, is recording media. Magnetic recording technology has made tremendous gains in data storage density, partly by scaling down the grain size of thin-film media. However, further scaling to support future increases will bring the grain sizes near the superparamagnetic limit. This has led to a search for new materials and new microstructures for magnetic recording. The

magnetocrystalline anisotropy of these materials must be high enough to prevent thermal decay of written information on magnetic recording media. The FePt-base nanostructured materials are excellent candidates because of their good chemical stability and high magnetocrystalline anisotropy (~10^7 erg/cc) observed in the ordered intermetallic phase.[142,143] This large crystalline anisotropy allows for thermally stable grain diameters down to 2.8 nm. The synthesis and characterization of a well-organized magnetic array of such particles can contribute to the design of a magnetic medium capable of recording densities beyond 1 Tb/in^2.[144,145] The challenges to realize this Tb/in^2 goal are to make uniform high-coercivity FePt nanoparticles and nanoparticle assemblies with controlled assembly thickness, surface roughness, and mechanical robustness.

A report by Sun *et al.* has generated considerable interest in the use of self-assembled FePt nanoparticles for ultrahigh-density recording media.[71] These nanoparticles are coated with an organic surfactant and can be dispersed in hydrocarbon solvents. When the dispersions are cast onto solid substrates and the solvent evaporates, and these nanoparticles self-assemble into ordered two- or three-dimensional arrays. However, as-synthesized FePt nanoparticles are of disordered fcc structure and should be annealed at above 500 ^oC to convert to ordered $L1_0$ structure that has high magnetocrystalline anisotropy.[71] From a practical viewpoint, such high temperature processing is unsuitable for mass-production of magnetic recording media. In addition, at this temperature, the surfactant protecting nanoparticle decomposes which results in particle sintering and grain growth, leading to wide size distributions and deterioration of the monodispersity and nanomorphology of the particles.[146] This breakdown is highly detrimental for maintaining ultra-high density bit cell sizes. Several methods have been developed to produce thin particle films with controlled thicknesses that are more resistant to sintering during annealing. Sun and coworkers have used a layer-by-layer deposition process in which monolayers of FePt nanoparticles are separated by a polymer layer, reducing sintering and allowing accurate control of the coating thickness.[147,148] Momose et al. have used spin coating

to produce uniform films with controllable thickness.[149] By adjusting the spin conditions with excess surfactant in the dispersion, they were able to substantially reduce sintering during the annealing process. Yu et al. have used an amino-functional silane coupling layer to anchor the FePt nanoparticles to a silicon surface.[150] No significant sintering occurred after annealing at 800 ^{o}C; however, chemical ordering to the $L1_0$ phase was weak, suggesting a possible connection between sintering or particle size and degree of order.[151]

Our approach has been directed towards reducing the ordering temperature of this alloy, thereby reducing the annealing temperature and thermal energy for sintering.[152-158] Kitakami *et al.* found that the addition of Sn, Pb, Sb, Bi, Au and Ag into sputtered CoPt thin films promotes a disordered–ordered transformation, resulting in an appreciable reduction of the temperature for ordering.[159,160] They also stated that the ordering is promoted by defects produced by the additives during annealing, because those additives have very low surface energy and are easy to segregate.[161] Additive Au have been found to be effective in sputtered FePt films to decrease the ordering temperature.[162] FePd is a well-known high-anisotropy $L1_0$ material, and additive Cr is used extensively in magnetic thin film media for grain isolation. In the second part of chapter we also report a composition controlled synthesis of Au doped FePt nanoparticles. It has been found that by tuning the concentration of Fe, Pt and Au in $Fe_xPt_yAu_{100-x-y}$ nanoparticles, the phase transition temperature can be reduced by more than 200 ^{o}C without sacrificing saturation magnetization of FePt nanoparticles.

6.2 Experimental

6.2.1 Synthesis of FePt/Au Core/Shell Nanoparticles

FePt/Au core/shell nanoparticles were synthesized using seed-mediated approach which consists of a synthesis of FePt nanoparticles and then Au coating over FePt nanoparticles. 8 nm FePt nanoparticles, which were used as seeds, were prepared via reduction of $Pt(acac)_2$ and decomposition of $Fe(CO)_5$ under argon gas. FePt nanoparticles were then taken as seeds and an Au shell was grown over it by reductive decomposition of

$Au(CH_3CO_2)_3$ in presence of surfactants. The key parameter of producing Au coating over FePt nanoparticles is the type of solvent used for the synthesis of FePt nanoparticles. Different solvents were used for FePt nanoparticles synthesis and it was found that FePt surface can be homogeneously coated with Au shell only if FePt nanoparticles are synthesized using benzyl ether as solvent. In case of other solvents either coating did not take place or FePt nanoparticles were not homogeneously coated. An outline of the reaction route is presented in the Figure 6.2.

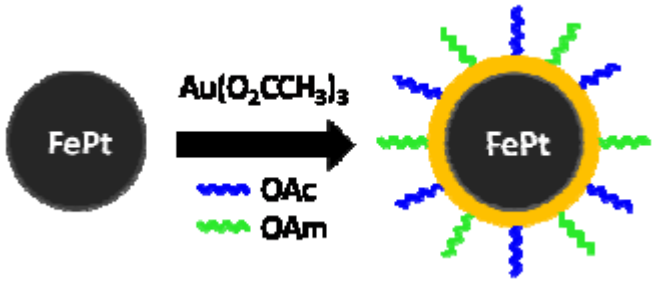

Figure 6.2 Schematic showing synthesis of FePt/Au core/shell nanoparticles.

To prepare 8 nm FePt nanoparticles, similar recipe as mentioned in section 3.2 was used. 5 mL of hexane dispersed 8 nm FePt nanoparticles (approximately 30 mg), $Au(CH_3CO_2)_3$ (0.13 mmol, 50 mg), 1,2-hexadecanediol (0.69 mmol, 180 mg), benzyl ether (15 mL), oleic acid (6.2 mmol, 2.0 mL) and oleylamine (5.9 mmol, 2.0 mL) were added into the 125 mL flask containing a magnetic stir bar under Ar gas flow. The flask was heated up to 100 ºC and held for 10 min to evaporate the hexane, then heated up to 190 ºC with heating rate of 1 ºC/min and refluxed at this temperature for 15 h. The solution started changing color from black to dark red at around 150 ºC, suggesting the nucleation of Au nanoparticles. After 15 h of reflux, the solution was cooled down to room temperature under Ar gas flow. The dark red FePt/Au core/shell nanoparticles were precipitated by adding 30 mL of ethanol and separated by centrifugation at 6000 rpm for 20 min. The product was washed three times using mixture of

hexane and absolute ethanol (10 mL hexane and 35 mL ethanol) and finally the precipitated particles were dispersed in 15 mL of hexane.

6.2.2 Phase Transfer of FePt/Au Core/Shell Nanoparticles

15 mL of hexane dispersed FePt/Au core/shell nanoparticles capped with oleic acid and oleyl amine ligands were mixed with 15 mL of hexane and 15 mL of octane in a 50 mL centrifuge tube. 5.0 mL of a saturated solution of 11-mercaptoundecanoic acid in cyclohexanone were added into the tube and the tube was placed in an ultrasonication water bath. After 10 min of ultrasonic, the dark red solution was separated by centrifugation at 6000 rpm for 20 min. The particles were rinsed first with cyclohexanone, then ethanol, and finally with acetone until the supernatant were clear. After each wash, the particles were centrifuged at 6000 rpm for 20 min and redispersed with a minimal amount of cyclohexanone. The particles were then added to a vial filled with 5 mL of distilled water and 1 mL of ammonium hydroxide (NH_4OH). After shaking, a dark red dispersion of the FePt/Au core/shell particles in water was obtained.

6.2.3 Synthesis of FePtAu Nanoparticles

$Fe_xPt_yAu_{100-x-y}$ nanoparticles were prepared by the polyol method reported by Kang *et. al.*[155] with slight modification. All the reactions were carried out using standard schlenk line technique. In brief, 0.5 mmol of platinum acetylacetonate ($Pt(acac)_2$) and designated amount of gold acetate ($Au(ac)_3$) were added to 125 mL flask containing a magnetic stir bar and mixed with 10 mL of phenyl ether. After purging with argon for 30 min at room temperature, the flask was heated up to 80 ºC. Then, 0.5 mmol oleic acid, 0.5 mmol oleyl amine, and designated amount of iron pentacarbonyl ($Fe(CO)_5$) were added and then the solution was refluxed for 30 min before cooling down to room temperature. There was no additional reducing agent added in the reaction since the reduction potential of Au and Pt is too low, therefore $Pt(acac)_2$ and $Au(ac)_3$ can be reduced by oleyl amine itself.[163,164] The black product from the synthesis was precipitated by adding ethanol and separated by centrifugation and redispersed in hexane.

6.2.4 Purification, Annealing and Characterization of FePt/Au and FePtAu Nanoparticles

After being washed in ethanol three or more times, the FePt/Au and FePtAu nanoparticles were dispersed in hexane and stored in glass bottles under refrigeration. To prepare TEM samples, a drop of the nanoparticle dispersion solution in octane was put on the formvar side of a 300-mesh carbon coated copper TEM grid. The solvent was allowed to evaporate slowly in air and the nanoparticles self assembled on the grid. Samples for magnetic characterization were prepared by depositing a drop of the final hexane dispersion on a 3x3 mm^2 silicon substrate, evaporating the solvent at room temperature, and further drying in vacuum, which led to the formation of FePt/Au and FePtAu nanoparticle-assembled thin films. The FePt/Au samples were annealed at 400 °C for 1 h under the flow of forming gas (Ar+7%H_2) in a tube furnace while the FePtAu samples were annealed from 300 to 500 °C for 1 h in same reducing atmosphere.

The morphology and crystalline structure were characterized by scanning electron microscopy (SEM), transmission electron microscopy (TEM), and x-ray diffraction (XRD). The composition of the samples was checked by energy dispersive x-ray (EDX) analysis in SEM and TEM. Magnetic properties were measured with superconducting quantum interference device (SQUID) magnetometer with a maximum applied field of 70 kOe. The TEM images were recorded on a JEOL 1200 EX electron microscope at an accelerating voltage of 120 kV. Powder X-ray diffraction (XRD) spectra were recorded on a Philips MPD diffractometer with a Cu Kα X-ray source (*i*) 1.5405 Å). For FePt/Au nanoparticles, particle morphology, crystal structure and composition were also analyzed by high-resolution transmission electron microscope (HRTEM) with selected area electron diffraction (SAED), nano-beam diffraction (NBD), nano energy dispersive spectroscopy (nano-EDS). HRTEM analysis was done at University of Alabama and images were recorded on a JEOL 4000 electron microscope at an accelerating voltage of 400 kV. Ultra violet-Visible spectroscopy (UV-Vis) was used to determine the plasmon absorption band of Au nanoparticles.

6.3 Results and Discussion

6.3.1 Micro-structural Characterization on FePt/Au Core/Shell Nanoparticles

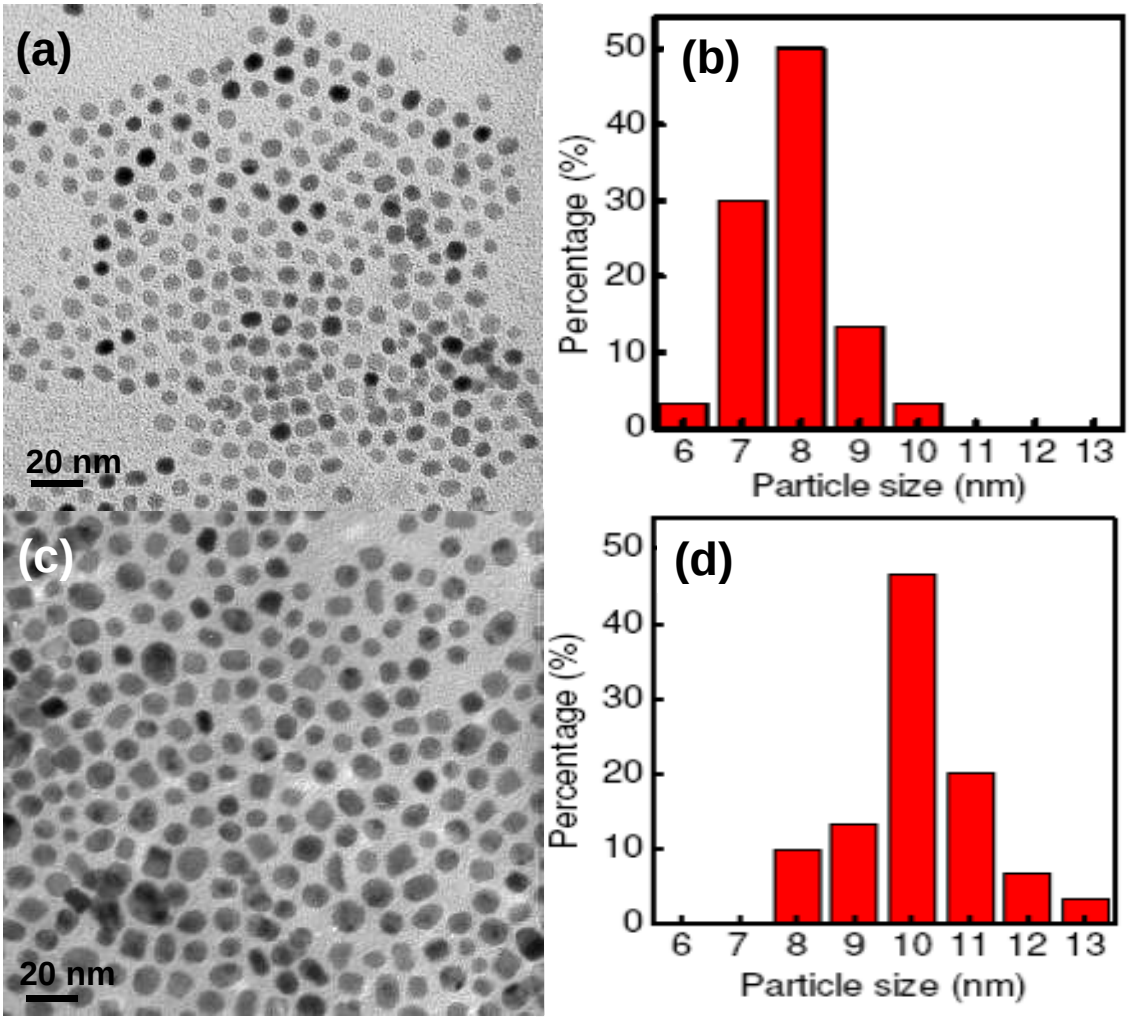

Figure 6.3 (a) TEM image and (b) the size distribution graph of FePt seed nanoparticles, (c) TEM image and (d) the size distribution graph of FePt/Au core/shell nanoparticles. The Au shell thickness was estimated to be ~1 nm.

Figure 6.3(a) shows the transmission electron microscope (TEM) image of monodisperse FePt nanoparticles and Figure 6.3(b) shows the size distribution graph of FePt nanoparticles taken as seeds, indicating 8 nm as an average size with narrow size distribution. Figure 6.3(c) and 6.3(d) show the TEM image and the size distribution graph of FePt/Au

core/shell nanoparticles. TEM analysis on FePt seed nanoparticles and FePt/Au core/shell nanoparticles revealed that the particle size increased from 8 nm of FePt particles to ~10 nm after Au shell was developed over the FePt core nanoparticles. It can also be seen that the particles contrast has been changed with increasing of particle size, suggesting that the surface morphology of FePt nanoparticles has been changed by Au coating.FePt/Au core/shell nanoparticles were further characterized by high-resolution TEM (HRTEM). As shown in Figure 6.4(a), the HRTEM image of FePt seed nanoparticles clearly shows the interfringe spacing of 0.224 nm and 0.196 nm, corresponding to the interplane distance of (111) and (200) planes in face centered cubic (fcc) FePt. In comparison, as shown in Figure 6.4(b) and 6.5(a), the HRTEM analysis on the shell region of FePt/Au core/shell nanoparticles revealed the interfringe spacing of 0.232-0.236 nm which is indexed as (111) plane in fcc Au, indicating the

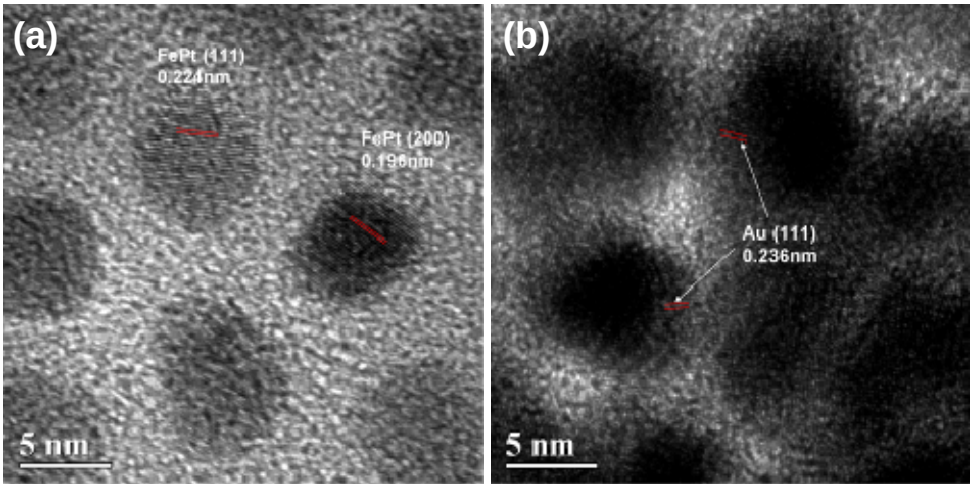

Figure 6.4 HRTEM image of (a) FePt nanoparticles with interfringe spacing of 0.224 nm (111) and 0.196 nm (200), and (b) FePt/Au core/shell nanoparticles with interfringe spacing of 0.236 nm (Au (111) of the shell region.

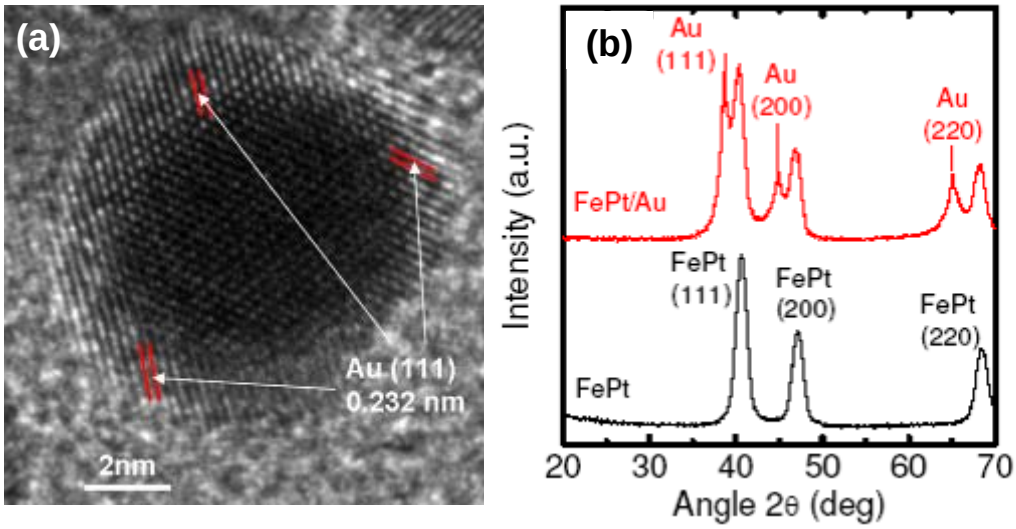

Figure 6.5(a) HRTEM image of FePt/Au core/shell nanoparticles with interfringe spacing of Au (111) in the shell region and (b) XRD patterns of FePt and FePt/Au core/shell nanoparticles.

FePt nanoparticles are successfully coated with crystalline Au shell.[165] Nevertheless, the interfringe of core region of FePt/Au core/shell nanoparticle is difficult to index due to the overlapping of fringes between FePt core and Au shell. This further suggested that FePt nanoparticles are completely encapsulated inside Au shell. X-ray diffraction patterns of FePt/Au core/shell nanoparticles shows the co-existence of FePt and Au peaks (Figure 6.5(b)), and further suggested the core/shell structure.

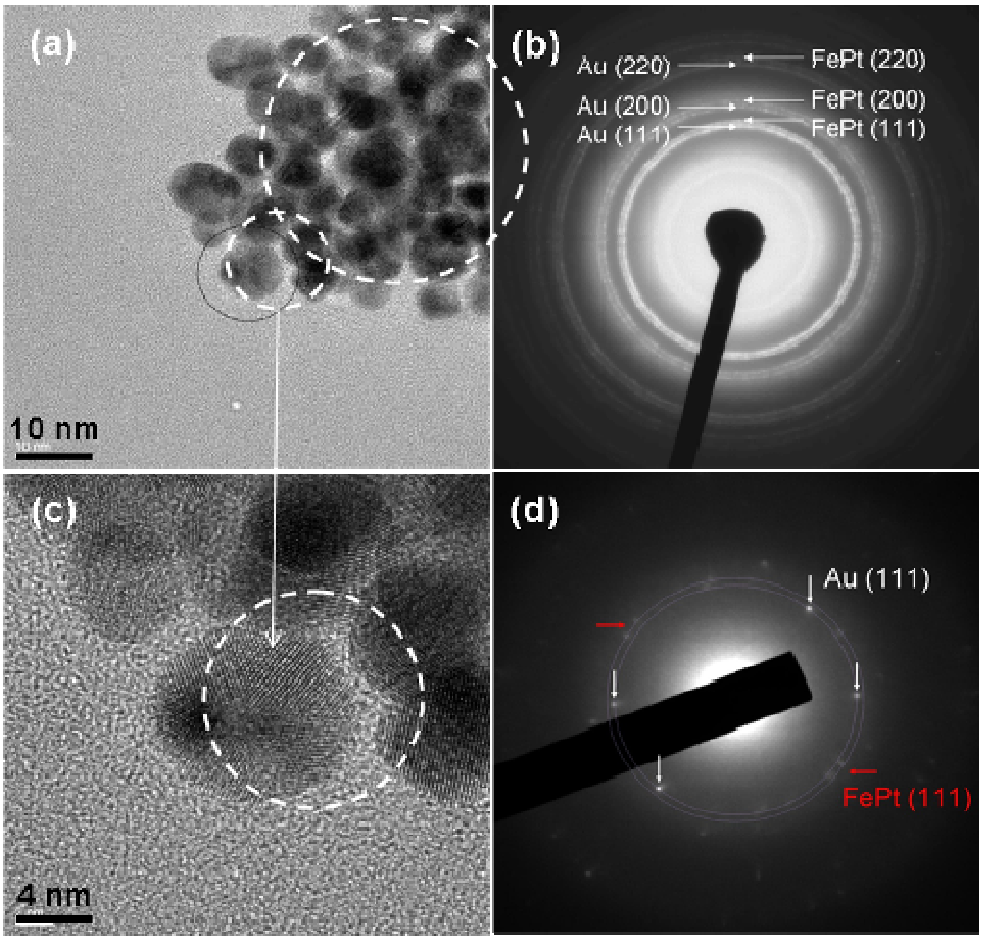

Figure 6.6 (a) TEM image and (b) SAED pattern for group of FePt/Au core/shell nanoparticles, (c) HRTEM image and (d) NBD pattern for single FePt/Au core/shell nanoparticle.

The diffraction studies including selected area electron diffraction (SAED) and nano-beam diffraction (NBD) further confirmed that FePt nanoparticles are coated with crystalline Au shells. The SAED pattern of group of particles show both the fcc Au and fcc FePt diffraction rings in the selected area (Figure 6.6(a) and 6.6(b)), implying the coexistence of FePt/Au core/shell nanoparticles. The NBD analysis on single particle shows the diffraction spots of FePt and Au (Figure 6.6(c) and 6.6(d)), suggesting the Au coating on FePt particle and single crystalline nature of the particle. Moreover, the nano-EDS spectrum confirmed the existence of Fe, Pt and Au elements in single FePt/Au core/shell nanoparticle (Figure 6.7).

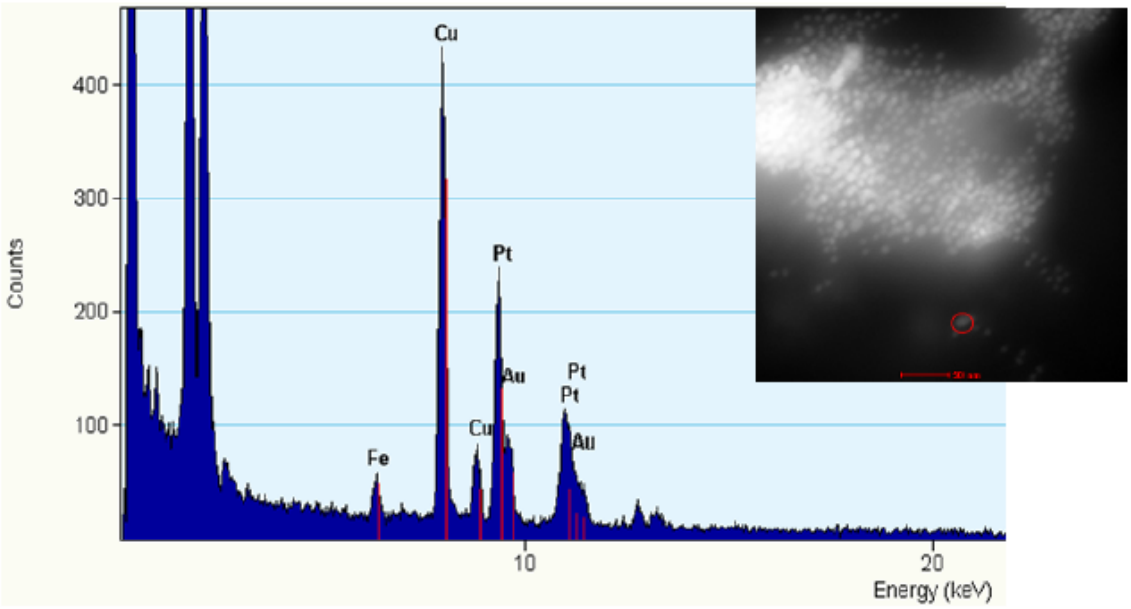

Figure 6.7 Nano-EDS spectrum of single FePt/Au core/shell nanoparticle.

6.3.2 Optical and Magnetic Properties of FePt/Au Core/Shell Nanoparticles

The small Au nanoparticles have a strong absorption band in the visible region, known as the surface plasmon.[166] For the FePt/Au core/shell nanoparticles, the surface plasmon band shows red-shift compared to the pure Au nanoparticles as shown in Figure 6.8, implying that the surface of Au nanoparticles has been changed after coating. In comparison, FePt nanoparticles do not show any characteristic absorption in the selected region. It is well known that Fe_3O_4/Au core/shell nanoparticles show the similar absorption band shift due to the morphology change induced by Au coating.[137,138]

Figure 6.9(a) shows the hysteresis loops of as-synthesized and annealed FePt/Au core/shell nanoparticles. Since the as-synthesized FePt nanoparticles have the disordered *fcc* phase which is super-paramagnetic at room temperature, the as-synthesized FePt/Au core/shell nanoparticles also show the super-paramagnetic loop. However, after annealing in forming gas (93% Ar + 7% H_2) at 400 °C for 1h, FePt/Au core/shell nanoparticles show coercivity of ~2 kOe, suggesting that FePt has transferred from disordered *fcc* phase to ordered $L1_0$ phase which has

strong magnetic anisotropy. In Figure 6.9(b), TEM image of FePt/Au core/shell nanoparticles after annealing shows that there is no significant agglomeration in the FePt/Au nanoparticles.

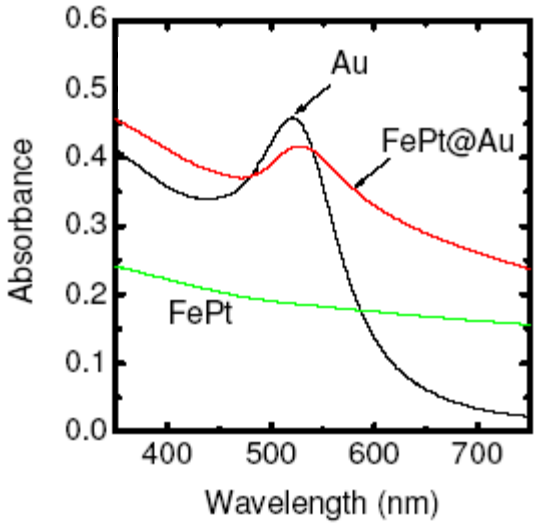

Figure 6.8 UV-Vis absorption spectra of FePt, Au and FePt/Au core/shell nanoparticles.

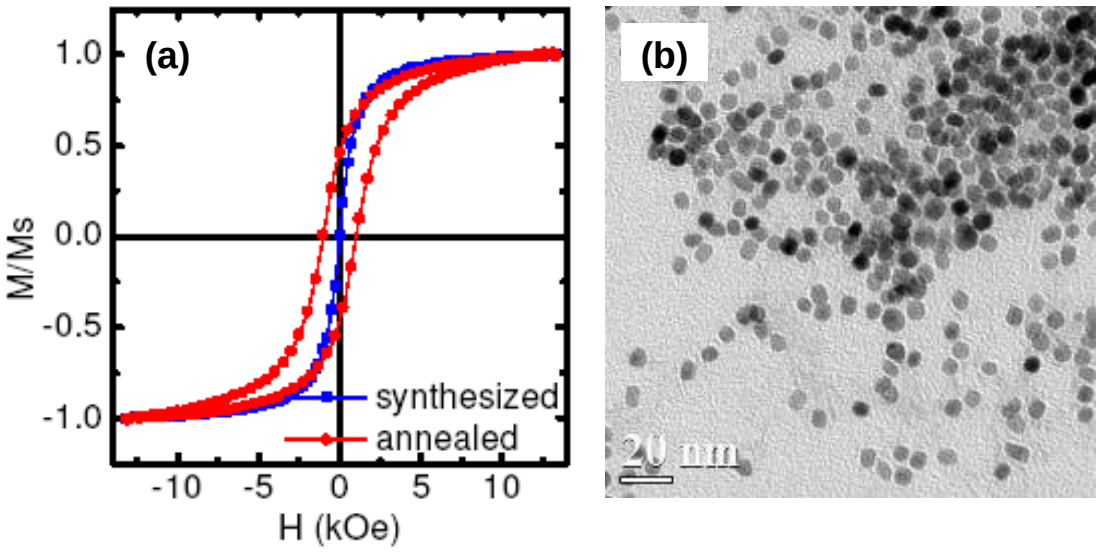

Figure 6.9 (a) Hysteresis loops of as-synthesized FePt/Au core/shell nanoparticles and annealed particles at 400 ºC for 1 h in forming gas. (b) TEM image of FePt/Au core/shell nanoparticles after annealing at 400 ºC for 1 h in forming gas.

6.3.3 Water Soluble FePt/Au Core/Shell Nanoparticles for Biomedical Applications

Water solubility of the nanoparticles is desired for bio-medical applications. The water solubility of the nanoparticles was achieved by replacing the capping ligands, oleic acid and oleyl amine, on the surface of FePt/Au core/shell particle with 11- mercaptoundecanoic acid. After the ligands exchange, the core/shell nanoparticles became water soluble since the outer hydrophilic group of the surfactant molecule dissolves the nanoparticles in water while –SH group attached on the Au shell and stabilize the nanoparticles. An outline of the ligands exchange leading to water solubility of nanoparticle is shown in Figure 6.10. Figure 6.11 shows the photograph of the FePt/Au core/shell nanoparticles dispersed in (A) hexane and (B) water.

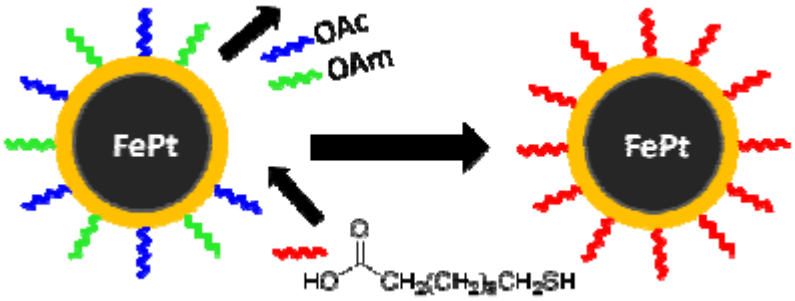

Figure 6.10 Schematic of preparation of water soluble FePt/Au core/shell nanoparticles.

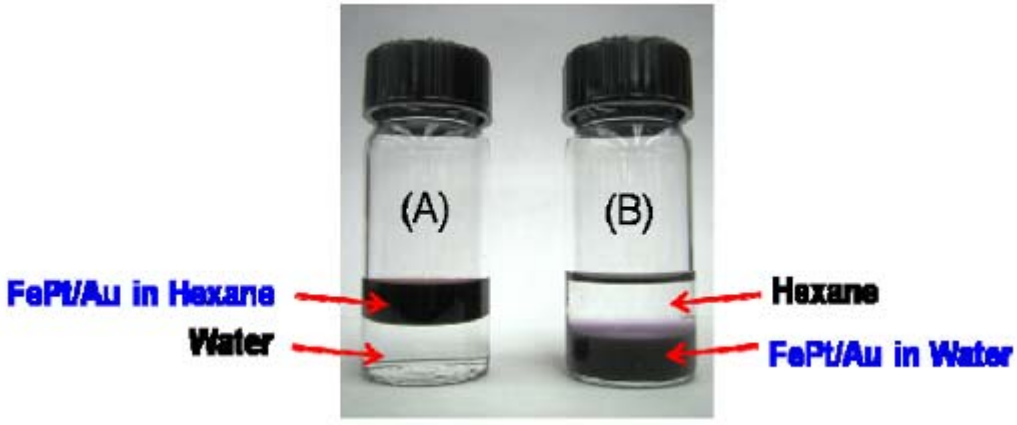

Figure 6.11 Photograph of the FePt/Au core/shell nanoparticles dispersed in (a) hexane and (b) water.

6.3.4 Micro-structural Analysis of FePtAu Nanoparticles

Figure 6.12 shows a TEM image of the as-synthesized $Fe_{42}Pt_{41}Au_{17}$ nanoparticles. The reason to choose this particular composition for FePtAu nanoparticles has been explained later in section 6.3.5.1. The TEM image reveals that the particles were of size 3.5 nm and monodisperse with a

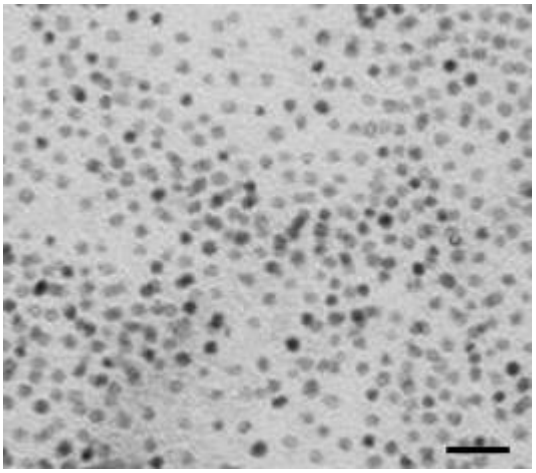

Figure 6.12 TEM image of as-synthesized $Fe_{42}Pt_{41}Au_{17}$ nanoparticles (the scale bar is for 20 nm).

narrow size distribution. Figure 6.13(a) shows the XRD patterns of as-synthesized $Fe_{51}Pt_{49}$ and $Fe_{42}Pt_{41}Au_{17}$ nanoparticles. The peak positions and intensity ratio of both samples match well with disordered fcc structure of FePt. However, It is seen that the (111) peak of $Fe_{42}Pt_{41}Au_{17}$ nanoparticles was shifted to low angle in comparison to $Fe_{51}Pt_{49}$ nanoparticles, indicating the lattice expansion of FePt nanoparticles after the addition of Au. The resulted lattice expansion of $Fe_{42}Pt_{41}Au_{17}$ nanoparticles was due to the larger atomic volume of Au (10.2 cm^3/mol) than that of Fe (7.1 cm^3/mol) and Pt (9.1 cm^3/mol).[167] The particle size calculated for $Fe_{42}Pt_{41}Au_{17}$ nanoparticles using Scherrer's formula[47] is consistent with the TEM image.

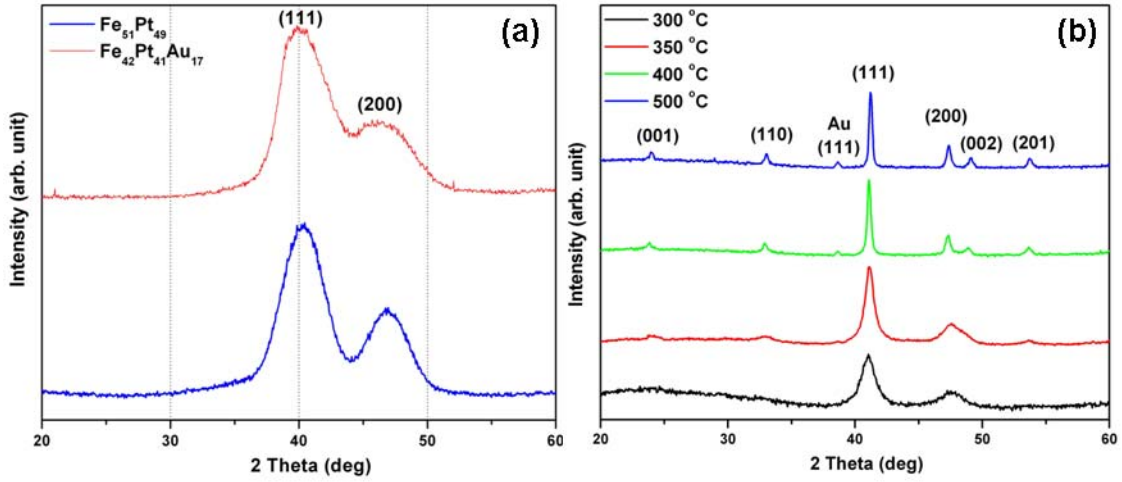

Figure 6.13 XRD patterns of (a) as-synthesized $Fe_{51}Pt_{49}$ and $Fe_{42}Pt_{41}Au_{17}$ nanoparticles (b) $Fe_{42}Pt_{41}Au_{17}$ nanoparticles after annealing at temperatures from 300 ^{o}C to 500 ^{o}C.

The disordered fcc $Fe_{42}Pt_{41}Au_{17}$ nanoparticles have low magnetocrystalline anisotropy, and hence were superparamagnetic at room temperature. To obtain high uniaxial magnetocrystalline anisotropy, $Fe_{42}Pt_{41}Au_{17}$ nanoparticles were annealed at temperatures between 300^{o}C to 500^{o}C. Figure 6.13(b) illustrates the XRD patterns of $Fe_{42}Pt_{41}Au_{17}$ nanoparticles annealed at different temperatures. Annealing induces the Fe and Pt atoms to rearrange into the long-range chemically ordered $L1_0$ phase. This phase transition from disordered fcc to ordered $L1_0$ depends on annealing temperature and can be seen as emergence of the superlattice (001) and (110) peaks and the shift of the (111) peak to high angle with increasing annealing temperature. Careful examination of the curves in Figure 6.13(b) shows that very weak peaks for the $L1_0$ FePt phase started appearing after heat treatment at 300 °C, indicating that partial ordering began around this temperature. This temperature, however, is more than 200 °C below that required for self-assembled FePt nanoparticles with no additive which indicates the transition temperature of fcc to $L1_0$ FePt phase decreased more than 200 °C due to the presence of Au.[71] It can be also seen that with

increasing annealing temperature, the intensity of the superlattice peaks became stronger; indicating that increase of annealing temperature favors the phase transition. The appearance of (111) peak of Au was also observed with increasing annealing temperature as reported previously.[164,167]

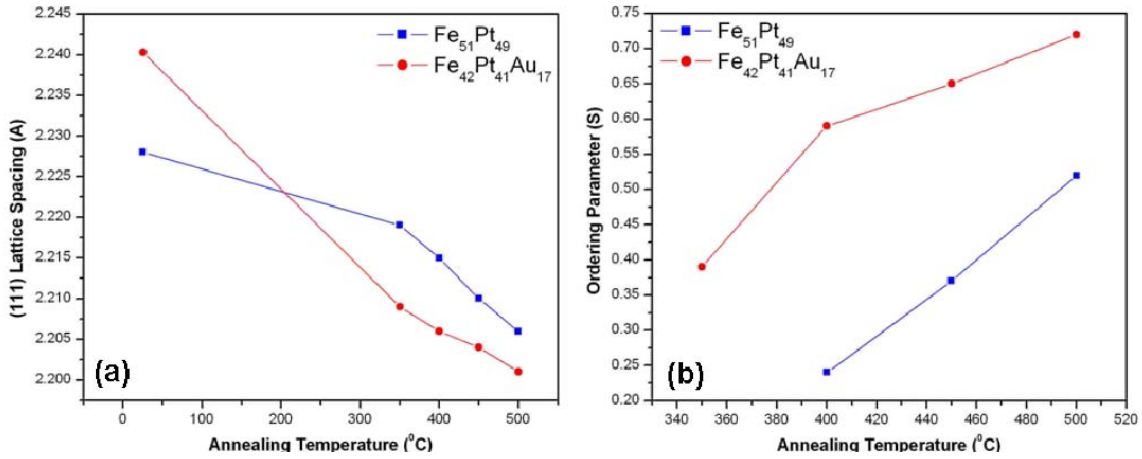

Figure 6.14 Dependence of (a) (111) Lattice spacing and (b) ordering parameter on annealing temperature for $Fe_{51}Pt_{49}$ and $Fe_{42}Pt_{41}Au_{17}$ nanoparticles.

The plots in Figure 6.14(a) compare values of the (111) lattice spacing for $Fe_{51}Pt_{49}$ and $Fe_{42}Pt_{41}Au_{17}$ nanoparticles as a function of annealing temperature. The lattice spacing for $Fe_{42}Pt_{41}Au_{17}$ nanoparticles approaches the bulk value for $L1_0$ FePt (d_{111} = 2.197 Å) at a lower annealing temperature after introducing gold, indicating the phase transition was promoted by the addition of gold. Figure 6.14(b) illustrates the ordering parameter as a function of annealing temperature for $Fe_{51}Pt_{49}$ and $Fe_{42}Pt_{41}Au_{17}$ nanoparticles. The ordering parameter (S) which is an indicator of percentage of ordered phase was calculated as

$$S = (I_{001}/ I_{002})^{0.85}$$

where I_{001} and I_{002} are intensities of peak (001) and (002), respectively in XRD patterns of annealed FePt and FePtAu nanoparticles. At each annealing temperature, the ordering parameter of the $Fe_{42}Pt_{41}Au_{17}$ nanoparticles is found larger than that of the $Fe_{51}Pt_{49}$

nanoparticles which also indicated that ordering in $Fe_{42}Pt_{41}Au_{17}$ nanoparticles was promoted due to the presence of gold.

6.3.5 Magnetic Properties of FePtAu Nanoparticles

6.3.5.1 Effect of Au Concentration

Table 6.1 Composition and magnetic properties of $Fe_xPt_yAu_{100-x-y}$ nanoparticles with increasing concentration of Au.

$Fe(CO)_5$ (mmol)	$Pt(acac)_2$ (mmol)	$Au(ac)_3$ (mmol)	Composition of $Fe_xPt_yAu_{100-x-y}$	Coercivity after annealing at 500 ^oC (kOe)	Saturation Magnetization after annealing at 500 ^oC (emu/g)
1.0	0.5	0.0	$Fe_{51}Pt_{49}$	2.0	50
1.0	0.5	0.1	$Fe_{46}Pt_{45}Au_9$	3.3	43
1.0	0.5	0.15	$Fe_{44}Pt_{43}Au_{13}$	6.9	38
1.0	0.5	0.2	$Fe_{42}Pt_{41}Au_{17}$	13	33
1.0	0.5	0.25	$Fe_{38}Pt_{37}Au_{25}$	7.5	27
1.0	0.5	0.3	$Fe_{35}Pt_{35}Au_{30}$	3.5	21

Table 6.1 shows the synthetic conditions of the Au-doped FePt nanoparticles. In the first series of experiments, the molar concentration of Fe and Pt precursors were kept constant while molar concentration of Au precursor was varied. Effort was made to control the atomic ratio of Fe to Pt close to unity in $Fe_xPt_yAu_{100-x-y}$ nanoparticles. The as-synthesized equi-atomic FePt nanoparticles with different atomic percent of Au additive were annealed at 500 ^oC and

their corresponding coercivity and saturation magnetization was measured. As shown in the table, initially the coercivity of $Fe_xPt_yAu_{100-x-y}$ nanoparticles increased with increasing concentration of Au and the maximum coercivity of 13 kOe was obtained for FePt nanoparticles having 17 atomic percent of Au. In comparison, pure $Fe_{51}Pt_{49}$ nanoparticles yielded only 2 kOe of coercivity when annealed at the same temperature. However, the coercivity of the $Fe_xPt_yAu_{100-x-y}$ nanoparticles was found to decrease when Au concentration was increased above 17 atomic percent. On the other hand, unlike the coercivity trend, the magnetization monotonously decreased with increase of Au content owing to the diamagnetic nature of Au. It is clearly seen from the table that, $Fe_{42}Pt_{41}Au_{17}$ nanoparticles have the highest coercivity, and hence was selected for detail micro-structural characterization as shown in section 6.3.4.

6.3.5.2 Effect of Fe Concentration

Table 6.2 Composition and magnetic properties of $Fe_xPt_yAu_{100-x-y}$ nanoparticles with increasing concentration of Fe.

$Fe(CO)_5$ (mmol)	$Pt(acac)_2$ (mmol)	$Au(ac)_3$ (mmol)	Composition of $Fe_xPt_yAu_{100-x-y}$	Coercivity after annealing at 500 ^oC (kOe)	Saturation Magnetization after annealing at 500 ^oC (emu/g)
1.0	0.5	0.2	$Fe_{42}Pt_{41}Au_{17}$	13	33
1.2	0.5	0.2	$Fe_{46}Pt_{39}Au_{15}$	14.8	39
1.4	0.5	0.2	$Fe_{51}Pt_{36}Au_{13}$	18	47
1.6	0.5	0.2	$Fe_{55}Pt_{33}Au_{12}$	15.5	53
1.8	0.5	0.2	$Fe_{60}Pt_{30}Au_{10}$	4.5	61

To complete the loss in saturation magnetization caused by Au doping, Fe concentration in $Fe_xPt_yAu_{100-x-y}$ nanoparticles was increased. Table 6.2 shows composition and magnetic properties of the samples in which the molar concentration of Pt and Au precursors were kept identical to that used to synthesize $Fe_{42}Pt_{41}Au_{17}$ nanoparticles (Table 6.1) while the molar concentration of Fe precursor was varied. As the amount of Fe precursor was increased in the synthesis, increase in ratio between Fe and Pt while decrease in Au content was observed in the composition of $Fe_xPt_yAu_{100-x-y}$ nanoparticles. The coercivity and saturation magnetization values given in Table 2 were obtained from $Fe_xPt_yAu_{100-x-y}$ nanoparticles annealed at 500 ^oC. As expected, the saturation of $Fe_xPt_yAu_{100-x-y}$ nanoparticles was increased with increasing amount of Fe in their composition. It was interesting to observe that along with the saturation magnetization, the coercivity of $Fe_xPt_yAu_{100-x-y}$ nanoparticles also increased with increasing concentration of Fe and maximum coercivity of 18 kOe was obtained from $Fe_{51}Pt_{36}Au_{13}$ nanoparticles. However, it is not clear how the increase in Fe-content enhanced the coercivity. Nevertheless, further increase of Fe concentration (above 51%) resulted in decrease of coercivity as shown in Table 6.2.

6.3.5.3 Effect of Annealing Temperature

Figure 6.13(a) shows the dependence of coercivity on annealing temperature of $Fe_{51}Pt_{49}$, $Fe_{44}Pt_{43}Au_{13}$ and $Fe_{51}Pt_{36}Au_{13}$ nanoparticles. Similar concentration of Au was chosen in both the Au-doped FePt nanoparticles for comparison. It is very clear from the figure 6.15(a) that the coercivity of FePt, $Fe_{44}Pt_{43}Au_{13}$ and $Fe_{51}Pt_{36}Au_{13}$ nanoparticles increases with increasing annealing temperature. It can also be seen from the Figure 6.15(a) that at the same annealing temperature, the coercivity of $Fe_{44}Pt_{43}Au_{13}$ nanoparticles was higher than $Fe_{51}Pt_{49}$ nanoparticles and was further increased by increasing Fe/Pt atomic ratio from 1 ($Fe_{44}Pt_{43}Au_{13}$) to 1.4 ($Fe_{51}Pt_{36}Au_{13}$) keeping atomic percent of Au constant. The coercivity of $Fe_{51}Pt_{36}Au_{13}$ nanoparticles after annealing at 300 ^oC was 2.6 kOe while the coercivity of $Fe_{51}Pt_{49}$ nanoparticles was negligible at this temperature. To achieve similar coercivity in $Fe_{51}Pt_{49}$

nanoparticles, the particles have to be annealed above 500 °C.[71] This is the second proof that for the $Fe_{51}Pt_{36}Au_{13}$ nanoparticles, the phase transition temperature from fcc to $L1_0$ structure was reduced by more than 200 °C.

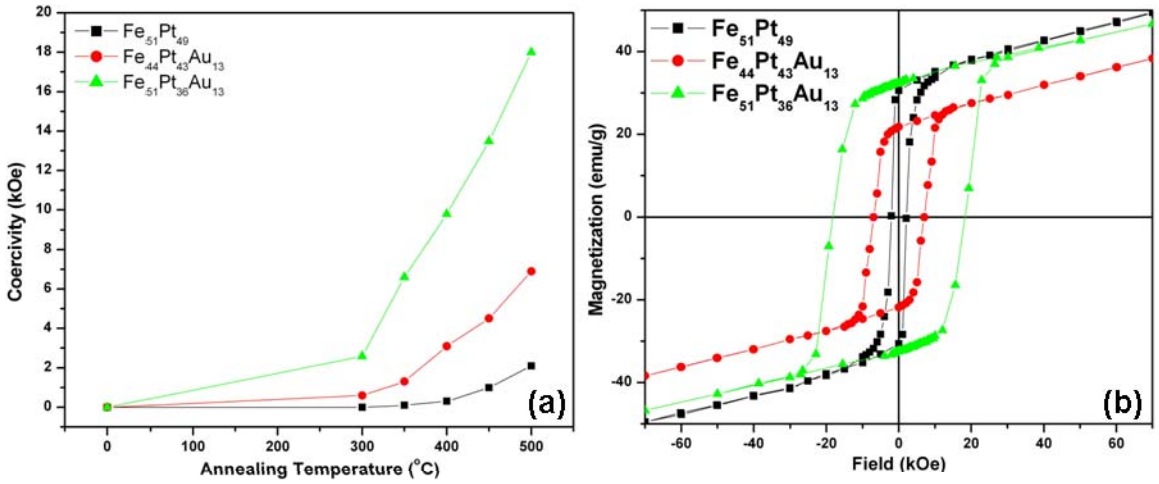

Figure 6.15(a) Coercivity dependence of $Fe_{51}Pt_{49}$, $Fe_{42}Pt_{41}Au_{17}$, and $Fe_{51}Pt_{36}Au_{13}$ nanoparticles on annealing temperature. (b) Hysteresis loops of $Fe_{51}Pt_{49}$, $Fe_{44}Pt_{43}Au_{13}$ and $Fe_{51}Pt_{36}Au_{13}$ nanoparticles after annealing at 500 °C for 1 hour in forming gas.

Figure 6.15(b) shows the hysteresis loops of $Fe_{51}Pt_{49}$, $Fe_{44}Pt_{43}Au_{13}$, and $Fe_{51}Pt_{36}Au_{13}$ nanoparticles after annealing at 500 °C for 1 h in forming gas. As shown in the figure, the coercivity of $Fe_{44}Pt_{43}Au_{13}$ nanoparticles is higher than that of $Fe_{51}Pt_{49}$ nanoparticles; however the saturation magnetization is lower. In comparison, the saturation magnetization of $Fe_{51}Pt_{36}Au_{13}$ nanoparticles was close to $Fe_{51}Pt_{49}$ nanoparticles while the coercivity was significantly higher than both $Fe_{44}Pt_{43}Au_{13}$ and $Fe_{51}Pt_{49}$ nanoparticles. These results clearly show that by tuning the stoichiometry of the $Fe_xPt_yAu_{100-x-y}$ nanoparticles, Au doping enhances the coercivity of FePt nanoparticles without sacrifice of saturation magnetization.

6.3.5.4 Real Effect of Doping

It has been reported previously[168] that addition of Au in FePt nanoparticles decreases the ordering temperature; however it promotes the grain growth during heat treatments due to the low surface energy of Au. Since grain growth of FePt nanoparticles during annealing also promotes the chemical ordering, it was not clear whether the decrease in ordering temperature was due to Au doping or due to the enhanced grain growth during annealing. Figure 6.16(a) shows the grain size of $Fe_{51}Pt_{49}$ and $Fe_{51}Pt_{36}Au_{13}$ nanoparticles as a function of annealing temperature. The grain size was calculated from the XRD curves of annealed nanoparticles using Scherrer's formula.[47] It can be seen that the grain size of $Fe_{51}Pt_{36}Au_{13}$ nanoparticles is larger than that of $Fe_{51}Pt_{49}$ nanoparticles at similar annealing temperatures which indicates that presence of Au promoted the grain growth in $Fe_{51}Pt_{36}Au_{13}$ nanoparticles. To study the true effect of Au doping on the phase transition, coercivity vs. grain size was plotted for $Fe_{51}Pt_{49}$ and $Fe_{51}Pt_{36}Au_{13}$ nanoparticles. It can be seen from the Figure 6.16(b) that the coercivity of $Fe_{51}Pt_{36}Au_{13}$ was found higher than that for $Fe_{51}Pt_{49}$ particles for similar grain size which suggested that even though Au promoted the grain growth, the decrease in ordering temperature in $Fe_{51}Pt_{36}Au_{13}$ nanoparticles was primarily due to the Au doping.

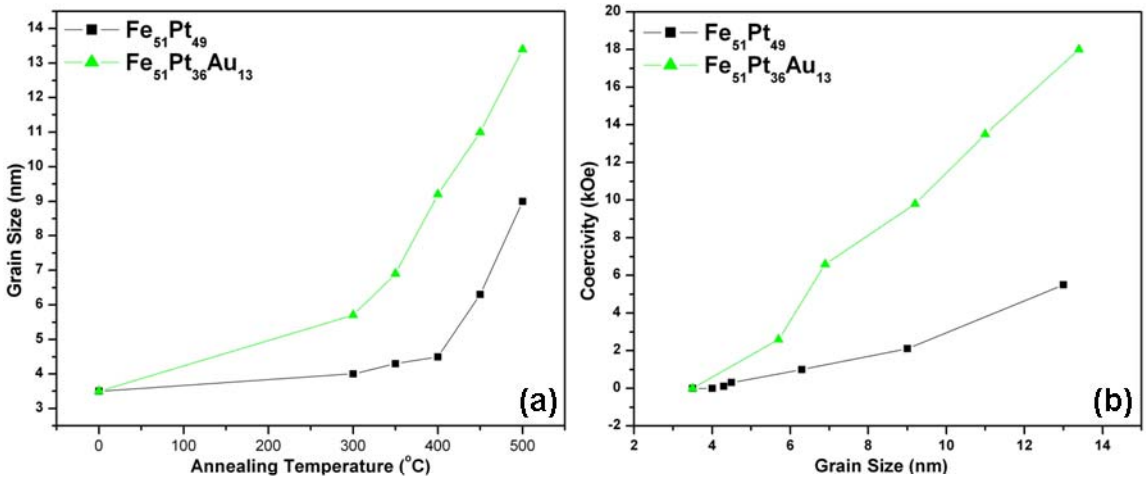

Figure 6.16(a) Grain size dependence of $Fe_{51}Pt_{49}$, $Fe_{42}Pt_{41}Au_{17}$, and $Fe_{51}Pt_{36}Au_{13}$ nanoparticles on annealing temperature. (b) Correlation of particle size and coercivity for $Fe_{51}Pt_{49}$, $Fe_{44}Pt_{43}Au_{13}$ and $Fe_{51}Pt_{36}Au_{13}$ nanoparticles.

6.4 Conclusion

FePt/Au core/shell nanoparticles have been successfully synthesized using seed mediated chemistry where FePt nanoparticles were used as seeds and Au shell was coated by reduction of gold acetate. The HRTEM with SAED and NBD analysis confirmed the core/shell structure of FePt/Au core/shell nanoparticles. The UV-Vis measurement revealed that FePt/Au core/shell nanoparticles show a red shift of surface plasmon absorption band compared to pure Au nanoparticles. The FePt/Au core/shell nanoparticles show ferromagnetism after annealing at optimum temperature. These FePt/Au core/shell nanoparticles can be further functionalized with DNA, protein and/or other bio-molecules and can serve as a potential nanoplatform for bio-labeling, magnetic separation and bio-sensors.

Also, $Fe_xPt_yAu_{100-x-y}$ nanoparticles have been prepared by polyol reduction of platinum acetylacetonate and gold acetate and thermal decomposition of iron pentacarbonyl. The as-synthesized nanoparticles have their size of 3.5 nm with disordered fcc structure. Upon annealing, the particles transform to ordered $L1_0$ structure with high magnetocrystalline anisotropy. After annealing the samples at 500 °C, the highest coercivity of 18 kOe was obtained from the $Fe_{51}Pt_{36}Au_{13}$ nanoparticles which is substantially higher compared to 2 kOe from $Fe_{51}Pt_{49}$ nanoparticles annealed at the same temperature. It is found that with right stoichiometry of the $Fe_xPt_yAu_{100-x-y}$ nanoparticles, the phase transition temperature can be reduced by more than 200 °C. The similar values of saturation magnetization of $Fe_{51}Pt_{36}Au_{13}$ and $Fe_{51}Pt_{49}$nanoparticles imply that Au doping enhances the coercivity without almost any sacrifice in saturation magnetization. The higher coercivity of $Fe_{51}Pt_{36}Au_{13}$ than that of $Fe_{51}Pt_{49}$ particles for similar grain size suggests that the increase in coercivity was primarily due to Au doping. These nanoparticles can be very useful in recording media since they can be converted from superparamagnetic to ferromagnetic at temperatures as low as 300 °C where almost no sintering occurs among nanoparticles.

CHAPTER 7

SUMMARY AND CONCLUSIONS

Monodisperse FePt nanoparticles with controlled size and geometry have drawn great attention in the last decade for fundamental scientific studies and for their potential applications in advanced materials and devices such as ultra-high-density magnetic recording media, exchange-coupled nanocomposite magnets, biomedicines and nanodevices. This dissertation focuses on the synthesis, characterization and their potential applications.

The FePt nanoparticles of different size (2 to 16 nm) and shape (spherical, cubic, rod) were synthesized by a simultaneous thermal decomposition of iron pentacarbonyl ($Fe(CO)_5$) and chemical reduction of platinum acetylacetonate ($Pt(acac)_2$) in presence of surfactants (oleic acid and oleyl amine). The size and shape of these particles were controlled by tuning surfactants and their concentration, type of solvents, nature of precursors, and heating rate. The as-synthesized FePt nanoparticles have chemically disordered fcc structure and are superparamagnetic at room temperature. Upon heat treatment the nanoparticles were transformed into ordered $L1_0$ structure, and high coercivity up to 27 kOe was achieved. Magnetic properties of the annealed FePt nanoparticles including magnetization and coercivity were strongly dependent on particle size, shape, composition and annealing temperature.

$FePt/Fe_3O_4$ bimagnetic nanoparticles with two different morphologies, core/shell and heterodimer have been prepared in a one or two-step synthesis. The morphology of the nanoparticles was controlled by changing solvent in the synthesis. Size of the FePt particles was tuned from 4 to 8 nm and the size of Fe_3O_4 was tuned from 1 to 3 nm in the core/shell particles and 5 to 10 nm in the heterodimers. After being annealed in a reducing atmosphere, the $FePt/Fe_3O_4$ nanoparticles form a hard magnetic nanocomposite films with enhanced

magnetic properties, which are closely related to dimensions of the soft and hard phase components and their morphology. The heterodimer nanoparticles resulted in relatively poor magnetic properties compared to the core/shell nanoparticles due to insufficient exchange coupling. By optimizing the dimensions of the FePt (8nm) and Fe_3O_4 (2nm) in core/shell bimagnetic nanoparticles, energy product up to 17.8 MGOe has been achieved.

8nm/2nm FePt/Fe_3O_4 core/shell and 8nm FePt + 4nm Fe_3O_4 mixed nanoparticles with similar magnetic properties were compacted under 2.0 GPa at 400 °C, 500 °C and 600 °C. A density up to 84% of the full density was achieved. The fcc FePt phase was changed to $L1_2$ FePt phase during the compaction while Fe_3O_4 phase still existed. After annealing at 650 °C in forming gas, the FePt/Fe_3O_4 compacted samples were converted into $L1_0$ FePt/Fe_3Pt magnetic nanocomposites. The nanoscale morphology was retained before and after annealing for both core/shell and mixed nanoparticles bulk samples. After annealing, the highest energy product in the bulk samples was 18.1 MGOe based on the theoretical density which is 39.2% higher than the theoretical limit of 13 MGOe for the single phase isotropic FePt magnets. It was found that the bulk samples made from core/shell nanoparticles compacted samples had more effective exchange coupling and hence higher energy products than the samples made from mixed nanoparticles.

FePt/Au core/shell nanoparticles were successfully synthesized using seed mediated chemistry where FePt nanoparitcles were used as seeds and Au shell was coated by reduction of gold acetate. The HRTEM with SAED, NBD analyses, UV-Vis measurement confirmed the presence of Au shell on surface of FePt nanoparticles. The as-synthesized FePt/Au core/shell nanoparticles were superparamagnetic and converted to ferromagnetic after annealing at 400 ºC in forming gas without any significant sintering. FePt/Au particles were dispersed in water to make them usable for biomedical applications.

FePtAu nanoparticles were prepared by doping Au into FePt nanoparticles during the synthesis. The as-synthesized FePtAu nanoparticles had disordered fcc structure and their size

was 3.5 nm. Upon annealing, the particles transformed to ordered $L1_0$ structure. It is found that with right stoichiometry of the $Fe_xPt_yAu_{100-x-y}$ nanoparticles, the phase transition temperature was reduced by more than 200 °C. After annealing at 500 °C, the highest coercivity of 18 kOe was obtained from the $Fe_{51}Pt_{36}Au_{13}$ nanoparticles which was substantially higher compared to 2 kOe from $Fe_{51}Pt_{49}$ nanoparticles annealed at the same temperature. The similar values of saturation magnetization of $Fe_{51}Pt_{36}Au_{13}$ and $Fe_{51}Pt_{49}$nanoparticles indicated that the increase in coercivity was made without sacrifice in saturation magnetization.

APPENDIX A

INTRINSIC PROPERTIES OF SELECTED MAGNETIC MATERIALS

Table A.1 Intrinsic properties of selected magnetic materials.[169]

Material	$\mu_o M_s$ (T)	T_c (K)	K_1 (MJ/m^3)	Symmetry
Fe_3O_4	0.60	858	-0.011	Cubic
$CoFe_2O_4$	0.50	793	0.270	Cubic
$NiFe_2O_4$	0.34	858	-0.0069	Cubic
□-Fe_2O_3	0.47	863	-0.0046	Cubic
CoPt	1.00	840	4.9	Tetragonal
FePt	1.43	750	6.6	Tetragonal
Sm_2Fe_{17}	1.17	389	-0.8	Rhombohedral
Sm_2Co_{17}	1.20	1190	3.3	Rhombohedral

APPENDIX B

CONVERSION FACTORS FOR COMMON MAGNETIC TERMS IN CGS AND SI UNITS

Table B.1 Conversion factors for common magnetic terms in CGS and SI units.[59]

UNITS FOR MAGNETIC PROPERTIES

Quantity	Symbol	Gaussian & cgs emu [a]	Conversion factor, C [b]	SI & rationalized mks [c]
Magnetic flux density, magnetic induction	B	gauss (G) [d]	10^{-4}	tesla (T), Wb/m^2
Magnetic flux	Φ	maxwell (Mx), $G \cdot cm^2$	10^{-8}	weber (Wb), volt second (V·s)
Magnetic potential difference, magnetomotive force	U, F	gilbert (Gb)	$10/4\pi$	ampere (A)
Magnetic field strength, magnetizing force	H	oersted (Oe),[e] Gb/cm	$10^3/4\pi$	A/m [f]
(Volume) magnetization [g]	M	emu/cm^3 [h]	10^3	A/m
(Volume) magnetization	$4\pi M$	G	$10^3/4\pi$	A/m
Magnetic polarization, intensity of magnetization	J, I	emu/cm^3	$4\pi \times 10^{-4}$	T, Wb/m^2 [i]
(Mass) magnetization	σ, M	emu/g	1 $4\pi \times 10^{-7}$	$A \cdot m^2/kg$ Wb·m/kg
Magnetic moment	m	emu, erg/G	10^{-3}	$A \cdot m^2$, joule per tesla (J/T)
Magnetic dipole moment	j	emu, erg/G	$4\pi \times 10^{-10}$	Wb·m [i]
(Volume) susceptibility	χ, κ	dimensionless, emu/cm^3	4π $(4\pi)^2 \times 10^{-7}$	dimensionless henry per meter (H/m), Wb/(A·m)
(Mass) susceptibility	χ_ρ, κ_ρ	cm^3/g, emu/g	$4\pi \times 10^{-3}$ $(4\pi)^2 \times 10^{-10}$	m^3/kg $H \cdot m^2/kg$
(Molar) susceptibility	χ_{mol}, κ_{mol}	cm^3/mol, emu/mol	$4\pi \times 10^{-6}$ $(4\pi)^2 \times 10^{-13}$	m^3/mol $H \cdot m^2/mol$
Permeability	μ	dimensionless	$4\pi \times 10^{-7}$	H/m, Wb/(A·m)
Relative permeability [j]	μ_r	not defined		dimensionless
(Volume) energy density, energy product [k]	W	erg/cm^3	10^{-1}	J/m^3
Demagnetization factor	D, N	dimensionless	$1/4\pi$	dimensionless

a. Gaussian units and cgs emu are the same for magnetic properties. The defining relation is $B = H + 4\pi M$.
b. Multiply a number in Gaussian units by C to convert it to SI (e.g., $1\ G \times 10^{-4}\ T/G = 10^{-4}\ T$).
c. SI (*Système International d'Unités*) has been adopted by the National Bureau of Standards. Where two conversion factors are given, the upper one is recognized under, or consistent with, SI and is based on the definition $B = \mu_0(H + M)$, where $\mu_0 = 4\pi \times 10^{-7}$ H/m. The lower one is not recognized under SI and is based on the definition $B = \mu_0 H + J$, where the symbol I is often used in place of J.
d. 1 gauss = 10^5 gamma (γ).
e. Both oersted and gauss are expressed as $cm^{-1/2} \cdot g^{1/2} \cdot s^{-1}$ in terms of base units.
f. A/m was often expressed as "ampere-turn per meter" when used for magnetic field strength.
g. Magnetic moment per unit volume.
h. The designation "emu" is not a unit.
i. Recognized under SI, even though based on the definition $B = \mu_0 H + J$. See footnote c.
j. $\mu_r = \mu/\mu_0 = 1 + \chi$, all in SI. μ_r is equal to Gaussian μ.
k. $B \cdot H$ and $\mu_0 M \cdot H$ have SI units J/m^3; $M \cdot H$ and $B \cdot H/4\pi$ have Gaussian units erg/cm^3.

R. B. Goldfarb and F. R. Fickett, U.S. Department of Commerce, National Bureau of Standards, Boulder, Colorado 80303, March 1985
NBS Special Publication 696 For sale by the Superintendent of Documents, U.S. Government Printing Office, Washington, DC 20402

APPENDIX C

CRYSTRAL STRUCTURE OF FERRITE

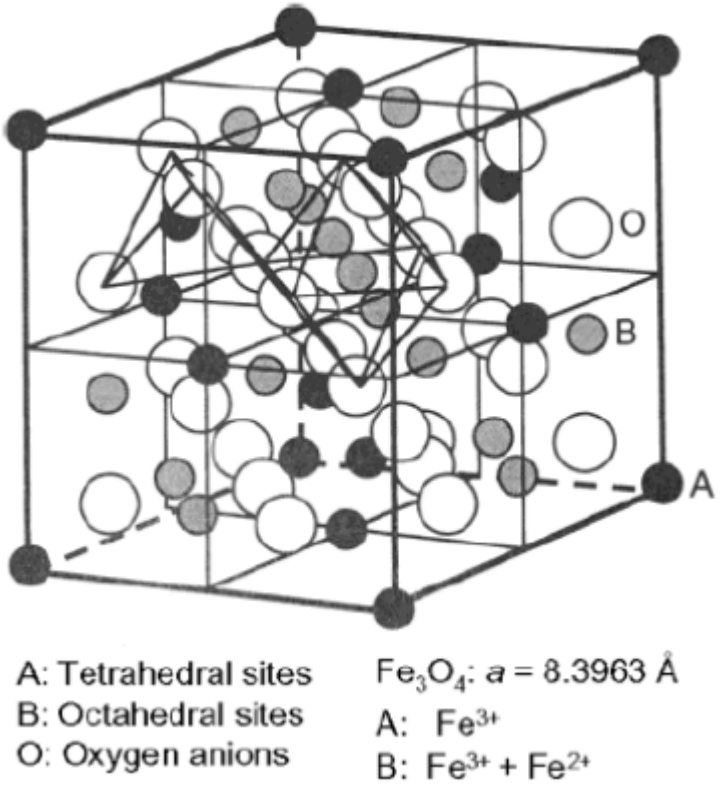

Figure C.1 Schematic model of the spinel unite cell structure.[170] The spinel structure has two cation sites: the tetrahedrally coordinated A sites and the octahedrally coordinated B sites. For Fe_3O_4, the A and B positions are occupied by Fe^{3+} and Fe^{2+} cations, respectively.

APPENDIX D

PHASE DIAGRAM OF FePt

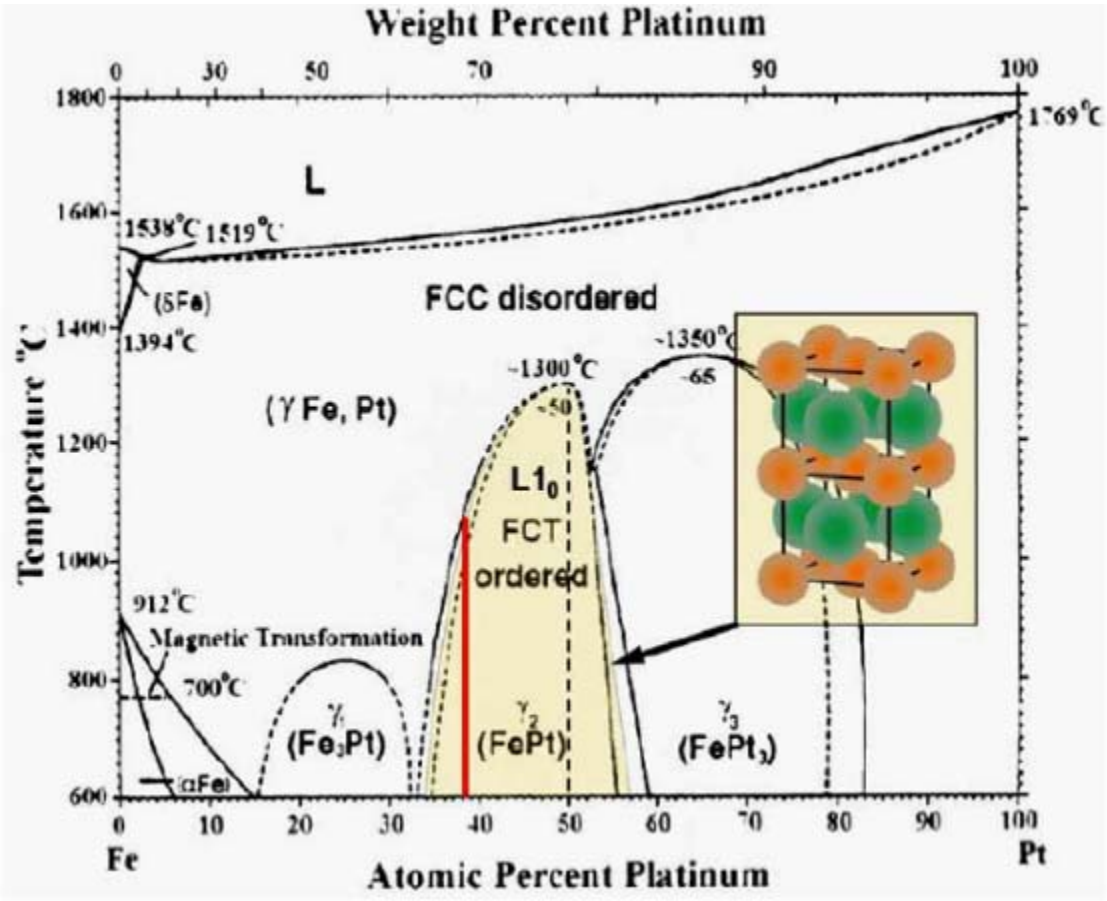

Figure D.1 FePt phase diagram and schematic representation of structure transformation between fcc and $L1_0$ FePt. Orange circles represent Fe atoms and green circles represent Pt atoms in unit cells.[171]

APPENDIX E

PROPERTIES OF HARD MAGNETIC MATERIALS

Table E.1 Properties of hard magnetic materials.[51]

- anisotropy field: $H_K = 2K_u/M_S$;
- domain wall width: $\delta_W = \pi (A/K_u)^{1/2}$
- domain wall energy: $\gamma_W \cong 4 (A \cdot K_u)^{1/2}$
- single particle domain size: $D_C = 1.4\ \gamma_W / M_S^2$
- exchange coupling constant $A=10^{-6}$ erg/cm
- minimal stable grain size: $D_p = (60\ k_B T/K_u)^{1/3}$ (τ=10 years)

alloy system	material	K_u (10^7erg/cm^3)	M_S (emu/cm^3)	H_K (kOe)	T_C(K)	δ_W (Å)	γ (erg/cm^3)	D_C (μm)	D_p (nm)
	CoPtCr	0.20	298	13.7	--	222	5.7	.89	10.4
Co-alloys	Co	0.45	1400	6.4	1404	148	8.5	.06	8.0
	Co_3Pt	2.0	1100	36	--	70	18	.21	4.8
	FePd	1.8	1100	33	760	75	17	.20	5.0
$L1_0$	FePt	6.6-10	1140	116	750	39	32	.34	3.3-2.8
phases	CoPt	4.9	800	123	840	45	28	.61	3.6
	MnAl	1.7	560	69	650	77	16	.71	5.1
rare-earth	$Fe_{14}Nd_2B$	4.6	1270	73	585	46	27	.23	3.7
transition metals	$SmCo_5$	11-20	910	240-400	1000	22-30	42-57	.71-.96	2.7-2.2

APPENDIX F

RESEARCH ACCOMPLISHMENTS

Awards

Second Place in ASM North Texas Materials Symposium 2005 at Arlington, Tx.

News Published for Research Involved

- Magnets warm up to get stronger, published in *nanotechweb.org* ,August 29, 2007
- Just Add Salt titled news articles published in Physics Web in August 4, 2005.
  Link to the articles: *http://physicsweb.org/articles/news/9/8/3/1*
- For nanoparticles, just add salt titled news articles published in Nanotechweb.org
  Link to the articles: http://www.nanotechweb.org/articles/news/4/8/6/1
- Physicists Discover Table Salt is Solution to Creating the Smallest Magnets titled news articles published in UTA Today in August 15, 2005.

Publications

1. V. Nandwana, G. S. Chaubey, Y. Zhang, and J. P. Liu, Magnetic properties of $Fe_xPt_yAu_{100-x-y}$ nanoparticles (Submitted to *J Nanosc. Nanotech.*).
2. V. Nandwana, G. S. Chaubey, K. Yano, C. B. Rong and J. P. Liu, Bimagnetic nanoparticles with enhanced exchange coupling and energy products, *J. Appl. Phys. J. Appl. Phys.* 105 (2009) 014303 *(selected for the January 2009 issue of Virtual Journal of Nanoscale Science & Technology)*.
3. V. Nandwana, K. E. Elkins, N. Poudyal, G. S. Chaubey, K. Yano, and J. P. Liu, Size and shape control of monodisperse FePt nanoparticles *J. Phys. & Chem. C,* 111 (2007) 4185-4189.
4. V. Nandwana, K. E. Elkins, and J. P. Liu, Magnetic hardening in ultrafine FePt nanoparticle assembled films, *Nanotechnology* 16 (2005) 2823–2826.

5. K. Yano, V. Nandwana, G. S. Chaubey, N. Poudyal, S. Kang, and J. P. Liu, Synthesis and characterization of magnetic FePt/Au core/shell nanoparticles, *J. Phys. & Chem. C* (in press).
6. C. B. Rong, V. Nandwana, N. Poudyal, G. S. Chaubey, and J. P. Liu, Phase transformation and magnetic hardening in isolated FePt nanoparticles, *IEEE Trans. on Nanotech.* (in press).
7. N. Poudyal, G. S. Chaubey, V. Nandwana, C. Rong, K. Yano, and J. P. Liu, Synthesis of FePt nanorods and nanowires by a facile method, *Nanotechnology*, 19 (2008) 355601.
8. K. Yano, V. Nandwana, N. Poudyal, C. Rong, and J. P. Liu, Rapid thermal annealing of FePt nanoparticles, *J. Applied Physics,* 104 (2008), 013918.
9. C. B. Rong, N. Poudyal, G. S. Chaubey, V. Nandwana, Y. Liu, Y. Q. Wu, M. J. Kramer, M. E. Kozlov, R. H. Baughman, and J. P. Liu, High thermal stability of carbon-coated $L1_0$-FePt nanoparticles prepared by salt-matrix annealing, *J. Appl. Phys*. 103 (2008) 07E131.
10. G. S. Chaubey, V. Nandwana, N. Poudyal, C. Rong, and J. P. Liu, Synthesis and characterization of bimagnetic bricklike nanoparticles, *Chem. Mater.*, 20 (2008) 475–478.
11. K. E. Elkins, G. S. Chaubey, V. Nandwana, and J. P. Liu, A novel approach to synthesis of FePt magnetic nanoparticles, *J. Nano Research,* 1 (2008) 23-29.
12. C. B. Rong, N. Poudyal, G. S. Chaubey, V. Nandwana, R. Skomski, Y. Q. Wu, and M. J. Kramer, Structural phase transition and ferromagnetism in monodisperse 3 nm FePt particles, *J. Appl. Phys.,* 102 (2007) 043913.
13. C. B. Rong, V. Nandwana, N. Poudyal, J. P. Liu, M. E. Kozlov, R. H. Baughman, Y. Ding, and Z. L. Wang, Bulk FePt based nanocomposite magnets with enhanced exchange coupling, *J. Appl. Phys*. 102 (2007) 023908.

14. S. Kang, S. Shi, Z. Jia, G. B. Thompson, D. E. Nikles, J. W. Harrell, D. Li, N. Poudyal, V. Nandwana, and J. P. Liu, Microstructures and magnetic alignment of $L1_0$ FePt nanoparticles, *J. Appl. Phys.*, 101 (2007) 09J113.
15. C. B. Rong, V. Nandwana, N. Poudyal, J. P. Liu, T. Saito, Y. Wu, and M. J. Kramer, Bulk FePt/Fe_3Pt nanocomposite magnets prepared by spark plasma sintering, *J. Appl. Phys.*, 101 (2007) 09K515.
16. C. B. Rong, V. Nandwana, N. Poudyal, Y. Li, J. P. Liu, Y. Ding, and Z. L. Wang, Formation of Fe_3Pt phase in FePt-based nanocomposite magnets, *J. Phys. D: Appl. Phys.* 40 (2007) 712–716.
17. C. B. Rong, Daren Li, V. Nandwana, N. Poudyal, Y. Ding, Z. L. Wang, H. Zeng, and J. P. Liu, Size-dependent chemical and magnetic ordering in $L1_0$ FePt nanoparticles, *Adv. Materials* 18 (2006) 2984–2988.
18. J. P. Liu, K. E. Elkins, D. Li, V. Nandwana, and N. Poudyal, Phase transformation of FePt nanoparticles, *IEEE Trans. Magn.* 42 (2006) 3036-3041.
19. D. Li, N. Poudyal, V. Nandwana, Z. Jin, K. Elkins, and J. P. Liu, Hard magnetic FePt nanoparticles by salt-matrix annealing, *J. Appl. Phys.* 99 (2006) 08E911.
20. K. E. Elkins, D. Li, N. Poudyal, V. Nandwana, Z. Jin, K. Chen, and J. P. Liu, Monodisperse face-centered tetragonal FePt nanoparticles with giant coercivity, *J. Phys D: Appl. Phys.* 38 (2005) 2306-2309 (*an IoP Select article and reported in PhysicsWorld, NanotechWeb and other medias*).

Conference Presentations

1. V. Nandwana, G. S. Chaubey, Y. Zhang, and J. P. Liu, Magnetic properties of $Fe_xPt_yAu_{100-x-y}$ nanoparticles, 53rd MMM Conference, November 10-14, 2008, Austin, TX.

2. V. Nandwana, K. Yano and J. P. Liu, Synthesis and characterization of FePt/Fe_3O_4 bimagnetic nanoparticles, MRS Fall 2007 Meeting, November 25-30, Boston, MA.

3. V. Nandwana, G. S. Chaubey, K. Yano, J. P. Liu, Synthesis and characterization of hard/soft bimagnetic nanoparticles, APS March Meeting 2007, March 5–9, Denver, CO.

4. V. Nandwana, G. S. Chaubey, K. Yano, J. P. Liu, Synthesis and characterization of bimagnetic core-shell nanoparticles, APS Fall Meeting 2006, October 5–7, 2006, Arlington, TX.

5. V. nandwana and J. P. Liu, Chemical synthesis of FePt nanoparticles, ASM-International North Texas Materials Symposium, April 10, 2005, Arlington, TX.

6. V. Nandwana and J.P. Liu, High coercivity in FePt nanoparticle assemblies, APS March Meeting 2005, March 23, Los Angeles, CA.

7. C. B. Rong, V. Nandwana, N. Poudyal, G. S. Chaubey, and J. P. Liu, Magnetic hardening in isolated FePt nanoparticles, The 8th International Conference on Nanotechnology, IEEE Nano Conference, August 19 - 21, 2008 Arlington, TX.

8. N. Poudyal, V. Nandwana, C. B. Rong, G. S. Chaubey and J.P. Liu, $L1_0$ FePt Nanoparticles by Salt-matrix Annealing, IEEE Magnetics Society Summer School, University of Colorado at Colorado Springs, August. 3-8, 2008, Colorado Springs, CO.

9. K. Yano, V. Nandwana, N. Poudyal, C. B. Rong and J. P. Liu, Rapid Thermal Annealing of Monodisperse FePt Nanoparticles, MRS Fall 2007 Meeting, November 25 - 30, Boston, MA.

10. G. S. Chaubey, Y. Wang, C. B. Rong, N. Poudyal, V. Nandwana, K. E. Elkin and J. P. Liu, Silica Encapsulation and Magnetic Properties of Hard Magnetic Sm2Co17

Nanoparticles Obtained by Mechanical Ball-milling Process, MRS Fall 2007 Meeting, November 25 - 30, Boston, MA.

11. C. B. Rong, Y. Wang, V. Nandwana and J. P. Liu, Bulk SmCo5/α-Fe Nanocomposite Magnets Prepared by Warm Compaction of Mechanically Milled Powders, MRS Fall 2007 Meeting, November 25 - 30, Boston, MA.

12. N. Poudyal, G. S. Chaubey, V. Nandwana and J. P. Liu, Synthesis and Characterization of FePt Nanorods and Nanowires, 52nd MMM Conference, November 5-9 , 2007, Tampa, FL.

13. C. B. Rong, N. Poudyal, G. S. Chaubey, V. Nandwana, Y. Liu, Y. Wu, M. Kramer, M. Kozlov, R. Baughman and J. P. Liu, High thermal stability of carbon-coated $L1_0$-FePt nanoparticles prepared by salt-matrix annealing, 52nd MMM Conference, November 5-9 , 2007,Tampa, FL.

14. K. Yano, V. Nandwana, N. Poudyal, G. S. Chaubey and J.P. Liu, Chemical synthesis of FePt/Au core/shell nanoparticles, 52nd MMM Conference, November 5-9, 2007, Tampa, FL.

15. C. B., Rong, V. Nandwana, J. P. Liu, Bulk nanocomposite magnets with enhanced exchange coupling, APS March Meeting 2007, March 5–9, 2007; Denver, CO.

16. C. B. Rong, V. Nandwana, N. Poudyal and J. P. Liu, Bulk FePt/Fe3Pt nanocomposite magnets prepared by spark plasma sintering, 10th joint MMM/InterMag Conference, Jan 7-11, 2007, Baltimore, MD.

17. C. B. Rong, V. Nandwana and J. P. Liu, Inter-particle Magnetic Interactions in Nanoparticle Compacts, MRS Fall Meeting 2006, November 29, 2006, Boston.

18. J. P. Liu, K. E. Elkins, D. Li, V. Nandwana, N. Poudyal, Phase Transformation of FePt Nanoparticles, InterMag Congerence, 2006 May 8-12, San Diego, CA.

19. D. Li, N. Poudyal, V. Nandwana and J.P. Liu, Size effect on chemical ordering in face-centered tetragonal FePt nanoparticles, APS March Meeting 2006, March 17, Baltimore, MD.

20. D. Li, N. Poudyal, V. Nandwana, Z. Jin, K. E. Elkins and J. P. Liu, Hard Magnetic FePt Nanoparticles by salt matrix annealing, 50th Conference on Magnetism and Magnetic Materials, San Jose, California, October 30-November 3, 2006, San Jose, CA.

REFERENCES

1. S. Chikasumi, Physics of Magnetism, John Wiley and Sons (1964).
2. B. D. Cullity, Introduction to Magnetic Materials, Addison-Wesley Publishing (1972).
3. Nicola A. Spaldn, Magnetic Materials: Fundamentals and Device Applications, Cambridge University Press (2003).
4. William D. Callister, Jr., Material Science and Engineering: An Introduction, John Wiley & Sons (2000).
5. Robert C. O‘ Handley, Modern Magnetic Materials: Principles and Applications, Wiley & Sons (2000).
6. J.C. Anderson, Magnetism and Magnetic Materials, Chapman and Hall Ltd. (1968).
7. R. Skomski and J.M.D. Coey, Physical. Review B, 48, 15812 (1993).
8. http://www.aacg.bham.ac.uk/magnetic_materials.
9. J. M. D. Coey, Solid State Communications, 102, 101 (1997).
10. http://www.magnets.bham.ac.uk/magnetic_materials.
11. D.C. Jiles, Acta Meterialia, 15, 5907 (2003).
12. E. F. Kneller and R. Hawing, IEEE Transactions on Magnetics, 27, 3588 (1991).
13. J. P. Liu, 18th International workshop on high performance magnets and their applications, Annecy (France) (2004).
14. J. P. Liu, Nanosturctured Soft and Hard Magnetic Materials, Kluwer Academic/Plenum Publishers and Tsinghua University Press (2003).
15. J. Sort, S. Surmach, J. S. Munoz, and M. D. Baro, Physical Review B, 65, 174420 (2002).

16. R. Coehoorn, D. B. de Mooij and C. de Waard, Journal of Magnetism and Magnetic Material, Volume 80, 10 (1989).
17. R. Skomski and J.M.D. Coey, Physical Review B, 48, 15812(1993).
18. E. E. Fullerton, J. S. Jiang and S. D. Bader, Journal of Magnetism and Magnetic Materials, 0, 392 (1999).
19. R. Skomski and J.M.D Coey, IEEE Transactions on Magnetics, 30, 607 (1994).
20. J. M. D. Coey, Journal of Alloys and Compounds, 326, 2 (2000).
21. H. Zeng, J. Li, J.P. Liu, Z. L. Wang, and S. Sun, Nature, 420, 395 (2002).
22. D. Jales, Introduction to Magnetism and Magnetic Materials; CRC Press (1998).
23. M. P. Morales, S. Veintemillas-Verdaguer, M. I. Montero, C. J. Serna, Chem. Mater. 11, 3058 (1999).
24. M. P. Morales, C. J. Serna, F. Bødker, S. Mørup, J. Phys.: Condens. Matter 9, 5461 (1997).
25. Y. Jun, J. Seo, and J. Cheon, Account, 41,179 (2008).
26. S. P. Gubin and Y. A. Koksharov, Neorg. Mater., 38, 1287 (2002).
27. D. M. Cox, D. J. Tevor, R. L. Whetten, E. A. Rohlfing, A. Kaldor, Phys. Rev. B, 32, 7290 (1985).
28. W. A. de Heer, P. Milani and A. Chatelain, Phys. Rev. Lett., 65, 488 (1990).
29. Y. I. Petrov, E. A. Shafranovskii, Y. F. Krupyanskii and S. V. Esin, Dokl. Akad. Nauk, 379, 357 (2001).
30. X. G. Li, A. Chiba, S. Takahashi and K. Ohsaki, J. Magn. Magn. Mater., 173, 101 (1997).
31. F. Fendrych, L. Kraus, O. Chayka, P. Lobotka, I. Vavra, J. Tous, V. Studnicka and Z. Frait, Monatsh. Chem., 133, 773 (2002).
32. B. Martinez, A. Roig, X. Obradors and E. Molins, J. Appl. Phys., 79, 2580 (1996).
33. Y. I. Petrov and E. A. Shafranovskii, Izv. Akad. Nauk, Ser. Fiz., 64, 1548 (2000).

34. V. A. Kuznetsov, A. G. Lipson and D. M. Sakov, Zh. Fiz. Khim., 67, 782 (1993).

35. C Suryanarayana, Prog. Mater. Sci., 46, 1 (2001).

36. J. A. Becker, R. Schafer, J. R. Festag, J. H. Wendorff, F. Hensel, J. Pebler, S. A. Quaiser,W. Helbug and M. T. Reetz, Surf. Rev. Lett., 3, 1121 (1996).

37. C. Pascal, J. L. Pascal, F. Favier, M. L. E. Moubtassim and C. Payen, Chem. Mater., 11, 141 (1999).

38. T. Hyeon, S. S. Lee, J. Park, Y. Chung and H. B. Na, J. Am. Chem. Soc., 123, 12798 (2001).

39. A. D. Pomogailo, A. S. Rozenberg and I. E. Uflyand, Metal Nanoparticles in Polymers, Khimiya (2000).

40. T. Prozorov, G. Kataby, R. Prozorov and A. Gedanken. Thin Solid Films, 340,189 (1999).

41. C. B. Murray, S. Sun, W. Gaschler, H. Doyle, T. A. Betley and C. R. Kagan, IBM J. Res. Dev., 45, 47 (2001).

42. C. B. Murray, S. Sun, H. Doyle and T. A. Betley MRS Bull., 26, 985 (2001).

43. C. Petit and M. P. Pileni, Appl. Surf. Sci., 162, 519 (2000).

44. M. P. Pileni, Langmuir, 13, 3266 (1997).

45. D. R. Uhlmann, G. Teowee and J. Boulton, J. Sol-Gel Sci. Technol., 8, 1083 (1997)

46. P. Bose, S. Bid, S. K. Pradhan, M. Pal and D. Chakravorty, J. Alloys Compd., 343, 192 (2002).

47. B. D. Cullity and S. R. Stock, Elements of X-ray diffraction, Prentice Hall, 170.

48. Brent Fultz and Jame M Howe, Transmission Electron Microscopy and Diffractometry of Materials, third edition, Springer Berlin Heilberg (2008).

49. http://www.microscopy.ethz.ch.

50. D. Weller and A. Moser, IEEE Transactions on Magnetics, 35, 4423 (1999).

51. D. Weller, A. Moser, L. Folks, M. E. Best, W. Lee, M. F. Toney, M. Schwckert, J. U. Thiele and M. F. Doerner, IEEE Transactions on Magnetics, 36, 10 (2000).

52. M. A. Willard, L.K. Kulrihara, E.E. Carpenter, S. Calvin and V.G. Harris, International Material Reviews, 49, 3 (2004).

53. T. Hyeon, Chemical communication, 8, 927 (2003).

54. C. C. Berry and A. S. G. Curtis, Journal of Physics. D: Applied Physics, 36, R198 (2003).

55. A. Curtis, Euro physics News, 34, 6 (2003).

56. M. Chastellain, A. Petri, M. Hofmann and H. Hofmann, European Cells and Materials, 3, 11 (2002).

57. D. K. Kim W. Voit, W. Zapka, B. Bjelke, M. Muhammed, and K. V. Rao, Material Research Society Symp. Proc., 676 (2001).

58. L. Fu, V.P. Dravid, K. Klug, X. Liu and C.A. Mirkin, “Synthesis and patterning of magnetic nanostructures”, European Cell and Materials, 3, 156 (2002).

59. R. B. Goldfarb and F. R., U. S. Department of Commerce, National Bureau of Standards, Boulder, NBS Special Publication 696, U.S. Government Printing Office (1985).

60. C.A. Ross, Annual Review of Material Research, 31, 203 (2001).

61. S. Okamoto, O. Kitkami, N. Kickuchi, T. Miyazaki, and Y. Shimada, Physical Review B, 67, 094422 (2003).

62. D. Weller and M. F. Doerner, Annual review of materials science, 30, 611 (2000).

63. Y. Shi, J. Ding and H. Yin, Journal of Alloys and Compounds, 303, 290 (2002).

64. Y. Kim, D. Kim and C. S. Lee, Physica B, 337, 42 (2003).

65. C.N. Chinnasamy, M. Senoue, B. Jeyadevan, O. Perales-Perez, K. Shinoda, and K. Tohji, Journal of colloid and interface science, 263, 80 (2003).

66. Q. A. Pankhurst, J. Connolly, S. K. Jones and J. Dobson, Journal of Physics D: Applied Physics, 36, R167 (2003).

67. S. Sun, Eric E. Fullerton, D. Weller and C. B. Murray, IEEE Transactions on magnetics, 37, 1239 (2001).

68. http://www.carolina.com/physics/aboutferro.asp.

69. http://www.zarm.uni-bremen.de/2forschung/ferro/basic_info/applic/index.htm.

70. R. V. Chepulskii and W. H. Butler, Physical Review Letters B, 72, 134205 (2005).

71. S. Sun, Adv. Mater., 18, 393 (2006).

72. O. Gutfleisch, J. Lyubina, K. H. Muller and L. Schultz, Adv. Eng. Mater., 7, 208 (2005).

73. T. Burkert, O. Eriksson, S. I. Simak, A. V. Ruban, B. Sanyal, L. Nordstorm and J. M. Wills, Phys. Rev. B: Condens. Matter Mater. Phys., 71, 134411 (2005).

74. G. Brown, B. Kraczek, A. Janotti, T. C. Schulthess, G. M. Stocks and D. D. Johnson, Phys. Rev. B: Condens. Matter Mater. Phys., 68, 052405 (2003).

75. O. Kitakami, S. Okamoto, N. Kikuchi and Y. Shimada, Jpn. J. Appl. Phys., 42, L455 (2003).

76. J. B. Staunton, S. Ostanin, S. S. A. Razee, B. L. Gyorffy, L. Szunyogh, B. Ginatempo and E. Bruno, Phys. Rev. Lett. 2004, 93, 257204.

77. Y. Zhang, J. Wan, V. Skumryev, S. Stoyanov, Y. Huang, G. C. Hadjipanayis and D. Weller, Applied Physics Letters, 85, 5343 (2004).

78. J. Lyubina, O. Gutfleisch, R. Skomski, K.-H. Muller and L. Schultz, Scripta Materialia, 53, 469 (2005).

79. S. Sun, C. B. Murray, D. Weller, L. Folks and A. Moser, Science 287, 1989 (2000).

80. S. Stappert, B. Rellinghaus, M. Acet and E. F. Wassermann, J. Cryst. Growth, 252, 440 (2003).

81. M. Green, Chem. Commun. 3002 (2005).

82. B. L. Cushing, V. L. Kolesnichenko and C. J. O'Connor, Chem. Rev., 104, 3893 (2004).

83. J. Park, E. Lee, N.-M. Hwang, M. Kang, S. C. Kim, Y. Hwang, J.-G. Park, H.-J. Noh, J.-Y. Kim, J.-H. Park and T. Hyeon, Angew. Chem. Int. Ed., 44, 2872 (2005).

84. D. L. Huber, Small, 1, 482 (2005).

85. H. Kim, M. Achermann, L. P. Balet, J. A. Hollingsworth and V. I. Klimov, J. Am. Chem. Soc., 127, 544 (2005).

86. B. T. Jonker, Y. D. Park, B. R. Bennett, H. D. Cheong, G. Kioseoglou and A. Petrou, Phys. Rev. B, 62, 8180 (2000).

87. Y. Q. Li, G. Zhang, A. V. Nurmikko and S. H. Sun, Nano Lett., 5, 1689 (2005).

88. H. Zeng, J. Li, Z. L. Wang, J. P. Liu and S. H. Sun, Nano Lett., 4, 187 (2004).

89. S. J. Oldenburg, R. D. Averitt, S. L. Westcott and N. J. Halas, Chem. Phys. Lett., 288, 243 (1998).

90. W. L. Shi, Y. Sahoo, M. T. Swihart and P. N. Prasad, Langmuir, 21, 1610 (2005).

91. A. R. Kortan, R. Hull, R. L. Opila, M. G. Bawendi, M. L. Steigerwald, P. J. Carroll and L. E. Brus, J. Am. Chem. Soc., 112, 1327 (1990).

92. H. Yu, M. Chen, P. M. Rice, S. X. Wang, R. L. White and S. H. Sun, Nano Lett., 5, 379 (2005).

93. H. W. Gu, R. K. Zheng, X. X. Zhang and B. Xu, J. Am. Chem. Soc., 126, 5664 (2004).

94. H. W. Gu, Z. M. Yang, J. H. Gao, C. K. Chang and B. Xu, J. Am. Chem. Soc., 127, 34. (2005).

95. K. W. Kwon and M. Shim, J. Am. Chem. Soc., 127, 10269 (2005).

96. S. Kudera, L. Carbone, M. F. Casula, R. Cingolani, A. Falqui, E. Snoeck, W. J. Parak and L. Manna, Nano Lett., 5, 445 (2005).

97. T. Mokari, E. Rothenberg, I. Popov, R. Costi and U. Banin, Science, 304, 1787 (2004).

98. T. Mokari, C. G. Sztrum, A. Salant, E. Rabani and U. Banin, Nat. Mater., 4, 855 (2005).

99. Y. Hou, S. Sun, C. Rong, and J. P. Liu, Appl. Phys. Lett., 91, 153117 (2007).

100. C. B. Rong, V. Nandwana, N. Poudyal, J. P. Liu, M. E. Kozlov, R. H. Baughman, Y. Ding, and Z. L. Wang, J. Appl. Phys., 102, 023908 (2007).
101. H. Zeng, S. Sun, J. Li, Z. L. Wang, and J. P. Liu, Appl. Phys. Lett., 85, 792 (2004).
102. G. S. Chaubey, V. Nandwana, N. Poudyal, C. Rong, and J. P. Liu, Chem. Mater., 20, 475 (2008).
103. D. Suess, T. Schrefl, S. Fähler, M. Kirschner, G. Hrkac, F. Dorfbauer, and J. Fidler, Appl. Phys. Lett., 87, 012504 (2005).
104. C. B. Rong, V. Nandwana, N. Poudyal, Y. Li, J. P. Liu, Y. Ding, and Z. L. Wang, J. Phys. D, 40, 712 (2007).
105. C. B. Rong, Y. Z. Liu, and J. P. Liu, Appl. Phys. Lett., 93, 042508 (2008).
106. C. B. Rong, H. W. Zhang, X. B. Du, J. Zhang, S. Y. Zhang, and B. G. Shen, J. Appl. Phys., 96, 3921 (2004).
107. C. B. Rong, H. W. Zhang, R. J. Chen, S. L. He, and B. G. Shen, J. Magn. Magn. Mater., 302, 126 (2006).
108. K. O'Grady, M. El-Hilo, and R. W. Chantrell, IEEE Trans. Magn., 29, 2608 (1993).
109. C. B. Rong, H. W. Zhang, B. G. Shen, and J. P. Liu, Appl. Phys. Lett., 88, 042504 (2006).
110. R. Coehoorn, D. B. de Mooij, and C. de Waard, J. Magn. Magn. Mater., 80, 101 (1989).
111. A. Manaf, R. A. Buckley, and H. A. Davies, J. Magn. Magn. Mater., 128, 302 (1993).
112. G. C. Hadjipanayis, J. Magn. Magn. Mater., 200, 373 (1999).
113. J. Zhang, S. Y. Zhang, H. W. Zhang, and B. G. Shen, J. Appl. Phys., 89, 5601 (2001).
114. J. Guo, J. S. Jiang, J. E. Pearson, S. D. Bader, and J. P. Liu, Appl. Phys. Lett., 81, 2029 (2002).
115. Z. S. Shan, J. P. Liu, M. Vamsi Chakka, H. Zeng, and J. S. Jiang, IEEE Trans. Magn., 38, 2907 (2002).

116. C. B. Rong, H. W. Zhang, X. B. Du, J. Zhang, S. Y. Zhang, and B. G. Shen, J. Appl. Phys., 96, 3921 (2004).
117. R. Skomski, J. Phys.: Condens. Matter, 15, R841 (2003).
118. A. J. Zambano, H. Oguchi, I. Takeuchi, Y. Choi, J. S. Jiang, J. P. Liu, S. E. Lofland, D. Josell, and L. A. Bendersky, Phys. Rev. B, 75, 144429 (2007).
119. M. Chen, J. P. Liu, and S. H. Sun, J. Am. Chem. Soc., 126, 8394 (2004).
120. C. B. Rong, D. Li, V. Nandwana, N. Poudyal, Y. Ding, Z. L. Wang, H. Zeng, and J. P. Liu, Adv. Mater., 18, 2984 (2006).
121. C. B. Rong, V. Nandwana, N. Poudyal, J. P. Liu, T. Saito, Y. Q. Wu and M. J. Kramer, J. Appl. Phys., 101, 09K515 (2007).
122. C. D. Dai, D. Eakins, N. Thadhani, and J. P. Liu, Appl. Phys. Lett., 90, 071911 (2007).
123. C. B. Rong, V. Nandwana, N. Poudyal, Y. Li, J. P. Liu, M. E. Kozlov, R. H. Baughman, Y. Ding and Z. L. Wang, J. App. Phys., 102, 023908 (2007)
124. H. G. Rutz, F. G. Hanejko, and S. H. Luk, Met. Powder Rep., 49, 40 (1994).
125. G. E. Fougere, J. R. Weertman, and R. W. Siegel, Nanostruct. Mater., 5, 127 (1995).
126. G. F. Bocchini, Powder Metall., 42, 171 (1999).
127. K. Kondoh, T. Takikawa, and R. Watanabe, J. Jpn. Soc. Powder Powder Metall., 47, 941 (2000).
128. H. M. Jaeger and S. R. Nagel, Science, 255, 1523 (1992).
129. K. Williamson and W. H. Hall, Acta Metall., 1, 22 (1953).
130. K. O'Grady, M. El-Hilo, and R. W. Chantrell, IEEE Trans. Magn., 29, 2608 (1993).
131. A. Bollero, O. Gutfleisch, K.-H. Muller, L. Schultz, and G. Drazic, J. Appl. Phys., 91, 8159 (2002).
132. C. B. Rong, H. W. Zhang, B. G. Shen, and J. P. Liu, Appl. Phys. Lett., 88, 042504 (2006).
133. P. Gould, Materials today, 36 (2006).

134. P. Sharma, S. Brown, G. Walter, S. Santra and B. Moudgil, Advances in Colloid and Interface Science, 123, 471 (2006).

135. L. Wang, J. Luo, Q. Fan, M. Suzuki, I. S. Suzuki, M. H. Engelhard, Y. Lin, N. Kim, J. Q. Wang, and C. J. Zhong, J. Phys. Chem. B, 109, 21593 (2005).

136. J. L. Lyon, D. A. Fleming, M. B. Stone, P. Schiffer and M. E. Williams, Nano Lett., 4, 719 (2004).

137. H. Yu, M. Chen, P. M. Rice, S. X. Wang, R. L. White, and S. Sun, Nano Lett., 5, 379 (2005).

138. Y. Li, Q. Zhang, A. V. Nurmikko and S. Sun, Nano Lett., 5, 1689 (2005).

139. C. Rong, N. Poudyal, G. S. Chaubey, V. Nandwana, R. Skomski, Y. Q. Wu, M. J. Kramer, and J. Ping Liu, J. Appl. Phys., 102, 043913 (2007).

140. J. Choi, Y. Jun, S. Yeon, H. Chan Kim, J. Shin, and J. Cheon, J. Am. Chem. Soc., 128, 15982 (2006).

141. T. Pellegrino, J. Am. Chem. Soc., 128, 6690 (2006).

142. A. Cebollada, D. Weller, J. Sticht, G. R. Harp, R. F. C. Farrow, R. F. Marks, R. Savoy, and J. C. Scott, Phys. Rev. B.; Condens. Matter, 50, 3419 (1994).

143. R. F. C. Farrow, D. Weller, R. F. Marks, M. F. Toney, A. Cebollada, and G. R. Harp, J. Appl. Phys., 79, 5967 (1996).

144. D. Weller, A. Moser, L. Folks, M. E. Best, W. Lee, M. F. Toney, M. Schwichert, J. Thiele, and M. F. Doerner, IEEE Trans. Magn., 36, 10 (2000).

145. D. Weller and A. Moser, IEEE Trans. Magn., 35, 4423 (1999).

146. Z. R. Dai, S. Sun, and Z. L. Wang, Nano Lett., 1, 443 (2001).

147. S. Sun, S. Anders, H. F. Hamann, J. Thiele, J. E. E. Baglin, and T. Thomson, J. Am. Chem. Soc., 124, 2884 (2002).

148. S. Anders, M. F. Toney, T. Thomson, R. F. C. Farrow, J. Thiele, and B. D. Terris, J. Appl. Phys., 93, 6299 (2003).

149. S. Momose, H. Kodama, T. Uzumaki, and A. Tanaka, Appl. Phys. Lett., 85, 1748 (2004).

150. A. C. C. Yu, M. Mizuno, Y. Sasaki, M. Inoue, H. Kondo, and I. Ohta, Appl. Phys. Lett., 82, 4352 (2003).

151. S. Kang, D. E. Nikles, and J. W. Harrell. Nano Letters, 2, 1033 (2002).

152. X. Sun, S. Kang, J. W. Harrell, and D. E. Nikles, J. Appl. Phys., 93, 7337 (2003).

153. S. Kang, D. E. Nikles, and J. W. Harrell. J. Appl. Phys., 93, 7178 (2003).

154. S. Wang, S. Kang, D. E. Nikles, J. W. Harrell, and W. X. Wu, J Magn. Magn. Mater., 266, 49 (2003).

155. S. Kang, Z. Jia, D. E. Nikles, and J. W. Harrell, IEEE Trans. Magn., 39, 2753 (2003).

156. S. Kang, Z. Jia, D. E. Nikles, and J. W. Harrell. J. Appl. Phys., 95, 6744 (2004).

157. J. W. Harrell, D. E. Nikles, S. Kang, X. Sun, and Z. Jia, J. Magn. Soc. Japan, 28, 847 (2004).

158. T. Maeda, T. Kai, A. Kikitsu, T. Nagase, and J. Akiyama, Appl. Phys. Lett., 80, 2147, (2002).

159. C. Chen, O. Kitakami, S. Okamoto, and Y. Shimada, Appl. Phys. Lett., 76, 3218 (2000).

160. O. Kitakami, Y. Shimada, K. Oikawa, H. Daimon, and K. Fukamichi, Appl. Phys. Lett., 78, 1104 (2001).

161. J. M. Hove, Interfaces in Materials, Wiley-Interscience (1997).

162. C. L. Platt, K. W. Wierman, E. B. Svedberg, R. Veerdonk, J. K. Howard, and A. G. Roy, J. Appl. Phys., 92, 6104 (2002).

163. V. Nandwana, K. E. Elkins, and J. P. Liu, Nanotechnology, 16, 2823 (2005).

164. S. Pyrpassopoulos, D. Niarchos, G. Nounesis, N. Boukos, I. Zafiropoulou and V. Tzitzios, Nanotechnology, 18, 485604 (2007).

165. Z. Xu, Y Hou and S. Sun, J. Am. Chem. Soc., 129, 8698 (2007).

166. S. Link and M. A. El-Sayed, J. Phys. Chem. B, 103, 8410 (1999).

167. http://web.mit.edu/course/3/3.091/www3/pt/pert2.html.

168. Z. Jia, S. Kang, S. Shi, D. E. Nikles, and J. W. Harrell, J Appl. Phys., 97, 10J310 (2005).

169. D. J. Sellmeyer; R. Skomski, *Advanced Magnetic Materials*; Springer (2006).

170. P. Gaunt, Philos. Mag. 34, 775 (1976).

171. T. B. Massalski, J. L. Murray, L. H. Bernet and H. Baker, Binary Phase Diagrams, ASM International (1986).

BIOGRAPHICAL INFORMATION

Vikas Nandwana was born in Udaipur, India. After completing high school in his hometown, he appeared in the highly competitive engineering examination of India (Joint Entrance Examination) and was ranked 1542 out of 150,000 candidates which placed him one of the most prestigious engineering colleges in India IIT (Indian Institute of Technology) Bombay, where he finished his Bachelors and Masters of Technology degrees in Metallurgical Engineering and Materials science. After the graduation from college, the author felt the need of a better understating and broader knowledge of Materials Science, which motivated him to continue graduate education in Materials Science. He was admitted into the Department of Materials Science and Engineering at the University of Texas at Arlington (UTA), Texas, USA, in 2003. He started his research under the supervision of Prof. J. Ping Liu and worked on the synthesis and characterization of the magnetic nanoparticles and their use in potential applications. The opportunity to work on the synthesis of magnetic nanoparticles and to study their unique magnetic properties has enriched his knowledge and experience in the area of nano-scale magnetism and nanotechnology, an area that has attracted great attention around the world. His and his group's research dealing with the development of advanced nanomaterials including magnetic nanoparticles and nanocomposites has been reported in the well known research media like *PhysicsWorld* and *NanotecWeb* for the significant contributions to the relevant research fields. He wants to contribute more in this area while pursuing his career in a related field.